3D Volume Reconstruction From 2D Plenoptic Data Using FFT-Based Methods

by

John Paul Anglin

A dissertation submitted to the
Graduate Faculty of Auburn University
in partial fulfillment of the requirements for the
Degree of Doctor of Philosophy

Auburn, Alabama
August 1, 2015

Stanley J. Reeves, Chair, Professor of Electrical and Computer Engineering
Thomas S. Denney, Professor of Electrical and Computer Engineering
Lloyd S. Riggs, Professor of Electrical and Computer Engineering
Brian S. Thurow, Associate Professor of Aerospace Engineering

Abstract

Traditional imaging modalities produce images by capturing a 2D slice of the 4D light field. This is an inherently lossy conversion, as the angular information contained in the light field is ignored. Light-field imaging attempts to capture not only the spatial information but also the angular information by sampling the light field from multiple perspectives. By recording both the spatial and angular information contained in the light field, the path each ray travels to the sensor can be reconstructed. By retracing these paths, the image can be refocused to any arbitrary focal plane after acquisition. The resulting images are no longer limited to a 2D space but can now describe the entire 3D imaged volume.

Plenoptic imaging systems are commonly used to generate 2D images at varying focal depths from a single acquired image. This technique can also be extended to create estimates of the 3D imaged volume by creating a stack of these 2D refocused images. However, each 2D refocused image will contain energy from out-of-plane objects, which is commonly recognized as image blur. This image blur is undesirable in many applications utilizing volume reconstructions, and an efficient means of removing this out-of-plane energy is desired. Existing state-of-the-art techniques for producing blur-free reconstructions such as the multiplicative algebraic reconstruction technique (MART) are tomographic approaches. While such techniques can produce exceedingly accurate estimates of the volume, the computational burden is also extremely high. This research describes alternate methods of reconstructing the volume via frequency-domain algorithms.

The focal stack generated by digitally refocusing the acquired data can be modeled as a linear process whereby the system point spread function (PSF) is convolved with the imaged volume. Deconvolution is based on recognizing that convolution is equivalent to point-by-point multiplication in the frequency domain. It follows that the imaged volume

can then be estimated by point-by-point division of its spectrum by the spectrum of the PSF. This is beneficial as calculation of a signal spectrum can be done efficiently via the fast Fourier Transform (FFT) . Where volume reconstruction may have taken hours using tomographic methods, solutions utilizing deconvolution can be obtained in minutes or even seconds. To truly understand the impact that such a drastic reduction in processing time can have, one must consider that processes involving dynamic events rely on not just a single reconstructed volume. To fully describe such events, the volume must be imaged and subsequently reconstructed multiple times to analyze the event.

Fourier-based processing techniques have also been shown to offer computationally efficient alternatives to the more intuitive integration-based refocusing algorithms. Existing research has focused on generating 2D images from the 4D plenoptic data set through the use of the projection-slice theorem [1, 2]. However, these results offer a hint at the flexibility of the projection-slice theorem and its application to higher-dimensional spaces. The 2D/4D projection-slice theorem used to compute 2D images is extended to the 3D/4D case in order to directly generate the 3D focal stack from the 4D plenoptic data. This offers the potential for further improvements in PIV processing speed over conventional tomographic methods. Furthermore, it is shown that the 3D object can be estimated directly from the 3D projections contained within the 4D plenoptic data, again through the use of the projection-slice theorem, without deconvolution.

Acknowledgments

I would like to thank my parents for teaching me that the most rewarding journeys are the most difficult, and there is no substitute for hard work, persistence, and plain old stubbornness.

I would like to thank my advisor, Dr. Stanley Reeves, for his guidance. Dr. Reeves has continually led me in the right direction with a gentle nudge at times, a push at others, and pulled me along the path when necessary. I'm grateful that he has freely given of his time, experience, and insight as well as listened to my occasional rant.

Most importantly, I would like to thank my wife, Rian. Without her I would have never reached the end of this journey. She has celebrated my successes along side me, consoled me following my failures, and encouraged me to keep going when I wanted to give up. She has been a perpetual source of inspiration and reminders that "you're almost done," even when it wasn't true but it was what I needed to hear most.

Table of Contents

List of Figures

List of Tables

List of Abbreviations

CCD	Charge-Coupled Device
DOF	Depth Of Field
FFT	Fast Fourier Transform
HPIV	Holographic Particle Image Velocimetry
IFFT	Inverse Fast Fourier Transform
MART	Multiplicative Algebraic Reconstruction Technique
PIV	Particle Image Velocimetry
PSF	Point Spread Function
SAPIV	Synthetic Aperture Particle Image Velocimetry
TPIV	Tomographic Particle Image Velocimetry

Chapter 1

Introduction

Light-field imaging is a concept brought to mainstream attention by the seminal work of Ren Ng [2] and the Lytro camera. This technology promises to resolve an issue that has plagued photographers since the first images were captured on silver-coated copper plates, that is, the problem of accurate focus. Traditional imaging techniques require the focal plane to be established at the time of image acquisition. Most who have used a camera have experienced a situation where the "perfect" picture has been relegated to the recycle bin because the desired subject was not in focus.

Light-field imaging offers the prospect of taking a photo with little regard for the focus of the image. Instead, the information acquired by these cameras allows the image to be refocused digitally, after the image has been acquired. This shifts the burden of focus from the critical moment in time when the image is taken, to the photographer's post-processing workflow. The ability to refocus during post-processing gives the photographer other tools that may not be immediately obvious. For example, a delicate balance between the light gathering ability of the camera set by the aperture, the depth of field (DOF) , and the shutter speed exists. It is often desirable to photograph a subject using the natural ambient light rather than the harsh light of a camera flash. In order to gather more light, the camera aperture must be opened further which forces the shutter speed to be adjusted in order to maintain the proper exposure. To further complicate matters, the size of the aperture is inversely related to the image DOF, and larger apertures produce a narrower DOF. This relationship prevents the would-be clever photographer from increasing the DOF in order to prevent improper focus. As the aperture is increased to compensate for low ambient light, the DOF is decreased, which requires more accurate focus. However, with the ability to

refocus an image in post-processing, now the photographer can use much larger aperture sizes without concern for improperly focused images. Clearly, this has astounding implications for the field of photography and film.

However, traditional photography is only one of many areas that can benefit from light-field imaging. Light-field imaging provides the ability to infer the source location of the recorded light in 3D, which leads to the possibility of 3D imaging. Potential applications of volumetric reconstruction from 2D image data are numerous. Fluid flow analysis is an area where techniques such as particle image velocimetry (PIV) utilize multiple volumetric estimates in order to reconstruct the movement of particles entrained in a fluid [5–18]. Flame structure and combustion event analysis is another area with impacts in industries ranging from power generation utilities to transportation industries [19–30]. Efficiency improvements in these areas can result in reduced fuel consumption and reduced negative environmental impacts.

The growing ubiquity of lasers and digital cameras with high-resolution sensors has allowed significant advancements in the field of 2D PIV. The laser is used to illuminate a flow field or combustion event, and the sensor detects the scattered light from particles. There are obvious limitations to these 2D planar measurements as fluid flows of interest are rarely 2D in nature [31, 32]. The inherent limitations of 2D planar PIV have led to the development of 3D techniques such as holographic PIV (HPIV) , synthetic aperture PIV (SAPIV) , and tomographic PIV (TPIV) . Of these, SAPIV and TPIV are techniques implicitly based on light field imaging.

Synthetic aperture PIV utilizes an array of five or more cameras to capture a view of the flow and/or combustion event from multiple perspectives. These images are then used to digitally focus on selected focal planes within the measurement volume. Volumetric cross-correlation can then be used to analyze the event [33]. This is a relatively new technology, and currently has some notable limitations. First, multiple cameras are required—on the order of 10-15—to achieve desirable results, and each camera must be triggered simultaneously

when imaging the volume. Further, each camera must be positioned and adjusted such that the entire imaging volume is within the DOF. As alluded to earlier, this places practical limits on the amount of light each camera can acquire for a given aperture as well as the flow velocity due to the corresponding changes in shutter speed.

Finally, tomographic PIV is another method of fluid flow measurement that uses multiple cameras to image the volume from different perspectives. The difference between TPIV and SAPIV lies in the reconstruction algorithm. While SAPIV uses a *map-shift-average algorithm* [33], TPIV typically relies on algebraic methods such as multiplicative algebraic reconstruction technique (MART) to estimate the 3D volume that *explains* the multiple processed views acquired by the camera array. While artifacts such as "ghosting" are possible, this process can produce extremely accurate results, and can operate on the greatest particle field densities of any of the 3D techniques. Unfortunately, traditional multi-camera TPIV has several limitations. Traditional TPIV requires multiple cameras that must be located precisely, and the reconstruction is highly sensitive to errors in camera placement. However, recent publications have proposed the use of light-field cameras, or plenoptic cameras, to replace the camera arrays previously necessary for the technique. This greatly simplifies the process as it eliminates the need for accurate placement of each individual camera and potentially reduces the cost of the system. Furthermore, and most importantly for the research performed here, the MART algorithm is computationally intensive and can require several hours to reconstruct even a modest volume.

This research proposes three novel approaches to reconstructing volumes through the use of Fourier-based techniques. The first, deconvolution, is a frequency-domain processing technique that uses knowledge of the system PSF to reconstruct the original volume. The advantage of this technique is the reduced computational burden. Computation of the frequency spectrum of the refocused 3D image and the spectrum of the PSF can be performed efficiently through the use of the fast Fourier transform (FFT), and volume reconstruction

becomes a matter of a point-by-point division of the spectra. Subsequent techniques demonstrate that the projection-slice theorem can be applied to higher-dimensional projections to reconstruct the object field directly or generate the focal stack for use in deconvolution. For each of these frequency-domain approaches, the processing time for volume reconstruction is expected to be reduced from hours to minutes. Furthermore, dynamic event analysis requires multiple reconstructions to track the event as it develops. The reduced computational demand is therefore compounded by the number of image acquisitions.

Figure 1.1 depicts the relationship of each of the three approaches to volumetric reconstruction from plenoptic data resulting from this research. Existing research is also indicated to clearly identify the contributions of this work with respect to existing methods.

1.1 The Plenoptic Camera

Traditional imaging modalities are limited to recording intensity values at given spatial coordinates. This is a 2D representation of the 4D light field. Light-field imaging, or plenoptic imaging, captures not only the spatial coordinates, but also the angular information associated with each intensity value. There are many methods of recording this information, but most rely on acquiring the image from slightly different perspectives. The first plenoptic camera was invented by Frederick Ives in 1903 and consisted of nothing more than a series of pinhole cameras placed at the focal plane of a traditional large-format camera [34]. The most intuitive implementation using current technology is simply an array of cameras where each is displaced by some known distance from its neighbor. Wilburn et al. have contributed to this research by developing camera arrays such as those shown in Figure 1.2 for use with synthetic aperture imaging [3] and its extension to light-field imaging by [35]. However, the obvious limitation to such a system is its size and cost. The mobility of such a system is limited and therefore impacts its potential applications. The cost is driven by the cost of the individual cameras and increases or decreases accordingly.

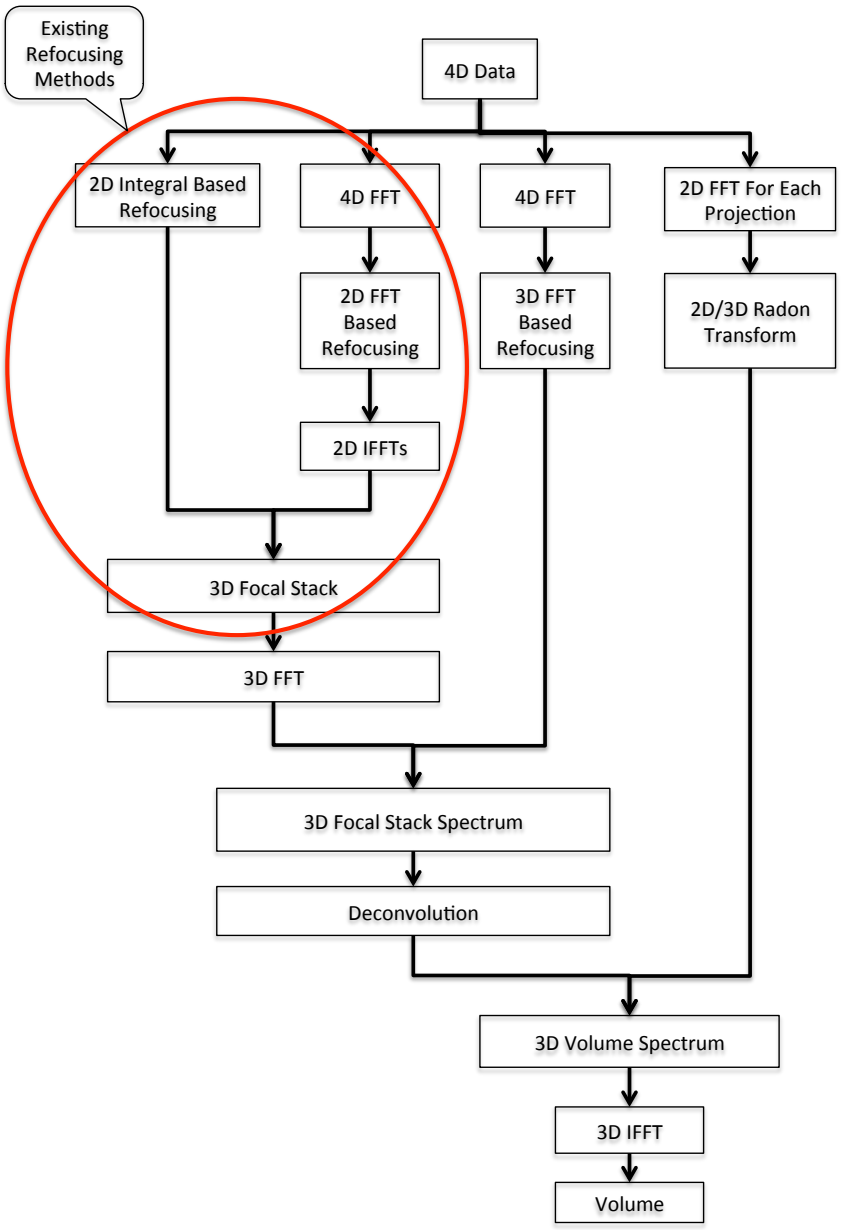

Figure 1.1: Flowchart indicating existing methods in relation to the contributions of this research.

Plenoptic cameras offer another solution to light-field imaging with the advantage of a compact size and potentially reduced cost. In lieu of an a array of cameras, a plenoptic

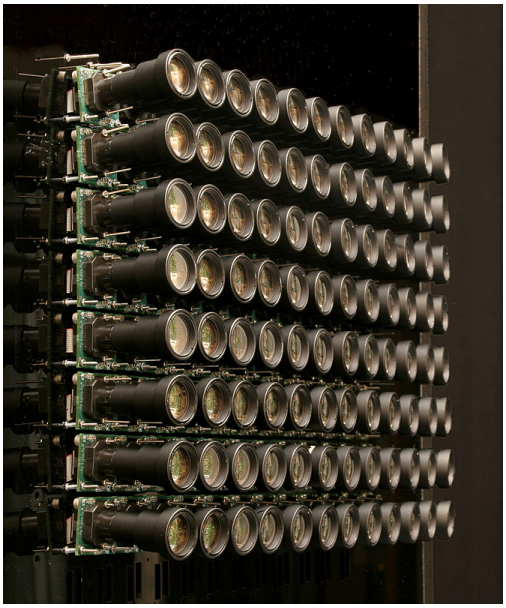

Figure 1.2: Large Camera Array [3]

camera places a microlens array in front of the camera sensor. There are two primary plenoptic camera architectures in current literature, plenoptic 1.0 and plenoptic 2.0 cameras. A plenoptic 1.0 camera places the microlens one focal length f from the sensor plane. In this configuration the microlens array determines the final image resolution where each virtual pixel is the size of a microlens and the sensor pixels correspond to a range of angles in the acquired light field. This represents the fundamental tradeoff in plenoptic imaging where spatial resolution is sacrificed in order to achieve angular resolution. In a plenoptic 2.0 camera, the microlens is placed such that it is focused on the main lens image plane. This has the advantage of improving the spatial resolution of the system but at the cost of a reduction in angular resolution. A comparison of the two architectures is shown in Figure 1.3 [4]. Plenoptic 1.0 will be considered in this document in order to simplify calculations and simulations.

1.2 Computational Image Synthesis

Light-field imaging represents a shift in photography work flow. Previously, photographers were forced to spend a great deal of effort acquiring their desired image. This included

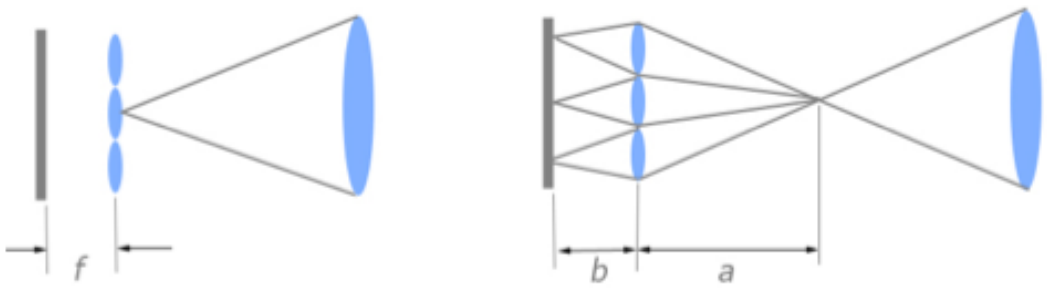

Figure 1.3: Plenoptic 1.0 (left) Plenoptic 2.0 (right) [4]

proper focus, depth of field (DOF), and perspective. A properly acquired image could then be edited to achieve the best possible results. Small corrections in lighting and focus can be achieved by editing the image, but significant changes require manipulation. The distinction is that of utilizing the existing data for the former vs. creating information with the latter. However, light-field imaging offers the photographer much greater flexibility with photo editing by collecting the angular information during photo acquisition. With this information in hand, the photographer is allowed the freedom to refocus the image, change the DOF, or even slightly alter the perspective during post-processing. In this way, photography becomes a process of image synthesis as opposed to image capture. Of particular importance to this research is the ability to synthesize images at any arbitrary focal plane throughout the imaged volume.

The imaging process is commonly described using a two-plane approach where points on the camera aperture are given by (u, v) coordinates and points on the film plane are given by (x, y) coordinates. The irradiance for a given pixel on the camera sensor is then given by

$$E_F(x, y) = \frac{1}{F^2} \iint L_F(x, y, u, v)\, \mathrm{d}u\, \mathrm{d}v, \tag{1.1}$$

where F is the distance between the camera aperture plane and the imaging plane (the film plane in a traditional camera), E_F is the irradiance at (x, y), and L_F is the light field given in terms of the two planes separated by F. Here, terms associated with optical vignetting are

included in L_F, and optical and imaging plane aberrations are ignored. Equation 1.1 states mathematically that a 2D image is obtained by integrating out the angular information from the 4D light field.

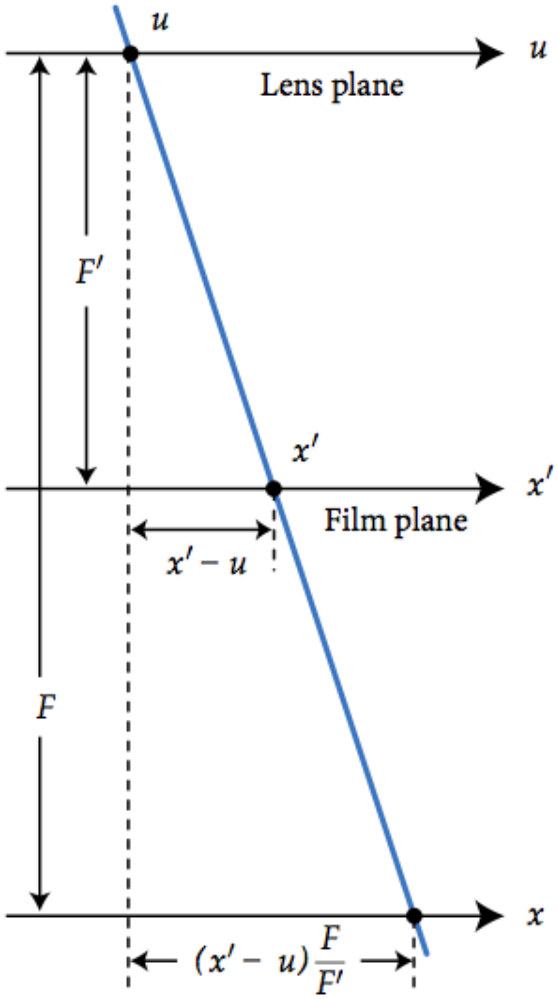

Figure 1.4: Two-plane imaging reparameterization [2]

Figure 1.4 shows that refocusing an image becomes a process of retracing each ray to the point where it intersects the new focal plane F'. This can also be thought of as a shearing of the ray space at the new focal plane. Obtaining an equation for the irradiance at the new focal plane is accomplished by establishing a relationship between L'_F and L_F. Applying properties of similar triangles shows that a ray intersecting the lens plane at u and the film plane at x' also intersects the x plane at $u + (x' - u)\frac{F}{F'}$. This relationship further extends to

the 4D case in a separable fashion. Defining the ratio of the new focal plane to the old as $\alpha = {}^{F'}/_{F}$, the light field at the new focal depth F' is

$$L'_F(x', y', u, v) = L_F\left(u + \frac{x' - u}{\alpha}, v + \frac{y' - v}{\alpha}, u, v\right) \tag{1.2}$$

$$= L_F\left(u\left(1 - \frac{1}{\alpha}\right) + \frac{x'}{\alpha}, v\left(1 - \frac{1}{\alpha}\right) + \frac{y'}{\alpha}, u, v\right). \tag{1.3}$$

Combining this result with (1.1) gives the irradiance at any arbitrary focal plane F':

$$E_{\alpha F}(x', y') = \frac{1}{\alpha^2 F^2} \iint (L_F\left(u\left(1 - \frac{1}{\alpha}\right) + \frac{x'}{\alpha}, v\left(1 - \frac{1}{\alpha}\right) + \frac{y'}{\alpha}, u, v\right) \, \mathrm{d}u \, \mathrm{d}v \tag{1.4}$$

This equation establishes the basis for integration-based refocusing utilizing plenoptic data.

1.3 Ray-space Diagrams, the Radiance Array, and Integral-based Refocusing

The use of a two-plane parameterization also introduces the concept of a Cartesian ray-space diagram and the radiance array. These concepts have proven to be invaluable as a visualization tool in determining the source of spatial variability in the refocusing algorithm. Figure 1.5 shows the relationship between the imaged point and the ray-space diagram in two dimensions. Light rays radiating from a discrete point in space trace a line through the (x, u) plane, where the angle of the line is dependent on the distance of the point from the focal plane. A continuous distribution of light is sampled spatially by the microlens array and angularly by the camera sensor. That is, the pixels underneath each lenslet correspond to angular samples across the camera aperture. Each line in image space corresponds to a single sample of the plenoptic function, which is represented as a point in the ray-space diagram. When digitally refocusing to the plane containing this point, the pixel associated with the point is synthesized by summing the angular samples along this line in the (x, u) plane. Moving the point in the x direction on the current focal plane simply shifts the line

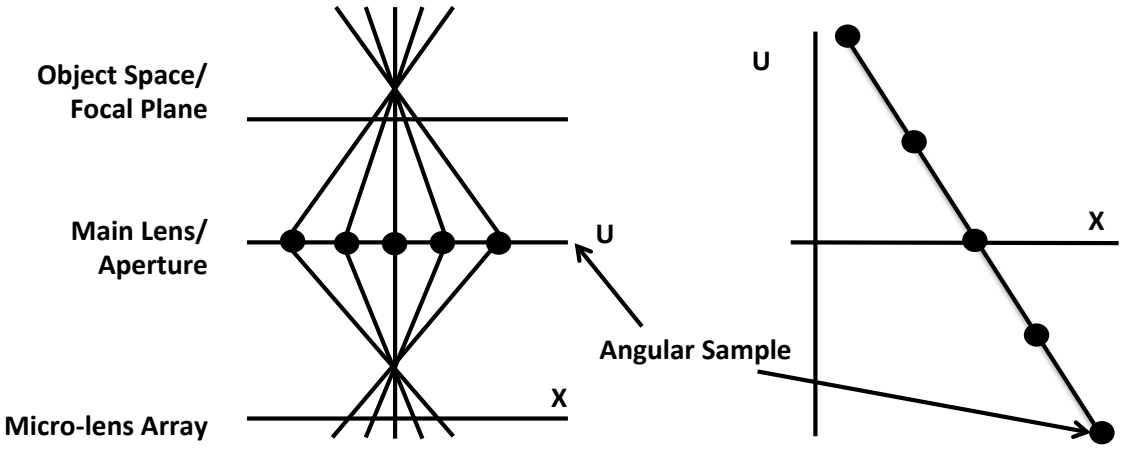

Figure 1.5: Example imaged point (left) and the corresponding ray-space diagram (right). Points along the line in the ray-space diagram are summed to produce a single point in the image.

along the x-axis in the ray-space diagram, while moving off the current focal plane results in a shearing or rotation of the line/samples about the x-axis sample.

The physical application of the ray-space diagram can be seen when considering the sensor data acquired by a plenoptic camera. The camera sensor collects a 2D array of angular samples, but the spatial information is also encoded in the locations of these samples on the sensor. In order to simplify processing, it becomes beneficial to reorder the sensor data into a 4D radiance array that mimics the structure of the ray-space diagram. To clarify and demonstrate concepts, 2D simulated data is presented throughout this work. This data is generated by choosing a point or points in object space and tracing the path of the light rays originating at these points back to the camera lens, to the microlens array, and finally to the sensor. The process is described in greater detail in [31], and the simulation parameters used for the following examples are presented in Table 2.1. Utilizing this process, Fig. 1.6 shows the relationship between the sensor data for a simulated point 9 mm in front of the focal plane and the corresponding radiance array. Note the shearing/rotation of the ray-space samples that occurs for points not on the optical focal plane. With this representation, refocusing to an arbitrary focal plane becomes a matter of choosing the correct angular samples from the radiance array and summing the values. Recognizing that the data acquired for an arbitrary

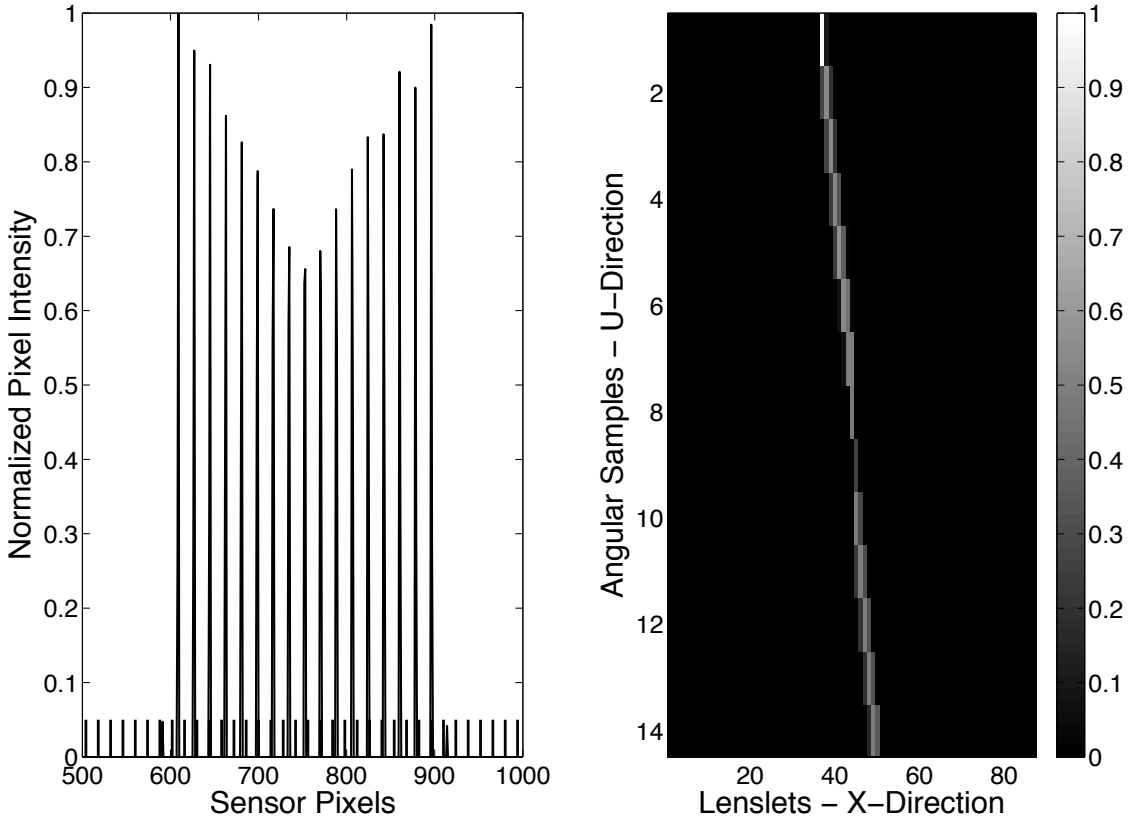

Figure 1.6: Simulated sensor data with micro-lens locations indicated across the bottom (left) and the corresponding radiance array (right) for a point 9 mm in front of the optical focal plane.

point in space is a combination of a shifting and shearing within the radiance array, the samples for that location can be similarly chosen.

Combining these concepts, the integral-based refocusing algorithm can be implemented as follows:

1. Collect the plenoptic data into a radiance array. This should include the calibration/registration process necessary to align the microlens array and image sensor. The plenoptic data should be interpolated onto a plaid grid to simplify processing.
2. Using (1.2), calculate the rays intersecting each point (x', y') in the refocused image. This is equivalent to selecting the appropriate samples from the radiance array. Interpolation is necessary when the calculated sample locations fall between samples in the radiance array.

3. Integrate/sum each of the rays at each point (x', y') to produce the refocused image.
4. Repeat Steps 2 and 3 for each desired focal plane.

Chapter 2

Characterization of Plenoptic Imaging Systems and Efficient Volumetric Estimation from Plenoptic Data

When imaged by a plenoptic camera, an estimate of the imaged volume can be created by generating a focal stack utilizing computational refocusing. When objects are present within the volume, each focal plane within the stack will contain energy from out-of-plane features. FFT-based deconvolution offers a fast and efficient means of removing this volumetric blur, thereby improving the estimate of the volume. While volumetric deconvolution of light-field data has been applied to microscopy [36], the characteristics of these systems are governed by the wave nature of light where each point emits a spherical wave of light. At the macro level, the system is modeled based on ray approximations to light propagation, which yields unique characteristics. Furthermore, microscopes are shift-invariant in the x and y directions [36], which is a significant advantage when applying 3D deconvolution. In contrast, existing refocusing algorithms for light-field cameras are inherently shift-variant, which must be considered when applying 3D deconvolution.

Figure 2.1 indicates how this research utilizes existing integral-based refocusing techniques in conjunction with deconvolution to reconstruct an estimate of a volume. Furthermore, previous research has not adequately characterized and/or identified artifacts resulting from image synthesis from plenoptic data such that the focal stacks can be reliably used in deconvolution.

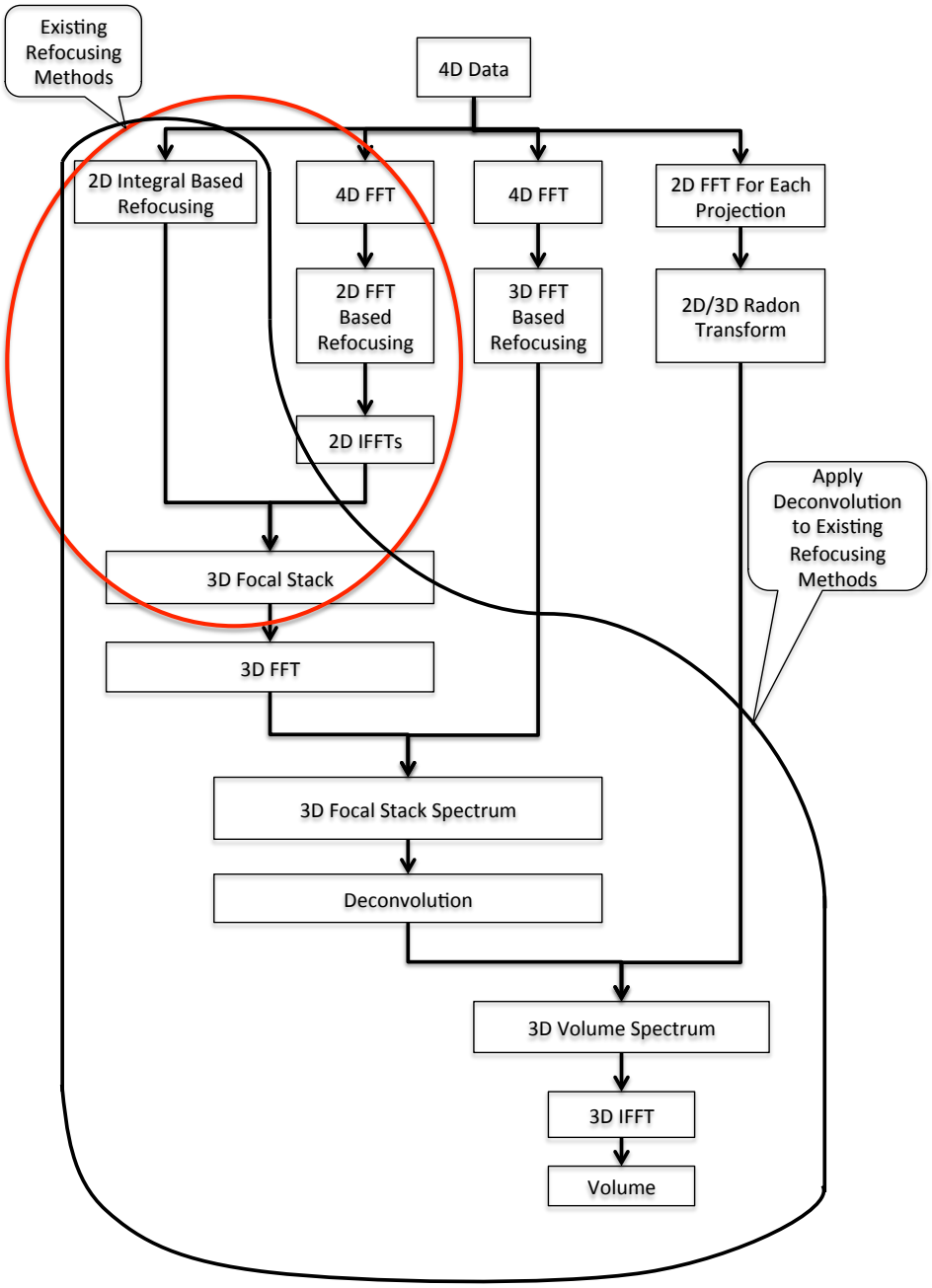

Figure 2.1: Flow chart indicating the application of deconvolution to existing integral-based refocusing techniques.

2.1 Imaging Model

In order to apply deconvolution to volumetric reconstruction, it is necessary to model the system as a convolution in the forward direction. Denoting an arbitrary point in three-space as $f(x, y, z)$, approximating the shift-variant point spread function (PSF) as a shift-invariant function $h(x, y, z)$, noise as $\eta(x, y, z)$, and the resulting image as $g(x, y, z)$, the imaging operation can be approximated as

$$\begin{aligned} g(x,y,z) &= \int_{-\infty}^{\infty}\int_{-\infty}^{\infty}\int_{-\infty}^{\infty} f(x',y',z') \\ &\qquad h(x-x',y-y',z-z')\,dx'\,dy'\,dz' + \eta(x,y,z) \\ &= f(x,y,z) * h(x,y,z) + \eta(x,y,z). \end{aligned} \tag{2.1}$$

The second line follows by denoting the convolution operator as $*$. Equation (2.1) describes the relationship between the imaged point and the focal stack generated by refocusing the plenoptic data.

The PSF is simply the system impulse response. The PSF that describes the typical imaging system will resemble a double cone where the apex of each describes the point when the system is optimally focused. An example PSF is given in Figure 2.2, which shows a point in object space (left figure) and two orthogonal slices of the PSF (center and right figures). From Fig. 2.2, it can be seen that as the system is focused in front of or beyond an object the resulting image will become increasingly blurred. Further, when multiple objects are present in the imaged volume the blur resulting from out-of-plane objects will contribute to the in-plane energy as well. This can reduce the resolution of the system and, in extreme cases, completely obscure some objects.

Ideally, the PSF chosen will completely characterize the imaging system. This would include the blurring that occurs as objects are moved further from the focal plane as well as impacts due to optical aberrations or other system anomalies. Unfortunately, neither the

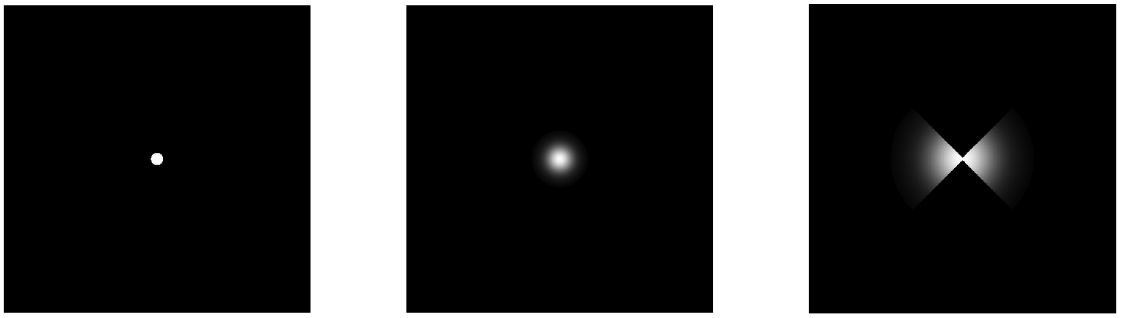

Figure 2.2: Impulse (left) followed by orthogonal cross sections (center and right) of an example 3D impulse response

plenoptic imaging system nor the refocusing algorithm are shift-invariant. However, under certain circumstances and with appropriate strategies, the system can be closely approximated as shift-invariant. Sources of shift-variance must be identified and addressed where possible to provide the best possible agreement between the shift-invariant model and the shift-variant system being analyzed.

Shift-Invariant Image Synthesis

Identifying sources of shift-variance and characterization of the image synthesis process begins with analyzing the refocusing equation

$$E_{\alpha F}(x', y') = \frac{1}{\alpha^2 F^2} \iint L_F \left(u \left(1 - \frac{1}{\alpha} \right) + \frac{x'}{\alpha}, v \left(1 - \frac{1}{\alpha} \right) + \frac{y'}{\alpha}, u, v \right) du dv. \tag{2.2}$$

A compact notation is adopted by letting $\boldsymbol{x} = [x\ y]'$ and $\boldsymbol{u} = [u\ v]'$, which gives

$$E_{\alpha F}(\boldsymbol{x}') = \frac{1}{\alpha^2 F^2} \int L_F \left(\boldsymbol{u} \left(1 - \frac{1}{\alpha} \right) + \frac{\boldsymbol{x}'}{\alpha}, \boldsymbol{u} \right) d\boldsymbol{u}. \tag{2.3}$$

The analysis begins by selecting a point $\boldsymbol{x}'_0$ in image space on some arbitrary focal plane a distance z'_0 from the microlens array. This can be modeled by an impulse $A(z'_0)\delta(\boldsymbol{x}' -$

$\boldsymbol{x}'_0, z' - z'_0)$ with an arbitrary amplitude given by $A(z'_0)$. The object-space impulse is observed through the camera aperture, which limits the range of angular samples and is modeled by applying a windowing function $W(u)$ to the impulse that models the effects of the aperture. The light field for a point source at x'_0 at depth z'_0 from the microlens is defined by:

$$L_{F-z'_0}(\boldsymbol{x}', \boldsymbol{u}) = A(z'_0)\delta(\boldsymbol{x}' - \boldsymbol{x}'_0)W(\boldsymbol{u}) \tag{2.4}$$

The light field L_F at the microlens plane can then be expressed in terms of the light field $L_{F-z'_0}$ at the plane $F - z'_0$ by solving for $\boldsymbol{x}'$ in terms of $\boldsymbol{x}$, where $\alpha = (F - z')/F$:

$$\boldsymbol{x} = \frac{1}{\alpha}[\boldsymbol{u}\,(\alpha - 1) + \boldsymbol{x}'] \tag{2.5}$$

$$\boldsymbol{x}' = \alpha\boldsymbol{x} - \boldsymbol{u}\,(\alpha - 1) \tag{2.6}$$

Let $\alpha_0 = (F - z'_0)/F$. The light field at the microlens array is then

$$L_F\,(\boldsymbol{x}, \boldsymbol{u}) = L_{F-z'_0}\,(\alpha_0\boldsymbol{x} - \boldsymbol{u}\,(\alpha_0 - 1)\,, \boldsymbol{u}) \tag{2.7}$$

$$= A(z'_0)\delta\,(\alpha_0\boldsymbol{x} - \boldsymbol{u}\,(\alpha_0 - 1) - \boldsymbol{x}'_0)\,W(\boldsymbol{u}) \tag{2.8}$$

$$= \frac{A(z'_0)}{\alpha_0^2}\delta\left(\boldsymbol{x} - \boldsymbol{u}\left(1 - \frac{1}{\alpha_0}\right) - \frac{\boldsymbol{x}'_0}{\alpha_0}\right)W(\boldsymbol{u}) \tag{2.9}$$

$$= \delta\left(\boldsymbol{x} - \frac{\boldsymbol{x}'_0}{\alpha_0} - \boldsymbol{u}(1 - \frac{1}{\alpha_0})\right)W(\boldsymbol{u}) \tag{2.10}$$

where the last line is obtained by setting $A(z'_0) = \alpha_0^2$.

Note that the light field at $F - z'_0$ is shifted by $\boldsymbol{x}'_0$, while the light field at the microlens array is shifted by a function dependent upon the location of the impulse along z. Therefore, the imaging equation based on this light field parameterization is shift-variant. However, we propose a new geometric transformation of the image space that makes the transformed system shift-invariant. We accomplish this by scaling the argument when evaluating functions of the light field at the microlens.

Define a mapping from an image space $\boldsymbol{x}''$-plane, where $\boldsymbol{x}''$ is used to denote an $\boldsymbol{x}$ position in the scaled image space, to the light-field plane with the scaling removed ($\hat{\boldsymbol{x}}$):

$$\hat{\boldsymbol{x}} = \boldsymbol{u}\,(\alpha - 1) + \boldsymbol{x}'' \tag{2.11}$$

$$\boldsymbol{x}'' = \hat{\boldsymbol{x}} - \boldsymbol{u}\,(\alpha - 1) \tag{2.12}$$

where $\alpha = (F - z'')/F$. The modified light field $L''_{F-z''}(\boldsymbol{x}'', \boldsymbol{u})$ at an arbitrary focal plane z'' can now be calculated in terms of the light-field pattern created by the impulse:

$$L''_{F-z''}(\boldsymbol{x}'', \boldsymbol{u}) = L_F\left(\hat{\boldsymbol{x}}, \boldsymbol{u}\right)\Big|_{\hat{\boldsymbol{x}}=\boldsymbol{u}(\alpha-1)+\boldsymbol{x}''} \tag{2.13}$$

$$= \delta\left(\boldsymbol{u}\,(\alpha - 1) + \boldsymbol{x}'' - \boldsymbol{u}(1 - \frac{1}{\alpha_0}) - \frac{\boldsymbol{x}'_0}{\alpha_0}\right) W(\boldsymbol{u}) \tag{2.14}$$

$$= \delta\left(\boldsymbol{u}[\alpha - 1 - 1 + \frac{1}{\alpha_0}] + \boldsymbol{x}'' - \frac{\boldsymbol{x}'_0}{\alpha_0}\right) W(\boldsymbol{u}) \tag{2.15}$$

Observe that

$$\alpha - 1 - 1 + \frac{1}{\alpha_0} = \frac{F - z''}{F} - \frac{F}{F} + \frac{z'_0 - F}{F - z'_0} + \frac{F}{F - z'_0} \tag{2.16}$$

$$= -\frac{1}{F}\left(z'' - \frac{F}{F - z'_0} z'_0\right) \tag{2.17}$$

$$= -\frac{1}{F}\left(z'' - \frac{z'_0}{\alpha_0}\right) \tag{2.18}$$

Further defining the following transformed coordinates:

$$\boldsymbol{x}''_0 = \frac{\boldsymbol{x}'_0}{\alpha_0} \tag{2.19}$$

$$z''_0 = \frac{z'_0}{\alpha_0} \tag{2.20}$$

we substitute into the previous expression to obtain

$$L''_{F-z''}(\boldsymbol{x}'', \boldsymbol{u}) = \delta\left(-\boldsymbol{u}\frac{1}{F}(z'' - z''_0) + \boldsymbol{x}'' - \boldsymbol{x}''_0\right) W(\boldsymbol{u}) \tag{2.21}$$

Note that evaluating this modified function at $z'' = z''_0$ yields

$$L''_{F-z''_0}(\boldsymbol{x}'', \boldsymbol{u}) = \delta(\boldsymbol{x}'' - \boldsymbol{x}''_0) W(\boldsymbol{u}) \tag{2.22}$$

which is the light-field function arising from an impulse in scaled image space $\delta(\boldsymbol{x}'' - \boldsymbol{x}''_0, z'' - z''_0)$. The integral over the aperture is then calculated by integrating over $\boldsymbol{u}$ to find modified refocused images at each z''-plane:

$$E''_{F-z''}(\boldsymbol{x}'') = \int L''_{F-z''}(\boldsymbol{x}'', \boldsymbol{u}) d\boldsymbol{u} \tag{2.23}$$

$$= \int \delta\left(-\boldsymbol{u}\frac{1}{F}(z'' - z''_0) + \boldsymbol{x}'' - \boldsymbol{x}''_0\right) W(\boldsymbol{u}) d\boldsymbol{u} \tag{2.24}$$

$$= \frac{F^2}{(z'' - z''_0)^2} W\left((\boldsymbol{x}'' - \boldsymbol{x}''_0)\frac{F}{z'' - z''_0}\right) \tag{2.25}$$

Thus, a shift of the input impulse by $(\boldsymbol{x}''_0, z''_0)$ results in a shift of the refocused image by the same amount, which demonstrates shift-invariance. The resulting algorithm for calculating a shift-invariant focal stack is

$$E_{\alpha F}(x'', y'') = \iint L_F\big(u\,(\alpha - 1) + x'', v\,(\alpha - 1) + y'', u, v\big) du dv. \tag{2.26}$$

Figure 2.3 depicts a single ray in both scaled (solid trace) and unscaled (dashed trace) image space intersecting (x', x'') on the $\alpha = 0.7$ image plane. The rays resulting from a shift of $(x'_0 = x''_0, z'_0 = z''_0)$ are also shown by the upper two traces. The figure shows that in unscaled image space a shift of (x'_0, z'_0) results in a shift of $(\frac{x'_0}{\alpha_0})$ at the microlens plane

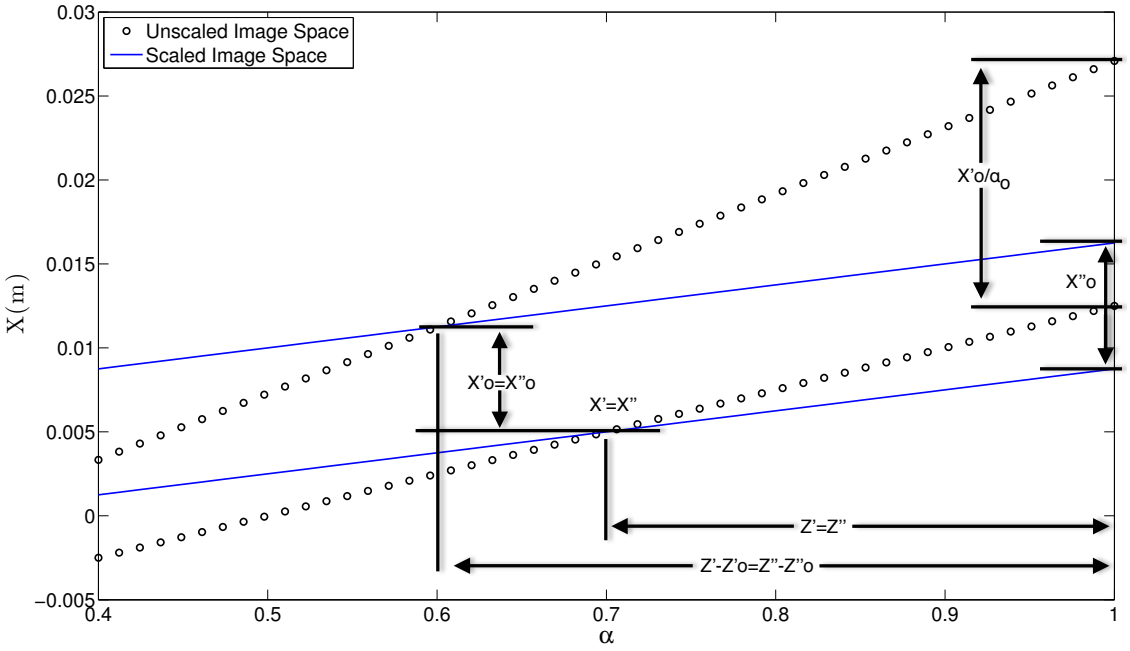

Figure 2.3: Impact of image-space scaling on a point shifted by $(x_0' = x_0'', z_0' = z_0'')$

$(\alpha = 1)$. However, in scaled image space a (x_0'', z_0'') shift yields an equivalent shift at the microlens plane $(\alpha = 1)$, again showing shift-invariance.

The impact of this modification to the algorithm can further be seen by plotting the boundary of the PSF both before and after the scaling is applied. The boundary of the PSF at a given focal plane can be calculated by utilizing (2.6). The PSF can be plotted by setting u to the limits of the camera aperture, selecting two x intercept points at the micro-lens, and plotting x' over a range of α values. The top row of Fig. 2.4 shows example PSFs depicting how the shape of the impulse response will change throughout the image in both x- and z-directions. Equations (2.2) and (2.6) show that the slope of the PSF boundary is set by $(x - u)$ which will vary for every point in the imaged space.

The boundary of the PSF in scaled coordinates is obtained similarly from (2.12). The slope of the PSF boundary in scaled coordinates is now set by u which is constant for every point throughout the volume. This can be seen in the second row of Fig. 2.4 which depicts the PSFs in scaled coordinates.

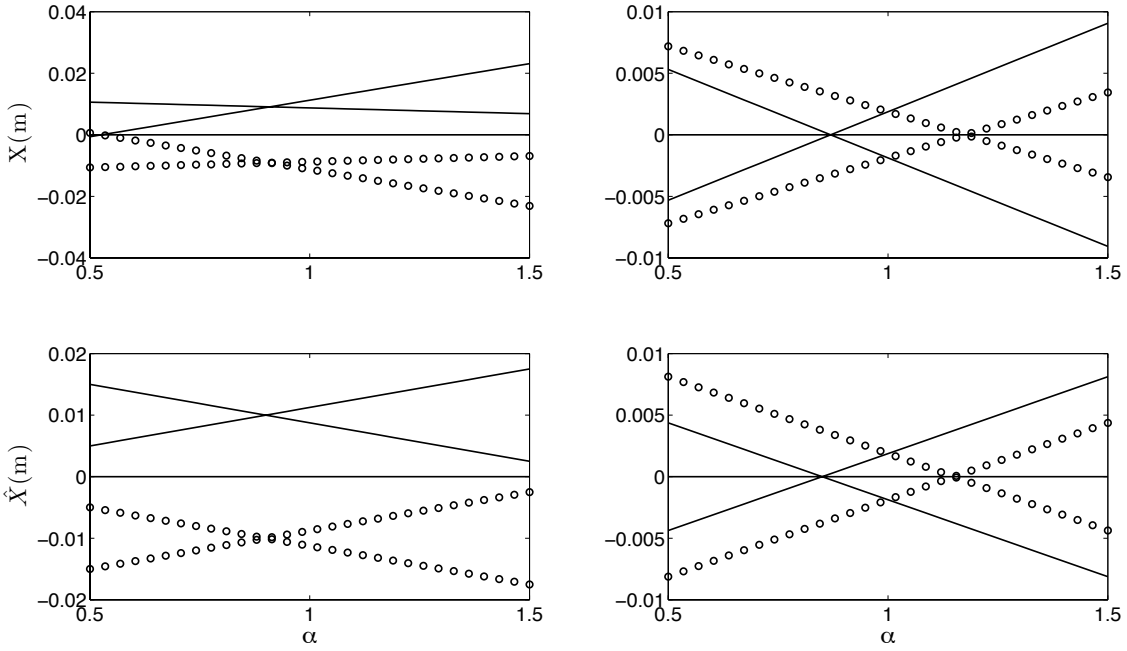

Figure 2.4: Unscaled PSFs (top) showing spatial variability in (x) (left) and in (z) (right) and scaled PSFs (bottom) showing shift-invariance in (x, z).

Additional Sources of Shift Variance

Unfortunately, the sampling and reconstruction process introduces further sources of shift-variance. One source occurs when objects or features are imaged across multiple micro-lenses. This can occur when objects are located at the boundary of multiple micro-lenses or when objects off the focal plane are imaged. Quantization artifacts result in variations in the reconstructed points. Other sources of shift-variance result from the reconstruction algorithm itself and can be seen by inspecting the simulated PSF and its corresponding radiance array shown in Fig. 2.5.

The most prominent feature of the PSF is the alternating light and dark bands that appear as the PSF decays from the optical centerline. The source of these bands becomes apparent when considering the samples of the radiance array responsible for example regions of the PSF. To illustrate, a point along one of the bright regions in the focal stack is denoted by an $*$. The samples integrated to obtain the point, likewise denoted by an $*$, are overlaid on the radiance array. Of note is the single sample that falls within the data (i.e. non-zero

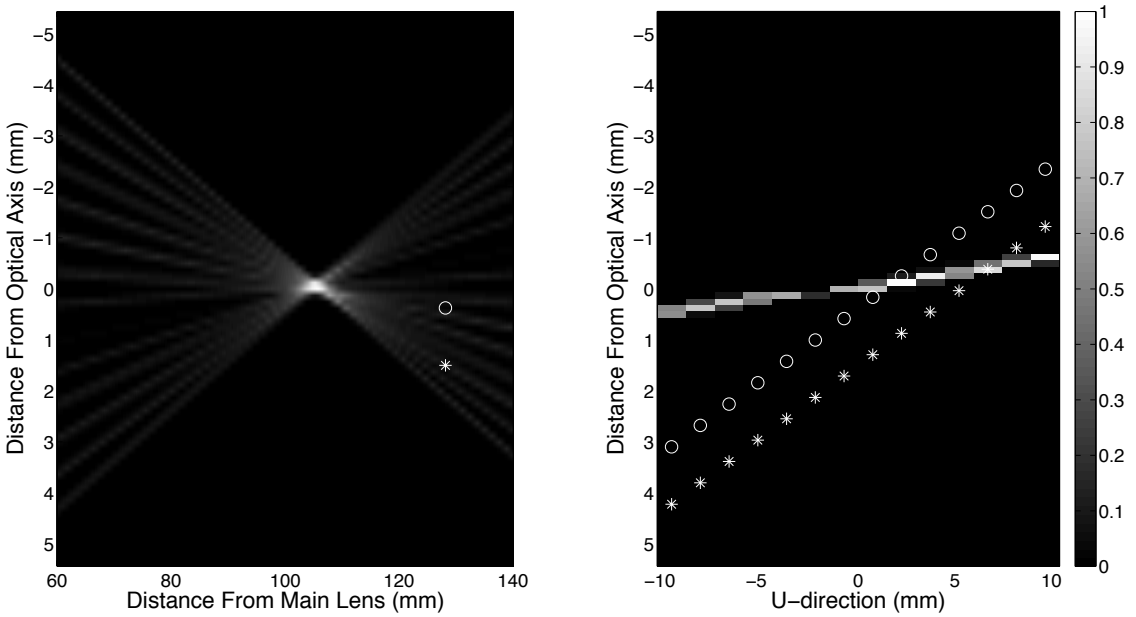

Figure 2.5: PSF (left) showing banding with two sample points denoted by an $*$ and a $\circ$ in the PSF with the associated samples in the radiance array (right).

region) of the radiance array. When the samples from the radiance array are summed to the sample of the PSF, this single sample in the data region of the radiance array is the most significant contributor to the intensity of the point in the PSF. A second point is chosen that falls within one of the dark bands and is denoted by a $\circ$ along with the corresponding samples from the radiance array. The samples from the radiance array that are summed to obtain this point fall on either side of the data in the radiance array. As a result, the sum produces a much lower intensity in the corresponding point in the PSF. The banding pattern varies with the origin of the point source because the shift changes the relative positions of the data band and the sampling locations along the sampling line. Thus, banding produces a shift-variant pattern.

This analysis of banding reveals that this banding is not the result of inadequate data collection, or aliasing, but of inadequately sampling the data that has been recorded. To address the issue, at least in part, simply increasing the number of samples used in the reconstruction can significantly reduce the banding present in the focal stack. Figure 2.6 depicts the case where four times as many data samples are used to reconstruct the PSF

from the same radiance array. Once again the points in the PSF and the corresponding samples in the radiance array are identified.

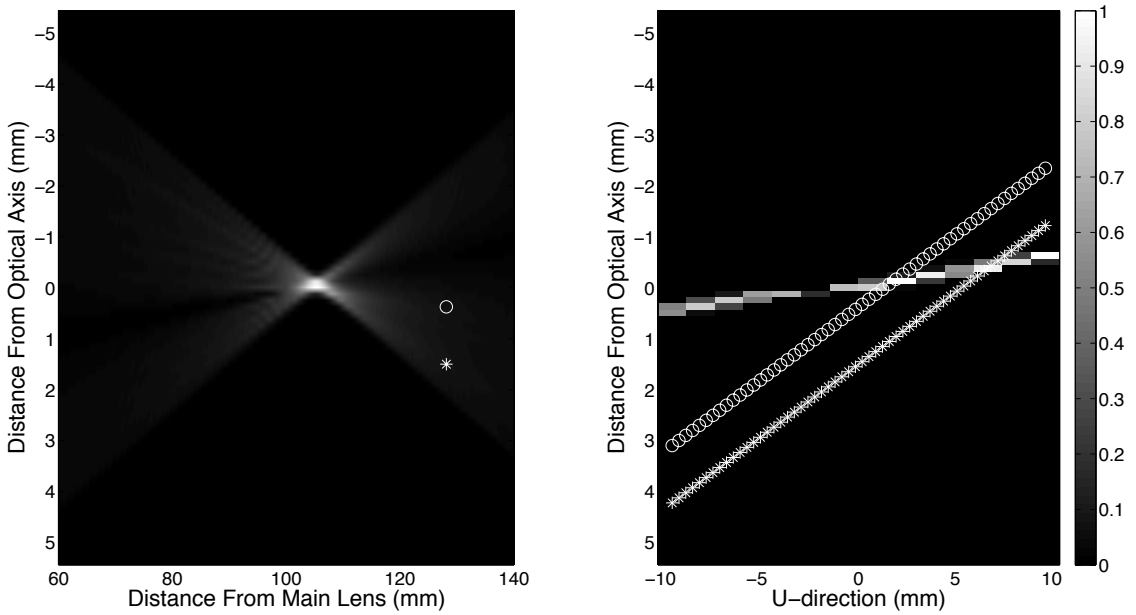

Figure 2.6: PSF (left) obtained by oversampling the radiance array (right). Increasing the samples used in the reconstruction algorithm produces a smoother response.

While oversampling improves the reconstruction significantly, some asymmetric banding and dark regions persist in the PSF. Both artifacts are identified in Fig. 2.7. Again comparing the points in the PSF with the corresponding samples from the radiance array demonstrates the source of these artifacts.

First, the persistent banding is caused when the samples for a point in the PSF have the opposite slope compared to the radiance data. This can be seen when comparing the radiance array samples shown in Fig. 2.6 and Fig. 2.7. In the former, the discontinuities in the data are masked by the overlapping angular information between adjacent micro-lenses. Because the slope of the samples has the same sign, more samples consistently fall on regions containing data, which results in a more uniform intensity. In the latter, because the slope of the samples has the opposite sign as the data and the data has a stair step structure, as the slope changes the number of samples falling on data regions varies more dramatically. This causes the alternating light and dark regions in the refocused image. This also explains why

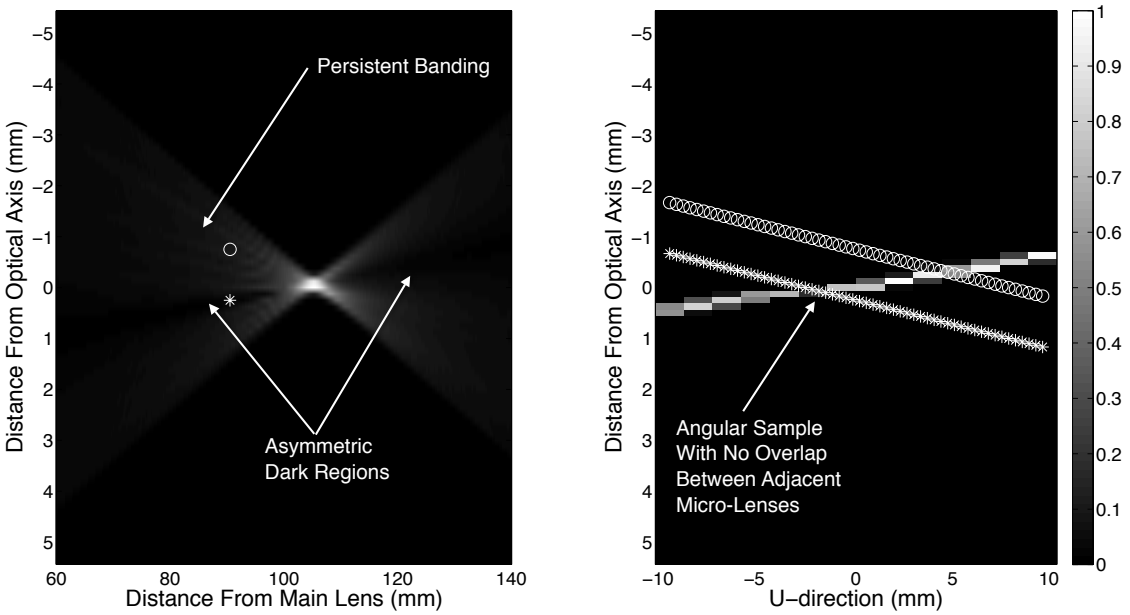

Figure 2.7: Persistent asymmetric banding and dark regions in the PSF (left) with two example points identified and the corresponding samples from the radiance array (right) shown.

this source of banding appears only on one side of the optical focal plane, since sampling with the same *slope* as the data band yields a smoother response.

Second, the dark regions on either side of the focused point are related to the persistent banding described above. The point denoted by an $*$ in Fig. 2.7 falls in one of the dark regions, and its corresponding samples are shown on the radiance array. It can be seen that the samples cross a region in the data where no overlap exists between angular samples. As a result, fewer samples in the reconstruction collect data, which results in a lower intensity.

These banding artifacts are of concern because they are also spatially variant and cannot be eliminated by post-processing techniques. The persistent banding will vary depending on the position of the point and is asymmetric about the point center depending on which side of the optical focal plane the point appears. The dark regions appear when angular data is collected by a single micro-lens, which again is a spatially variant phenomena. Addressing these issues requires direct manipulation of the data or the imaging system and is the subject of future research. For the purposes of this work, these are sources of spatial variability within

the reconstruction. While these sources of variability result in artifacts in the reconstruction, the impact is small and deconvolution still yields significant reductions in overall image blur.

With the imaging system modeled and sources of variability identified and addressed where possible, implementation of a deconvolution algorithm can be pursued.

2.2 Deconvolution

Deconvolution, also known as inverse filtering, is a frequency-domain processing technique that relies on the well-known convolution theorem of the Fourier transform. This states that convolution in the spatial domain is equivalent to point-by-point multiplication in the frequency domain, or

$$f(x,y,z) \star h(x,y,z) \stackrel{\mathfrak{F}}{\rightarrow} F(\omega_x,\omega_y,\omega_z)H(\omega_x,\omega_y,\omega_z)$$

Applying this result to Equation 2.1 gives

$$g(x,y,z) = f(x,y,z) \star h(x,y,z) + \eta \tag{2.27}$$

$$f(x,y,z) \star h(x,y,z) + \eta(x,y,z) = \mathfrak{F}^{-1}\left[F(\omega_x,\omega_y,\omega_z)H(\omega_x,\omega_y,\omega_z) + N(\omega_x,\omega_y,\omega_z)\right] \tag{2.28}$$

In the absence of noise, the imaged space can be estimated as

$$\hat{F}(\omega_x,\omega_y,\omega_z) = \frac{G(\omega_x,\omega_y,\omega_z)}{H(\omega_x,\omega_y,\omega_z)} \tag{2.29}$$

Unfortunately, the system is rarely, if ever, noise free. The general case is then,

$$\hat{F}(\omega_x,\omega_y,\omega_z) = F(\omega_x,\omega_y,\omega_z) + \frac{N(\omega_x,\omega_y,\omega_z)}{H(\omega_x,\omega_y,\omega_z)} \tag{2.30}$$

Equation 2.30 offers some insight into both the advantages and disadvantages of inverse filtering. The primary advantage is speed of computation. Direct convolution requires N^2

operations while convolution via FFT requires $\mathrm{O}(N \log N)$. However, perfect knowledge of the transfer function no longer guarantees a perfect reconstruction of the original volume once noise is introduced. Furthermore, a transfer function containing small values will result in an amplification of the noise term in the estimate of the imaged volume. As these values approach zero, the noise term will dominate the response. This case is common because the system typically represents an infinite bandwidth scene with band limited data. The consequence is a transfer function with zero crossings.

The impacts of this noise amplification and PSF mismatch can be mitigated to some degree with proper filtering. One approach is to minimize the expected value ($E\{\cdot\}$) of the squared error

$$e^2 = E\left\{\left(f - \hat{f}\right)^2\right\}. \tag{2.31}$$

The well known result of this minimization is the Wiener filter given by

$$\hat{F}(\omega_x, \omega_y, \omega_z) = \left[\frac{H^*(\omega_x, \omega_y, \omega_z)}{|H^*(\omega_x, \omega_y, \omega_z)|^2 + \frac{S_\eta(\omega_x, \omega_y, \omega_z)}{S_f(\omega_x, \omega_y, \omega_z)}}\right] G(\omega_x, \omega_y, \omega_z) \tag{2.32}$$

where S_η and S_f are the power spectrum of the noise and the original image volume respectively. When the power spectrums are not known, which is often the case, the ratio of the power spectrums are replaced by a regularization parameter K. Substituting this into Equation 2.32 gives

$$\hat{F}(\omega_x, \omega_y, \omega_z) = \left[\frac{H^*(\omega_x, \omega_y, \omega_z)}{|H(\omega_x, \omega_y, \omega_z)|^2 + K}\right] G(\omega_x, \omega_y, \omega_z) \tag{2.33}$$

For the noise free case with perfect PSF agreement, the regularization factor K can be set to zero, which reduces Equation 2.33 back to Equation 2.29. These relationships can be applied directly to plenoptic data.

2.2.1 Effects of Regularization and Artifact Identification

To demonstrate the efficacy of deconvolution when applied to plenoptic imaging and to identify artifacts in the reconstruction, two example cases are presented. The first is a a simplified 2D case which is used to identify artifacts in the deconvolved reconstruction. The second is a 3D case used to demonstrate results when the algorithm is applied to experimentally acquired volumetric data.

2.2.2 2D Reconstruction

For the 2D example case, the system is modeled with a native focal plane at 100 mm and the remaining system parameters as identified in Table 2.1. The simulations presented here utilize a lenslet pitch that is not an integer multiple of the pixel pitch. As a result, some overlap exists between pixels associated with adjacent micro-lenses. This accurately simulates the physical scenario, and these ambiguous pixels must be discarded before creating the radiance array.

Table 2.1: 2-D Simulation Parameters

Lenslet Focal Length	f_l	0.500 mm
Lenslet Pitch	p_l	0.125 mm
Pixel Pitch	p_p	0.0074 mm
Number of Pixels	n_p	1503
Sensor Size		10.5 mm
Number of Lenslets	n_l	89
Main Lens Focal Length	f_m	50 mm

Another important aspect of generating the radiance array is properly registering the micro-lens array with respect to the sensor. This step accounts for shifts and/or rotations of the micro-lens array relative to the sensor as well as the case where the micro-lens pitch is not an integer multiple of the pixel pitch. While the details of such a process are not considered here, the simulations provided here are calibrated via a calibration image in the same way experimental data would be calibrated. This process identifies the center of each micro-lens with respect to the sensor. The sensor data is then interpolated onto a uniform

grid that simulates the perfectly aligned/integer multiple scenario. This ensures that each row of the radiance array corresponds to the same angle, while each column represents the same spatial location throughout the array. Without this step, each entry within the 2D array (for 2D images) or the 4D array (for 3D volumes) must be uniquely identified within the (x, u) space or the (x, y, u, v) space respectively. Utilizing a plaid—that is, separably sampled—array significantly improves computational efficiency of the refocusing algorithm. This plaid data is then used by the refocusing algorithm to generate the focal stack. Inclusion of these steps is intended to more accurately model the physical system, its parameters, and potential sources of error from the algorithm.

A PSF must be selected in order to apply deconvolution to a simulated point field. The PSF chosen for the first simulation is based on a point located at the optical focal plane along the optical axis. This ensures that the point is imaged by a single micro-lens. This is a unique point in the system in that the banding and dark regions present in PSFs located elsewhere in the imaged space are not present. A particle located at this point will exhibit a smooth decay in all directions. This is due to the structure of the data in the radiance array, which does not exhibit the step-like discontinuities associated with points off the focal plane. These characteristics can be seen in Fig. 2.8. Furthermore, the simulated point is ideal in that each ray used in the simulation originates from an infinitesimally small point. While such a point is not likely to be used for experimental data, it serves to show that the artifacts resulting from the deconvolution are inherent in the system and not specifically the result of the artifacts in the PSF.

With a PSF chosen, the simulation proceeds with a test case where three points are placed within the simulated imaging volume at $(1.3\text{mm}, 91.2\text{mm})$, $(1.9\text{mm}, 97.5\text{mm})$, and $(-2.5\text{mm}, 112.5\text{mm})$, where the second point is again located on the optical focal plane along the optical axis. The second point is included in order to provide a reference as it should perfectly match the test PSF. As with the PSF, each point is simulated using 5000

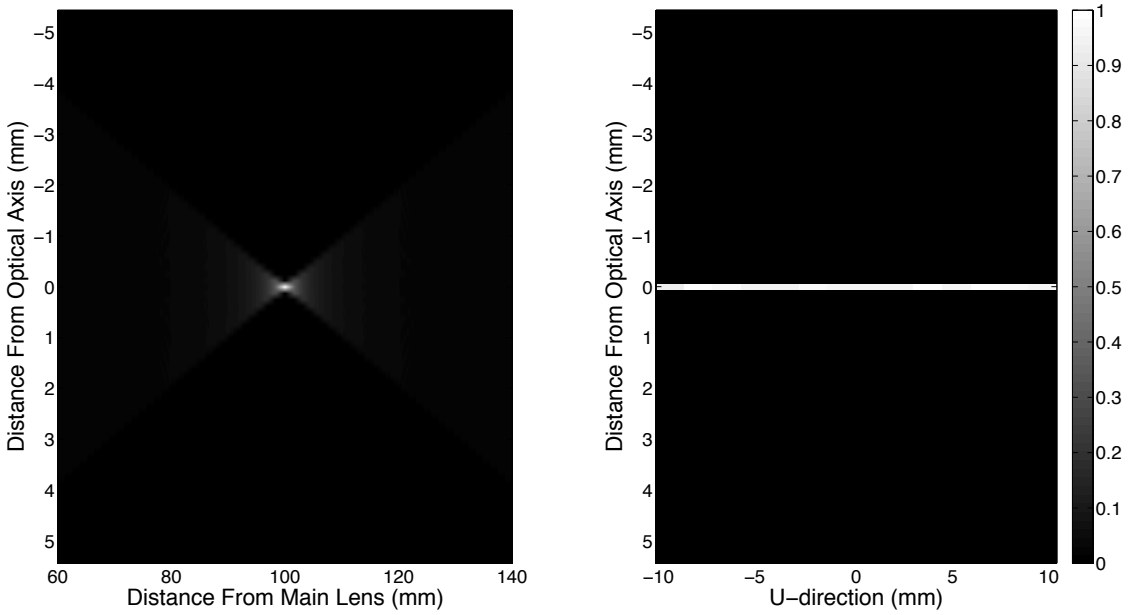

Figure 2.8: Simulated 2-D PSF (left) and the associated radiance array (right).

rays originating from an infinitesimally small point. Figure 2.9 shows the resulting focal stack for this case where the figures are normalized to the peak value to aid in clarity.

There are two aspects of Figure 2.9 that are immediately apparent and ultimately related. Specifically, the three points have significantly different intensities and varying sizes. This is of note because each point is simulated using the same number of rays, and therefore has the same energy, as well as being simulated as an infinitely small point. This would seem to indicate that each point should have the same, or similar intensity and size at its optimal focal plane. This would be true if the plenoptic camera were able to focus equally well at all possible focal planes. However, the resolution of the plenoptic camera at synthesized focal planes is limited by the bandwidth of the camera. For the purposes of this research, this is a contributor to the spatially variant nature of the PSF.

Applying deconvolution per Equation 2.33 with minimal regularization ($K = 1 \times 10^{-8}$) gives the results shown in Figure 2.10. This appears to have little in common with the original image shown in Figure 2.9, but this is to be expected. Closer inspection shows that the point at the origin is present in the deconvolved image. Again, the central point was

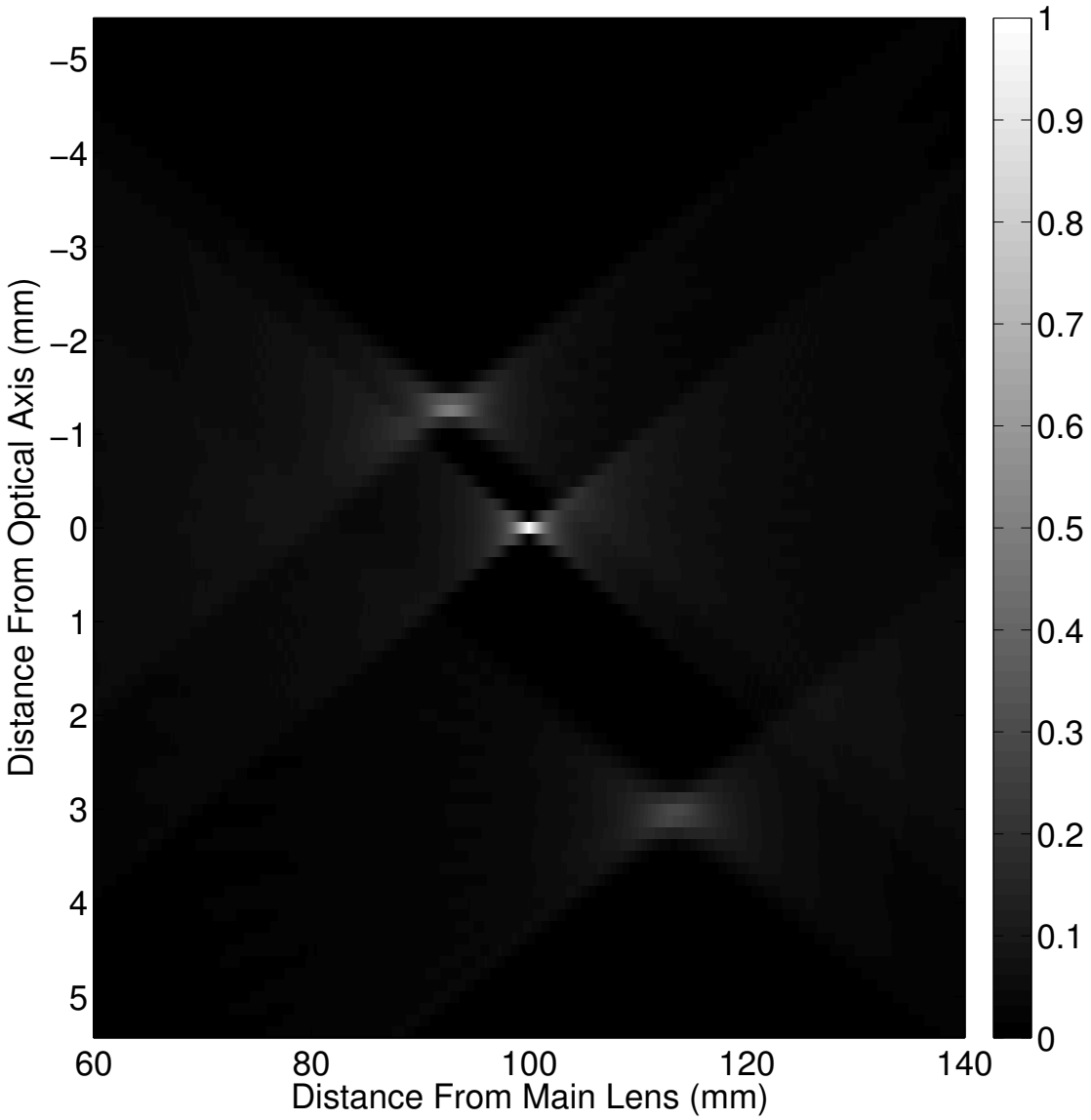

Figure 2.9: Focal stack for three simulated points.

chosen as it perfectly matches the test PSF. Because little regularization is applied, only the point with near perfect agreement with the PSF is recovered in the reconstruction.

Applying regularization to the deconvolution algorithm produces more desirable results. Figure 2.11 shows the results when $K = 1 \times 10^{-4}$ regularization is applied. This is a small amount of regularization, but the impact is significant. The three points are clearly present in the reconstruction. Further increasing the regularization to $K = 0.1$ yields the response shown in Figure 2.12. This is an increase of three orders of magnitude in the regularization,

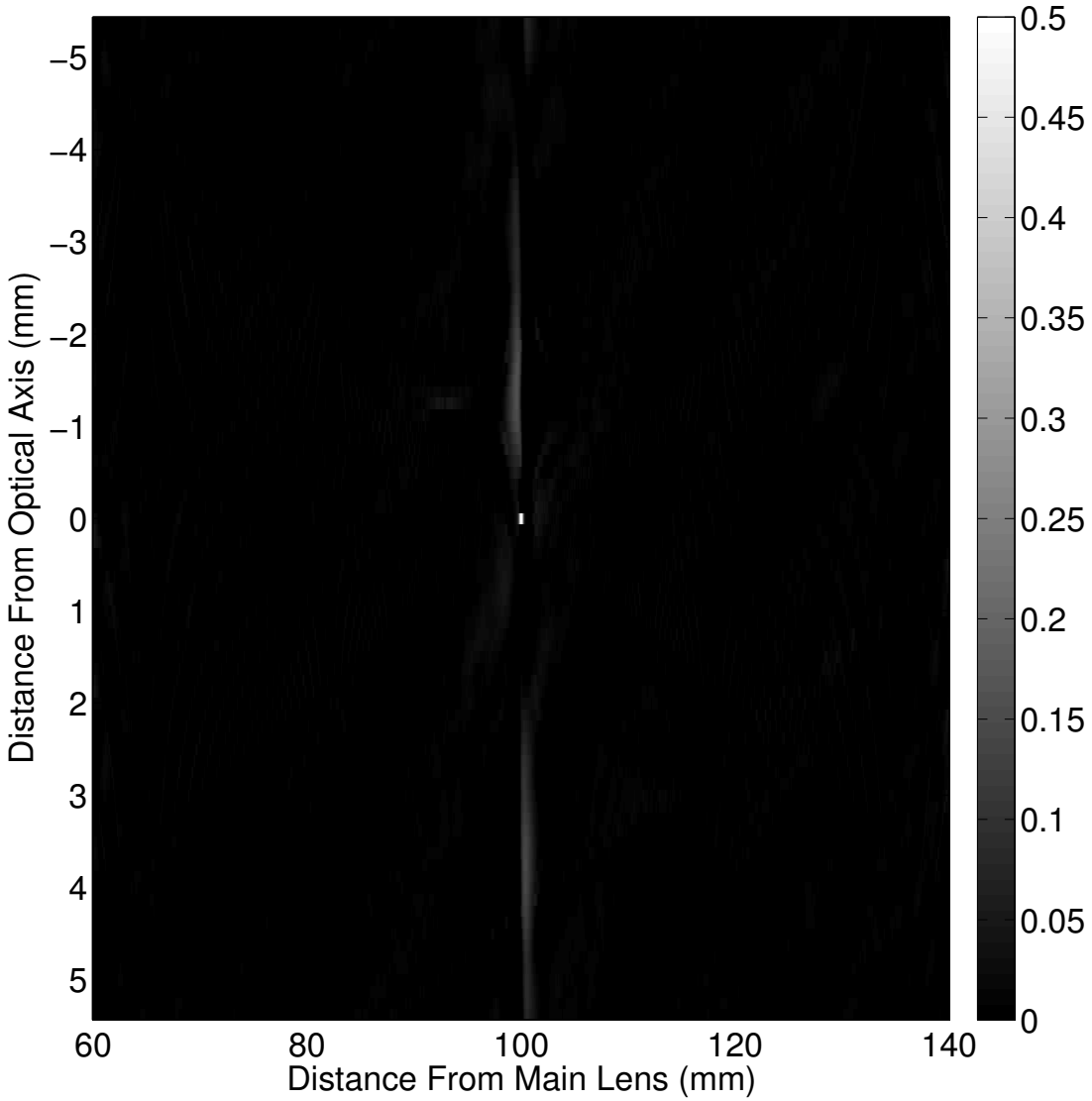

Figure 2.10: Deconvolved image with $K = 1 \times 10^{-8}$. Image intensity-scaled for clarity.

and again the impact is significant. While each of the points become more clearly identifiable, the deconvolution has introduced blur into the image. This demonstrates that selection of the regularization parameter is critical in producing acceptable results in the deconvolved image. In practice, this parameter can be set experimentally and held constant as long as the imaging conditions remain the same from one acquisition to another.

Unfortunately, selection of the optimal regularization parameter does not ensure complete elimination of artifacts. These can be seen in Fig. 2.11. The deconvolved points display

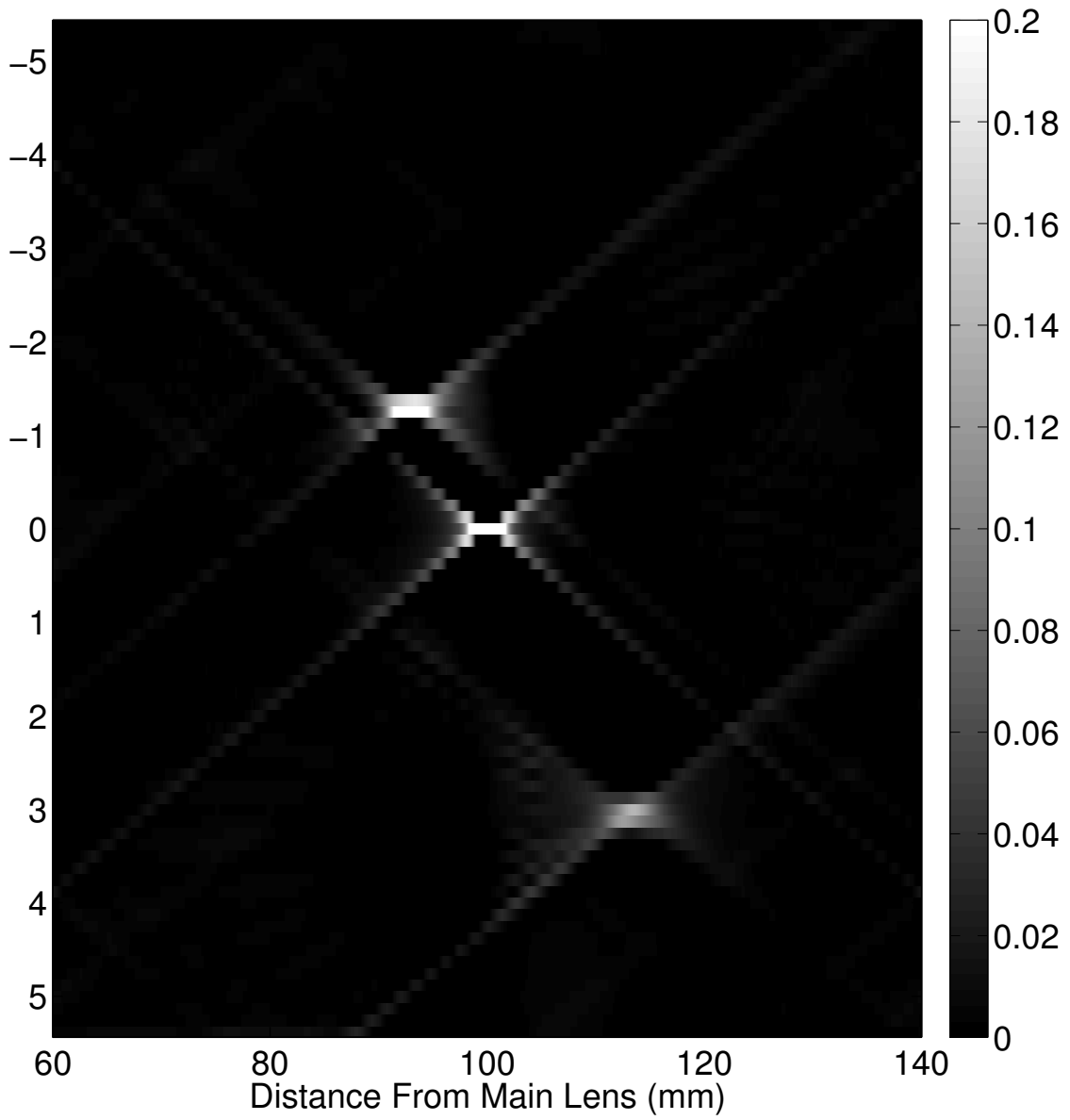

Figure 2.11: Deconvolved image with $K = 1 \times 10^{-4}$. Image intensity-scaled for clarity.

an X-like pattern due in part to the non-invertible nature of the PSF as well as from mismatch between the PSF and the object response. The bottom point displays the persistent banding in the deconvolved image. Both the top and bottom points show the loss of resolution as the points move away from the optical focal plane.. These artifacts cannot be eliminated when implementing a single PSF as the banding phenomena is shift-variant. While techniques exist for addressing spatially variant PSFs [37], they increase the computational burden of the algorithm. Nevertheless, these results show a significant improvement over the estimate

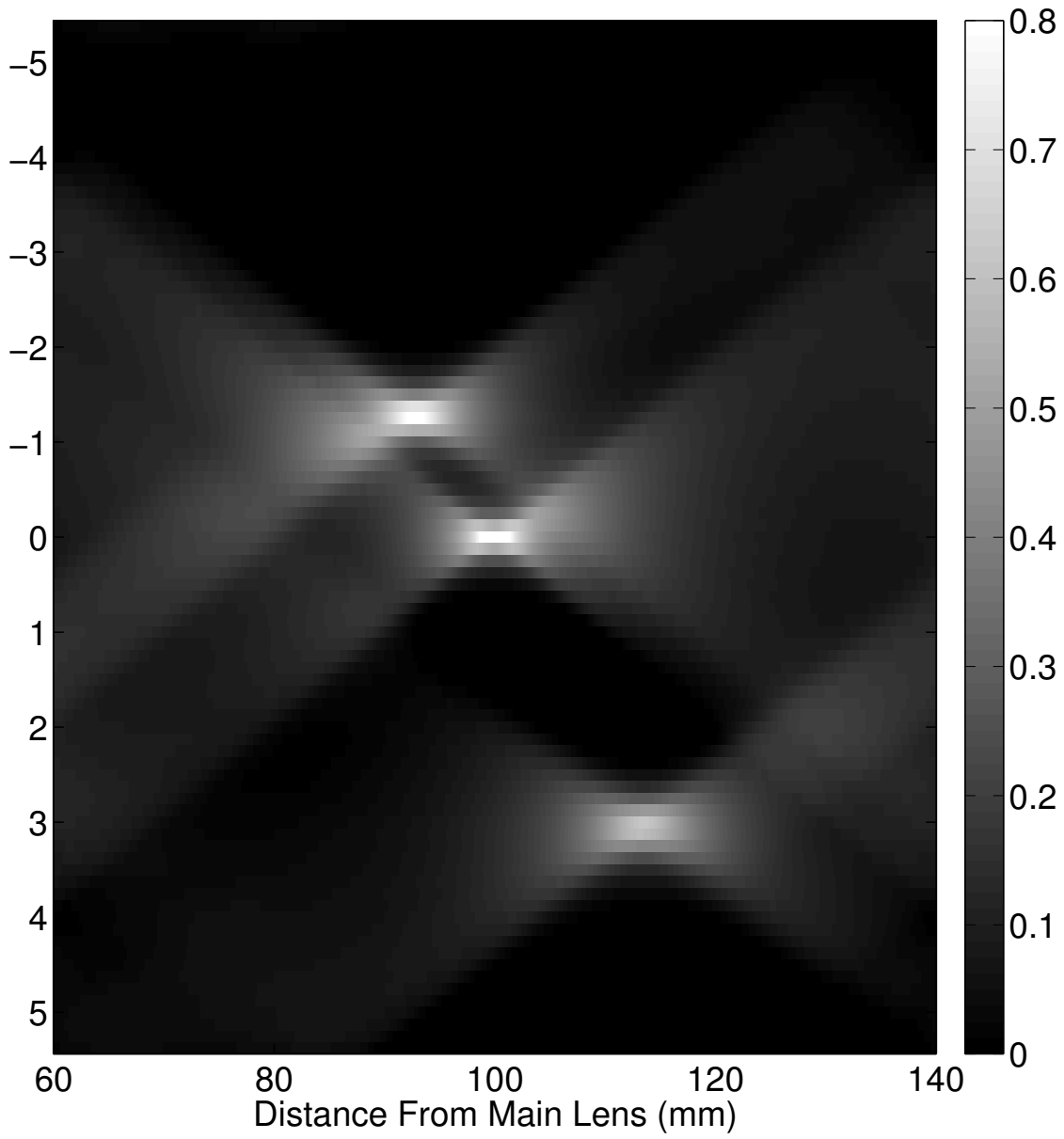

Figure 2.12: Deconvolved image with $K = 0.1$. Image intensity-scaled for clarity.

produced by simply generating a focal stack from the plenoptic data. As a result, we are able to achieve much improved depth resolution after deconvolution processing.

2.2.3 Volumetric Flame Reconstruction

A final experimental case is presented to demonstrate how the system characteristics and artifacts demonstrated in the previous sections impact a volumetric reconstruction with a real-world system. The plenoptic camera parameters are presented in Table 2.2. This configuration places the optical focal plane at 50 cm in front of the camera CCD , or 35.1 mm in front of the camera aperture. For the experiment, two flames are utilized as shown in Fig. 2.13. The first is from a Bunsen burner located to the right of centerline and 6 cm in front of the camera focal plane. The second is from a handheld torch located to the left of centerline and 10 cm behind the camera focal plane. The plenoptic camera is then used to capture an image of both flames burning. The sensor data is shown in Fig. 2.14. Both flames appear blurred in the raw image as neither flame is on the optical focal plane.

Table 2.2: Plenoptic Camera Parameters

Lenslet Focal Length	f_l	0.500 mm
Lenslet Pitch	p_l	0.125 mm
Pixel Pitch	p_p	0.0074 mm
Number of Pixels	n_p	3280×4904
Sensor Size		24 mm $\times$ 36 mm
Number of Lenslets	n_l	193×289
Main Lens Focal Length	f_m	100 mm

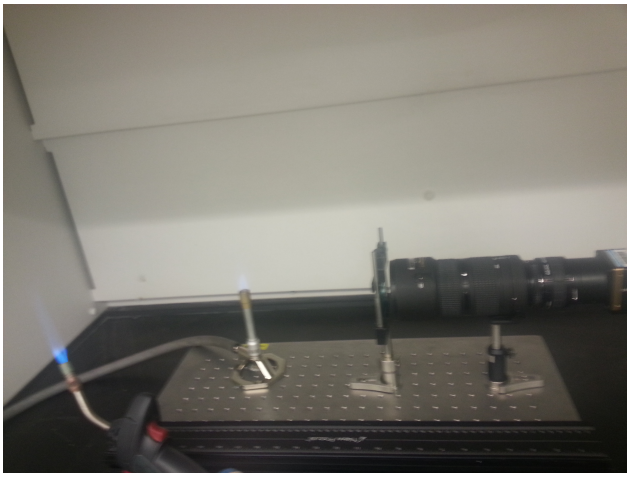

Figure 2.13: Experimental setup showing the plenoptic camera and the two flames being imaged.

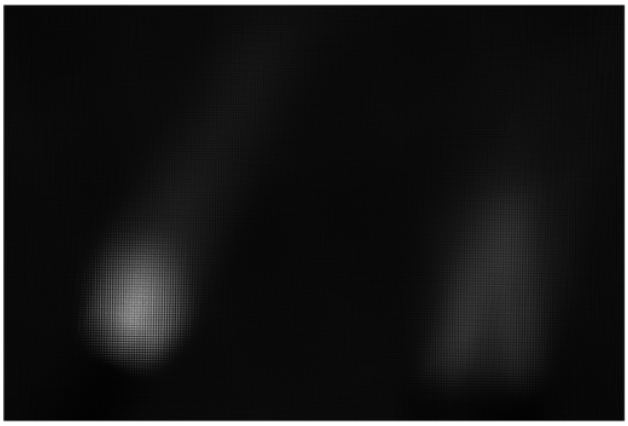

Figure 2.14: Sensor data obtained by imaging the experimental setup.

Next, a PSF must be selected. Many possibilities exist for creating a PSF including imaging a small light source such as a fiber optic light and generating the resulting focal stack. This poses challenges with regard to adequate light collection and preventing imaging the fiber optic cable as well. For this reconstruction, a PSF is synthesized using (2.25). The windowing function $W(u)$ is used to model the circular aperture of the camera and (x_0'', z_0'') are set to 0. Figure 2.15 shows an (x, y) slice of the PSF at 44 cm and Fig. 2.16 shows an (x, z) slice through the center of the PSF.

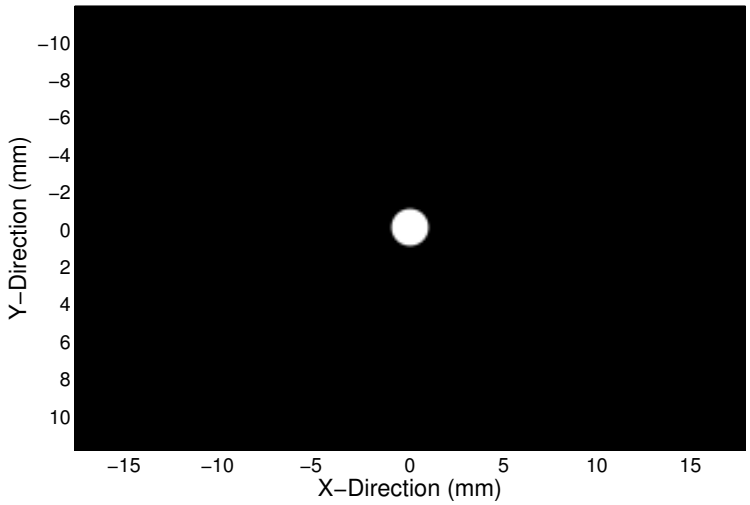

Figure 2.15: Slice of the synthesized PSF along the (x, y) plane at 44 cm. Image intensity-scaled for clarity.

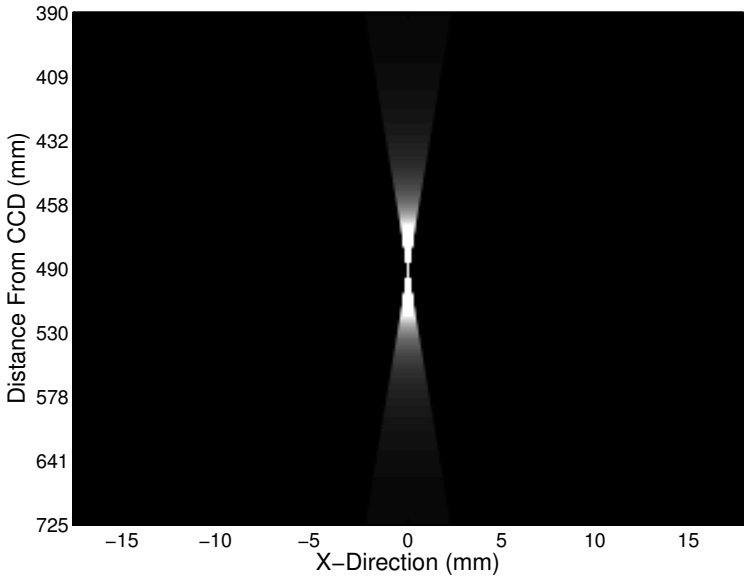

Figure 2.16: Slice of the synthesized PSF along the (x, z) plane through the center of the PSF. Image intensity-scaled for clarity.

The deconvolution begins by creating a focal stack of both the flame image and the PSF. Figure 2.17 shows an (x, y) slice of the volume, a single focal plane, at 44 cm where the Bunsen burner is in focus. This focal plane clearly shows the image blur resulting from the torch flame 16 cm further from the camera. In a blur-free image, we would expect to see only the in-focus Bunsen burner flame on the right side of the image. An (x, z) slice through the flames shown in Fig. 2.18 provides another view demonstrating how the energy from each flame is spread into adjacent focal planes. Again, in the absence of image blur, each flame would be localized to the planes where the flame is present, rather than smeared into adjacent planes as shown in the figure. Note that the scaling of the z-axis is the result of choosing a linear spacing between image-space samples, which results in a nonlinear sampling in object space. Sample spacing in object space is determined using the thin lens approximation

$$\frac{1}{f_m} = \frac{1}{s_i} + \frac{1}{s'} \tag{2.34}$$

where s_i is the image distance and s' is the object distance and f_m is the main lens focal length.

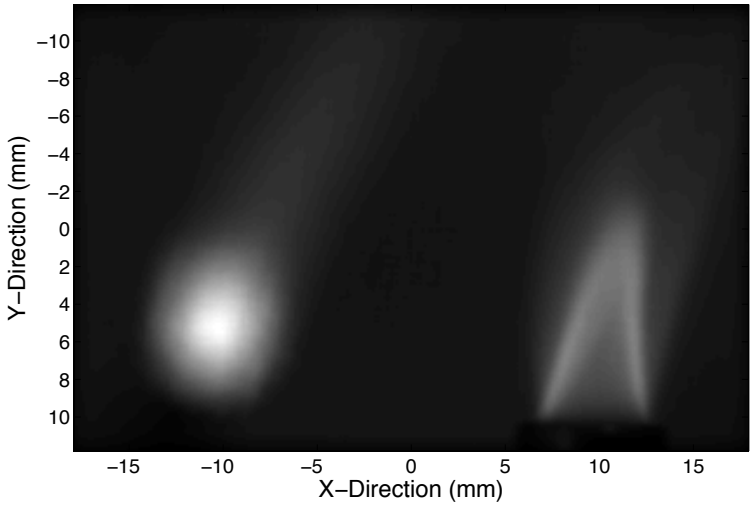

Figure 2.17: Slice of the focal stack along the (x, y) plane at $z = 44$ cm.

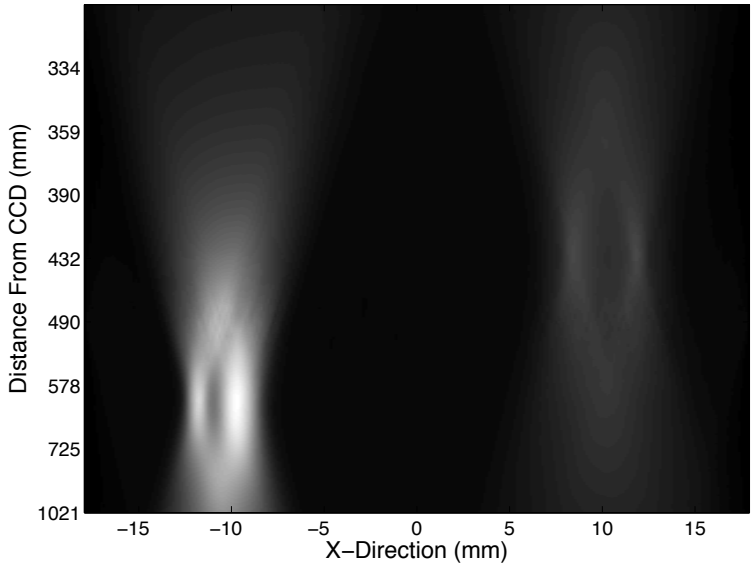

Figure 2.18: Slice of the focal stack along the (x, z) plane at $y = 6.1$mm depicting image blur in the z-direction.

Performing the deconvolution and considering the same (x, y) and (x, z) slices as before shows a significant reduction in out-of-plane energy. Of particular note, the blur from the torch flame is almost completely eliminated in the (x, y) slice at 44 cm shown in Fig. 2.19, while the structure of the Bunsen burner flame is now well defined. Examining the same (x, z) slice as before shows how the image blur is drastically reduced in the z-direction in Fig. 2.20, and again, the structure of the flames is well defined in-plane. The out-of-plane

blur is not completely removed in the reconstruction, which is due to the non-invertibility of the PSF as well as mismatch between the PSF and the object response.

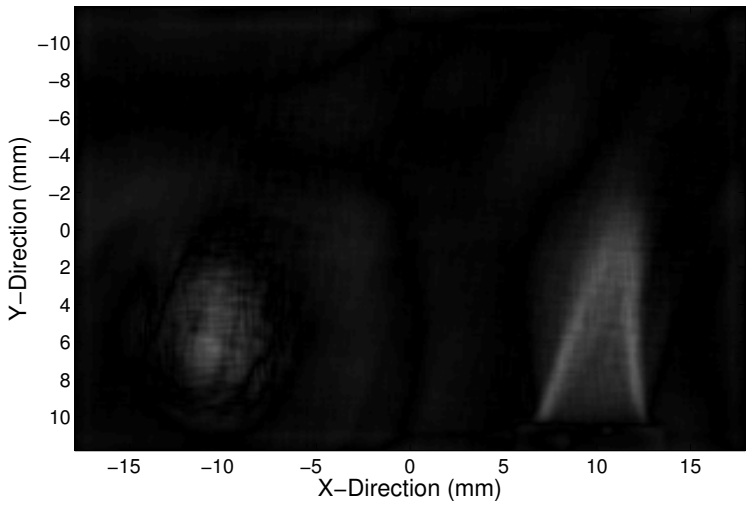

Figure 2.19: Slice of the deconvolved volume along the (x, y) plane at $z = 44$ cm. Image intensity-scaled for clarity.

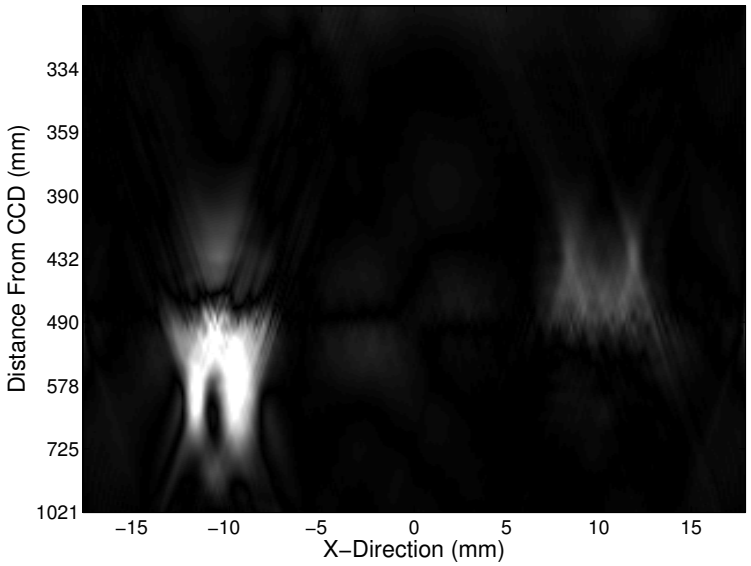

Figure 2.20: Slice of the deconvolved volume along the (x, z) plane at $y = 6.1$mm depicting the reduced blur in the z-direction.

Wiener filtering is know to be sensitive to PSF error, therefore, an additional case is presented where an alternate PSF is used. For this reconstruction, the PSF is simulated utilizing the data from the imaged scene. When viewed closely, the pixels associated with

each microlens can be identified across the camera sensor. A subset of the pixels from the central portion of Fig. 2.14 is shown in Fig. 2.21. The pixel values are normalized in the subset to clearly show the illuminated pixels. The sensor response to a point source can be simulated by first realizing that a point centered on the optical focal plane, centered on one of the micro-lenses shown in Fig. 2.21 will illuminate all of the underlying pixels uniformly. The sensor response is then simulated by choosing a centrally located micro-lens, setting the associated pixels to the maximum value, and setting the remaining sensor pixels to zero. The result is shown in Fig. 2.22.

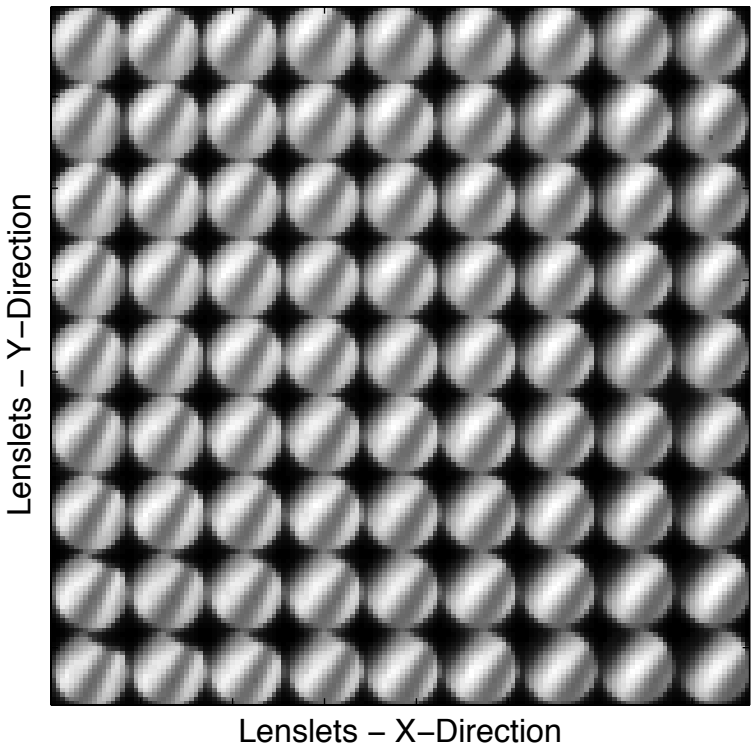

Figure 2.21: Subset of the camera sensor data showing the pixels illuminated underneath each lenset.

The significance of this approach is the PSF is generated by creating a focal stack using the refocusing algorithm as opposed to being purely synthesized as before. As a result, the PSF will exhibit the same shift-variant artifacts as the object focal stack. The deconvolution is performed as before, and the (x, y) and (x, z) slices are compared to those of the result achieved using the analytically derived PSF in Fig. 2.23. The PSF synthesized from the

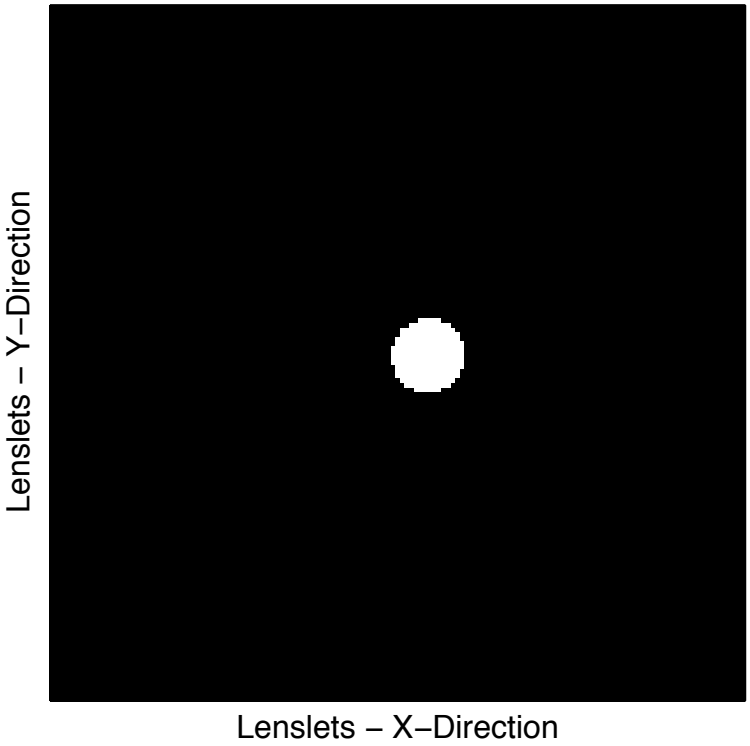

Figure 2.22: Simulated sensor data used for PSF generation.

image data yields results comparable to those achieved using an analytically derived PSF. Comparing Fig. 2.23(a) and (b) shows there is slightly less residual energy remaining from the torch in figure (b). However, figures (c) and (d) show that this may not be the case for all planes. This result is reassuring as it demonstrates that the algorithm can tolerate PSF mismatch gracefully.

The deconvolution for the 3D case presented required less than 10 seconds on a typical laptop without the benefit of parallel processing. Unfortunately, the integral-based refocusing algorithm used to generate the focal stacks for both the example volume and the synthesized PSF is processor-intensive and can require an order of magnitude more time to complete. This algorithm is easily parallelizable, and such algorithms have been demonstrated in our lab to generate similar focal stacks twice as fast as a non-parallel algorithm. Nonetheless, a faster method is desirable, and Fourier-based refocusing algorithms can significantly reduce the total time required to generate an estimate of the imaged volume.

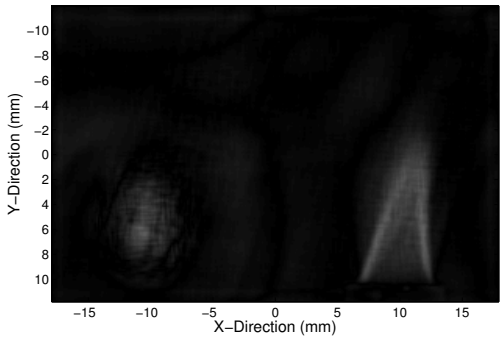

(a) Deconvolution using analytically derived PSF

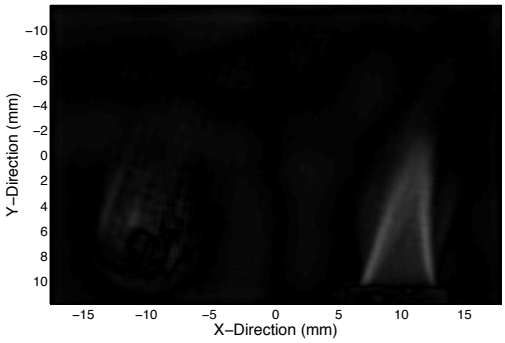

(b) Deconvolution using PSF synthesized from image data

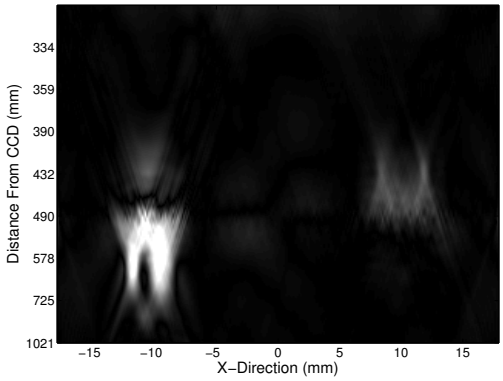

(c) Deconvolution using analytically derived PSF

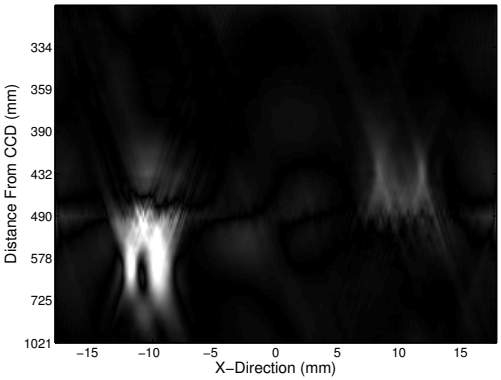

(d) Deconvolution using PSF synthesized from image data

Figure 2.23: Comparison of deconvolution results when a analytically derived PSF is used vs. a PSF synthesized from the image data.

Chapter 3

Direct FFT-Based Volumetric Reconstruction from Plenoptic Data

Deconvolution has been shown to be a practical method of reducing 3D blur in plenoptic reconstructions, but its efficiency is limited by the computational overhead required in generating the focal stack when utilizing integral-based refocusing methods [38]. Separately, FFT-based refocusing methods have proved to be much faster than integral-based alternatives [2]. This work combines FFT-based deconvolution and FFT-based light-field processing techniques in a unique way to yield volumetric reconstructions. The characteristics of the algorithm are identified and compared to those of integral-based methods. The algorithm efficiency is further improved by calculating the estimate of the 3D spectrum directly, eliminating the intermediate step of calculating the spatial-domain focal stack–refer to Fig. 3.1. To demonstrate the efficacy of the algorithm, a 3D volume is reconstructed from experimental data and compared to the corresponding focal stack.

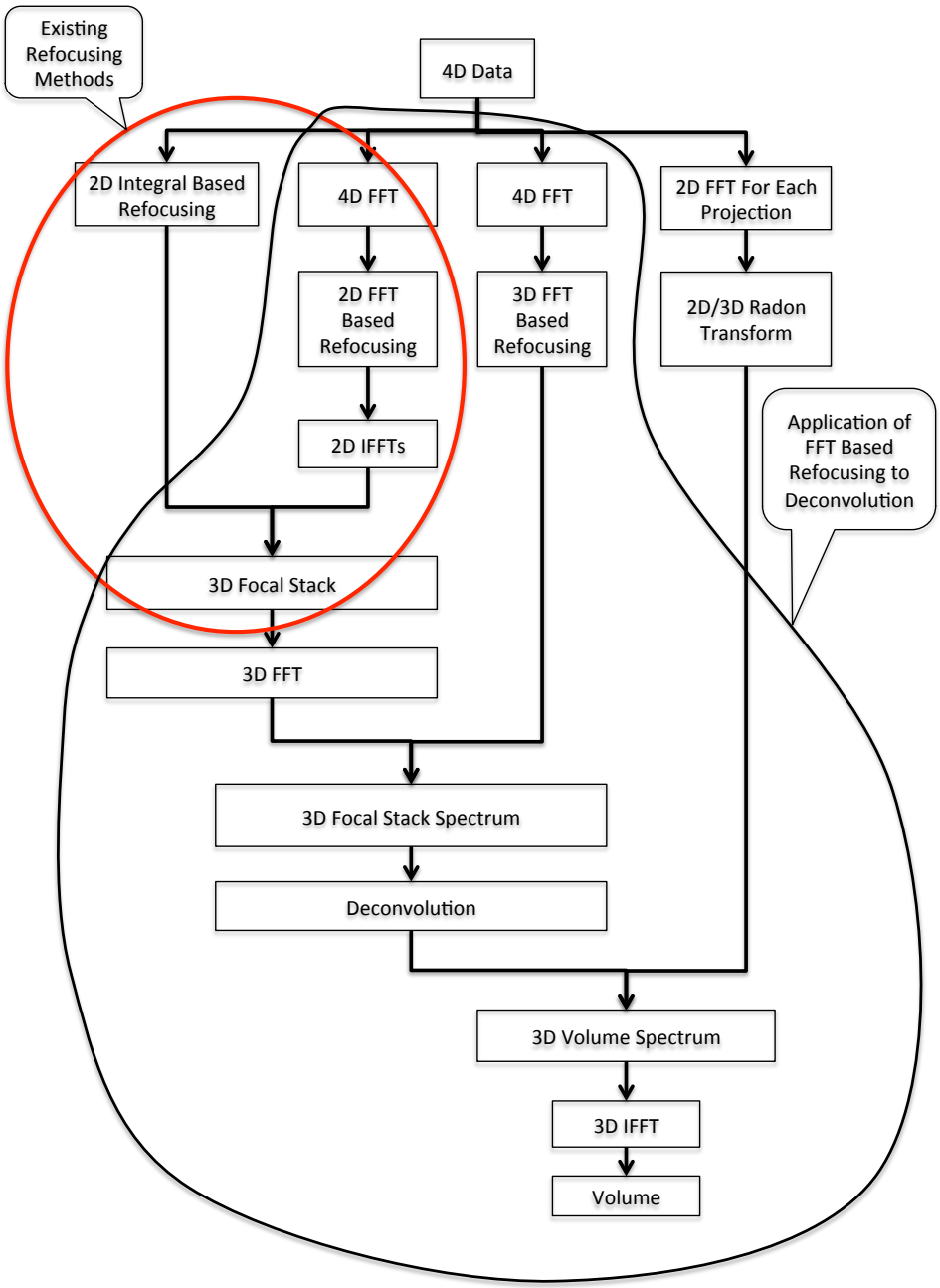

Figure 3.1: Flow chart indicating the application of deconvolution to existing FFT-based refocusing techniques as well as elimination of the intermediate step of calculating the focal stack.

3.0.4 FFT-Based Image Synthesis

While integral-based image synthesis is the most intuitive approach, refocusing a light-field image can also be accomplished through application of the Fourier Slice Theorem [39]. The spectrum of a 2D image at an arbitrary focal plane is obtained by taking a slice of the 4D light field at different angles in the frequency domain [1]. The frequency domain spectra can be computed quickly and efficiently using FFTs. As a result, FFT-based refocusing algorithms offer a significant improvement in speed when computing multiple images.

Integral-based refocusing requires $O(n^2m^2)$ operations *for each focal plane*, where n spatial and m angular samples are assumed in each dimension. Compare this to Fourier-slice refocusing, which requires $O(n^2m^2 \log n^2m^2)$ operations for the initial 4-D FFT but only $O(n^2 \log n^2)$ for the inverse 2-D FFT necessary to produce each image. When producing a single focal plane, the use of FFT-based processing offers little benefit due to the overhead associated with the initial 4-D FFT.

However, when cast in the context of deconvolution, multiple focal planes must be generated, which can each be calculated from the single 4-D FFT of the plenoptic data. Furthermore, It will be shown that angular oversampling is typically necessary to achieve acceptable results when using integral-based refocusing. Letting j be the angular oversampling rate and k be the number of focal planes, (3.1) gives the number of computations necessary to calculate a focal stack using integral-based refocusing and (3.2) gives the number of computations necessary for FFT-based refocusing. When considering angular oversampling, using FFT-based processing can yield reduction in processing time of two orders of magnitude when generating a focal stack.

$$O\left\{k(n^2(jm)^2)\right\} \tag{3.1}$$

$$O\left\{(n^2m^2)\log n^2m^2 + kn^2 \log n^2\right\} \tag{3.2}$$

Our study shows that integral-based refocusing algorithms are *not* equivalent to FFT-based refocusing algorithms. The results of each algorithm exhibit unique characteristics that result in spatial variability.

3.0.5 FFT-Based Image Synthesis Equations

Synthesis of a 2D image at an arbitrary focal plane F' along the z-axis begins with the same irradiance equation used for integral-based refocusing—repeated in (3.3) for convenience.

$$E_{\alpha F}(x', y') = \frac{1}{\alpha^2 F^2} \iint L_F \left(u \left(1 - \frac{1}{\alpha} \right) + \frac{x'}{\alpha}, v \left(1 - \frac{1}{\alpha} \right) + \frac{y'}{\alpha}, u, v \right) \mathrm{d}u \, \mathrm{d}v \tag{3.3}$$

Expressing the irradiance in terms of the operator $\mathcal{H}$ gives

$$\begin{aligned} \mathcal{H}_\alpha \left[L_F \right] (x', y') &= E_{\alpha F}(x', y') && (3.4) \\ &= \frac{1}{\alpha^2 F^2} \iint L_F \Bigg(u \left(1 - \frac{1}{\alpha} \right) + \frac{x'}{\alpha}, \\ &\quad v \left(1 - \frac{1}{\alpha} \right) + \frac{y'}{\alpha}, u, v \Bigg) du dv. && (3.5) \end{aligned}$$

Equation (3.5) is implemented by first reorganizing the 2D sensor data into the 4D radiance array where two dimensions of the array correspond to the spatial samples and the remaining dimensions correspond to the angular samples. This groups the angular samples with the corresponding spatial samples. Figure 1.6 depicts the process for the 2D case. With the data collected in this way, generating the intensity for a point at a particular focal plane becomes a matter of selecting a slice of the radiance array and summing the sampled values. While (3.5) is used for integral-based refocusing, it also provides the basis for Fourier slice refocusing as presented by Ng [1]. The Fourier slice theorem relating a 2D image ($M = 2$)

to 4D plenoptic data ($N = 4$) is

$$\mathcal{F}^2 \circ \mathcal{I}_2^4 \circ \mathcal{B}_\alpha = \mathcal{S}_2^4 \circ \frac{\mathcal{B}_\alpha^{-T}}{|\mathcal{B}_\alpha^{-T}|} \circ \mathcal{F}^4 \tag{3.6}$$

where $\mathcal{F}^M$ represents the M-D Fourier transform, $\mathcal{I}_M^N$ represents the projection from M to N, $\mathcal{S}_M^N$ represents the slicing operation whereby the last $N - M$ dimensions of a function are set to 0, and $\mathcal{B}_\alpha$ is the shearing operator. Here, $\mathcal{B}_\alpha$ is given by

$$\mathcal{B}_\alpha = \begin{pmatrix} \alpha & 0 & 1-\alpha & 0 \\ 0 & \alpha & 0 & 1-\alpha \\ 0 & 0 & 1 & 0 \\ 0 & 0 & 0 & 1 \end{pmatrix}.$$

A 2D image at an arbitrary focal plane can then be synthesized via

$$E_{\alpha F} = \mathcal{F}^{-2} \circ \frac{\mathcal{S}_2^4}{F^2} \circ \mathcal{B}_\alpha^{-T} \circ \mathcal{F}^4. \tag{3.7}$$

Equation (3.7) is implemented by first letting $\mathcal{R}$ denote the 4D FFT of the radiance array. The 2D slice of $\mathcal{R}$ corresponding to the 2D FFT of the desired focal plane is then given by

$$\mathcal{F}^2[E_{\alpha F}](k_x, k_y) = \frac{1}{F^2}\mathcal{R}(\alpha k_x, \alpha k_y, (1-\alpha)k_x, (1-\alpha)k_y). \tag{3.8}$$

The spatial-domain image is then given by simply taking the 2D IFFT of the slice given by (3.8).

3.1 Theory of FFT-based Volume Reconstruction

It is important to note that (3.8) is the Fourier slice *photograph* theorem. These equations produce a photograph refocused to an arbitrary focal depth, which includes the out-of-plane energy associated with image blur. Furthermore, as presented by Ng [1], both the

integral-based and Fourier-based refocusing algorithms shown above are inherently shift-variant. Section 2.1 demonstrates that the integral-based relationships can be modified to achieve a shift-invariant response in the continuous case. The resulting imaging equation is

$$E_{\alpha F}(x'', y'') = \frac{1}{\alpha^2 F^2} \iint L_F \Big(u(\alpha - 1) + x'', \\ v(\alpha - 1) + y'', u, v \Big) du dv. \tag{3.9}$$

This modification is a scaling applied to the shearing function and will subsequently yield a shift-invariant form of the Fourier slice photograph theorem. The modified shearing function is given by

$$\mathcal{B}_\alpha = \begin{pmatrix} 1 & 0 & 1-\alpha & 0 \\ 0 & 1 & 0 & 1-\alpha \\ 0 & 0 & 1 & 0 \\ 0 & 0 & 0 & 1 \end{pmatrix}.$$

The implementation is the same as shown in (3.8) where the modified shearing function is utilized for calculating the desired slice of the 4D radiance array spectrum by

$$\mathcal{F}^2[E_{\alpha F}](k_x, k_y) = \mathcal{R}(k_x, k_y, (1-\alpha)k_x, (1-\alpha)k_y). \tag{3.10}$$

Typically, (3.10) is used to create a single 2D image at the desired focal plane. Processing in this manner is faster than integral-based refocusing. However, the efficiency improvements are compounded when calculating a 3D focal stack, as the initial 4D FFT must be calculated only once. Each focal plane can then be calculated from the spectrum of the radiance array. Creating a stack of these 2D spectra—where each vertical slice corresponds to the spectrum of the corresponding spatial-domain focal stack plane—provides a great deal of insight into the characteristics of FFT-based refocusing. To illustrate, the simulated sensor

and corresponding radiance array data shown in Fig. 1.6 is again used (repeated as Fig.3.2 for convenience). The 2D FFT of the radiance array shown in Fig. 3.2 (right) is presented in Fig. 3.3 (top). A slice of the radiance array spectrum is identified, and the position in the spectral stack is shown in Fig. 3.3 (bottom). Creating the spatial-domain focal stack from this data is simply a matter of taking the 1D FFT along each vertical plane of the spectral stack. While computationally efficient to calculate, the focal stack remains a poor estimate of the volume. Deconvolution provides a method of removing this 3D blur while further leveraging FFT-based processing to reduce the computational burden and improve the speed of reconstruction. Furthermore, when deconvolution is to be applied for deblurring, calculating the spatial-domain focal stack is not necessary.

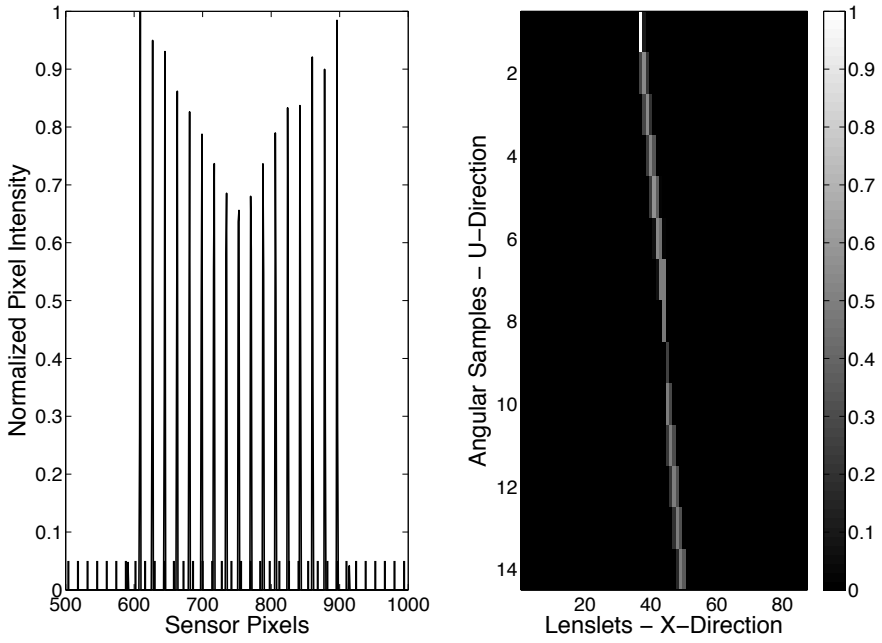

Figure 3.2: Simulated sensor data with micro-lens locations indicated across the bottom (left) and the corresponding radiance array (right) for a point 9 mm in front of the optical focal plane.

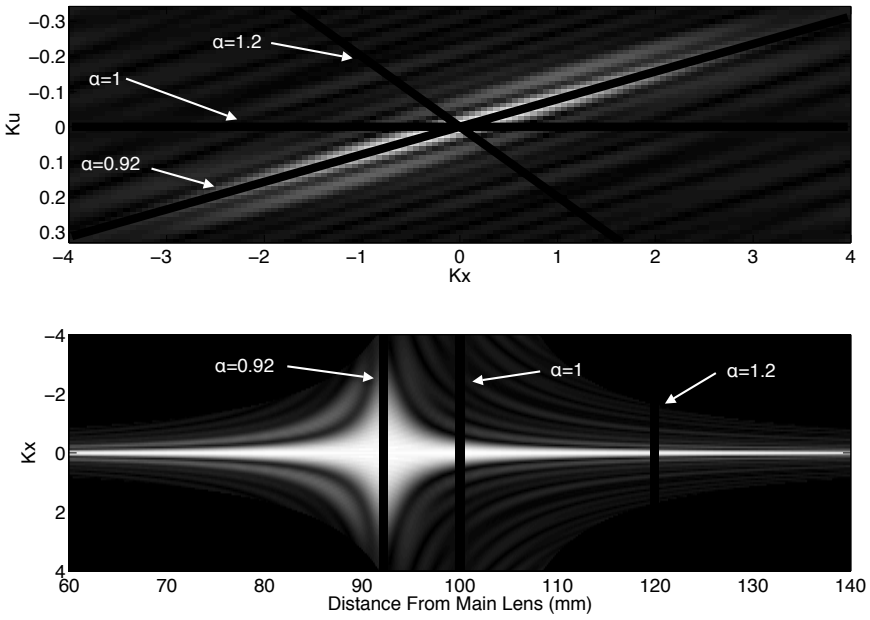

Figure 3.3: 2D FFT of radiance array (top) and the spectrum associated with each plane of the focal stack (bottom). Slices of the radiance array spectrum and the corresponding positions in the spectral stack are shown.

Comparison of Integral and FFT-based Image Synthesis Characteristics

A significant source of spatial variability in integral-based refocusing arises from banding due to the manner in which the radiance array is sampled to build the refocused image—refer to Section 2.1. An example of this banding can be seen in Fig. 3.4, where a focal stack for a point at the optical focal plane is generated using both integral-based processing (top) and FFT-based processing (bottom). The FFT-based PSF is much smoother, with greatly reduced banding.

The cause of this difference can be seen by comparing the spectral stack of the integral-based PSF to the FFT-based PSF as shown in Fig. 3.5. The spectral stack for the integral-based PSF (top) contains considerable high-frequency information near the corners of the figure. This is the result of aliasing due to undersampling the radiance array during image reconstruction. This artifact can be greatly reduced in integral-based refocusing by over-sampling the data. However, oversampling further increases the computational burden of an already computationally intensive algorithm. Contrast this to the spectral stack for the

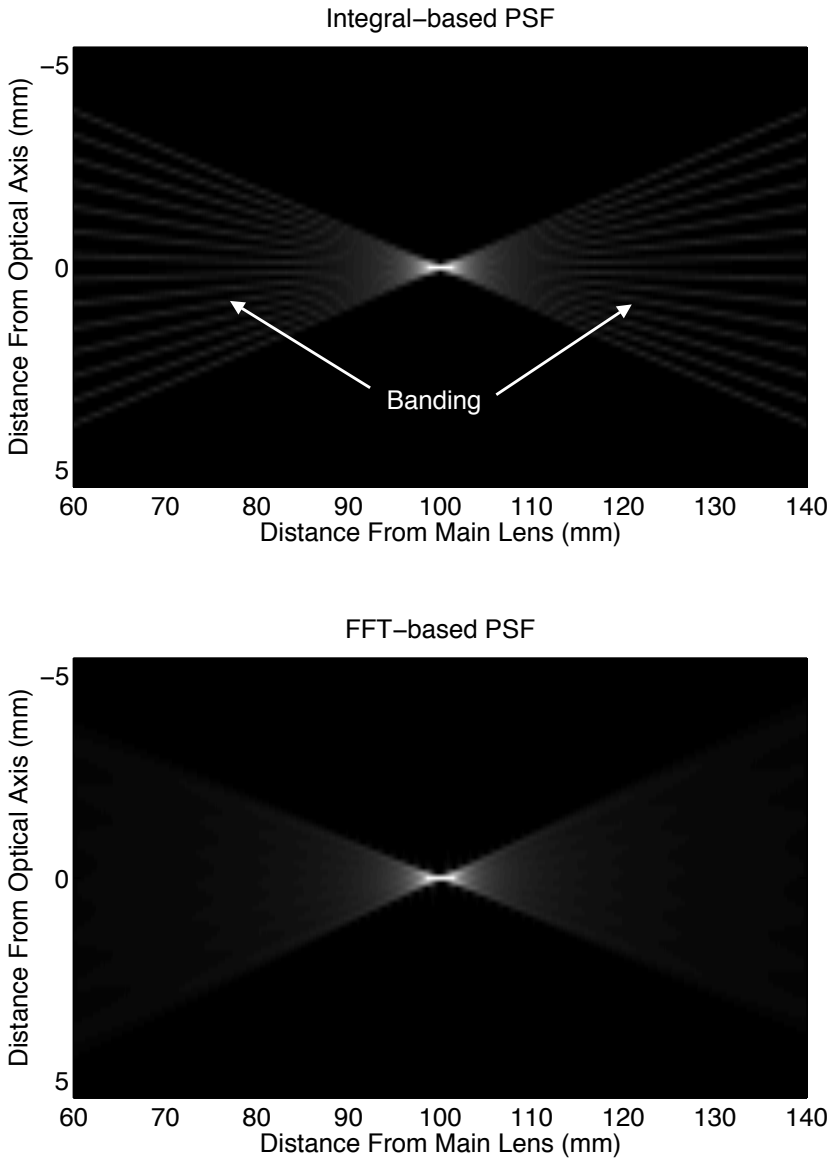

Figure 3.4: PSF generated by integral-based refocusing (top) and the PSF for the same point generated via FFT-based refocusing (bottom). Both figures intensity-scaled for clarity.

FFT-based PSF (bottom), where this high-frequency information is completely absent. This indicates that as the image is refocused further from the optical focal plane, the FFT-based refocusing algorithm begins to truncate the higher-frequency content from the spectrum of each focal plane. This truncation coincides with the Nyquist resolution limit given by

$$\frac{|F' - F|}{F'} \leq \frac{\Delta x}{\Delta u} \tag{3.11}$$

where Δx is the spatial sampling rate and Δu is the angular sampling rate [1]. Exceeding this limit results in a loss of resolution in the optimally focused point of the PSF, that is, the center of the PSF becomes slightly blurred as opposed to being perfectly focused. The 2D simulations presented here model a system with $\Delta x = 8\text{mm}^{-1}$ and $\Delta u = 135\text{mm}^{-1}$. Substituting these values into (3.11) and solving for α shows the system can only refocus with optimal resolution between $0.94 \leq \alpha \leq 1.06$ ($94\text{mm} \leq z \leq 106\text{mm}$). While this is a well-known limit for plenoptic imaging, its manifestation in the frequency domain has not been previously explored to the extent presented here.

The absence of the high-frequency information in the FFT-based PSF is the direct result of the limited range of angular samples acquired by the plenoptic camera. Referring to (3.10), we see that the slice of the spectral stack is calculated by setting $k_u = (1 - \alpha)k_x$ and $k_v = (1 - \alpha)k_y$. This slicing operation is demonstrated in Fig. 3.3. Each slice of the radiance array spectrum is taken at a different angle in order to populate the corresponding slice of the spectral stack. When $\alpha = 1$ the slice is taken along the $(k_u, k_v) = 0$ plane, which contains sufficient data to fully populate the spectrum of the corresponding slice of the spectral stack at the optical focal plane. As α increases or decreases, the angle of the slice from the radiance array increases. Once the slice rotates past the *corner* of the radiance array spectrum—that is, the slice rotates into the (k_u, k_v) portion of the spectrum where there is no longer recorded spectral content—the remaining values are then zero. At that point, the spectrum is truncated. The range of potential k_u and k_v values necessary to populate the selected spectral slice is set by the range of k_x and k_y samples in the radiance array spectrum. Because the extent of spatial samples is typically much greater than the extent of angular samples in a plenoptic camera, the spectral extent will be much greater in the spatial directions. This leads to a situation where focusing too far on either side of the optical focal plane requires spectral content outside the range of spectral support in the angular dimension.

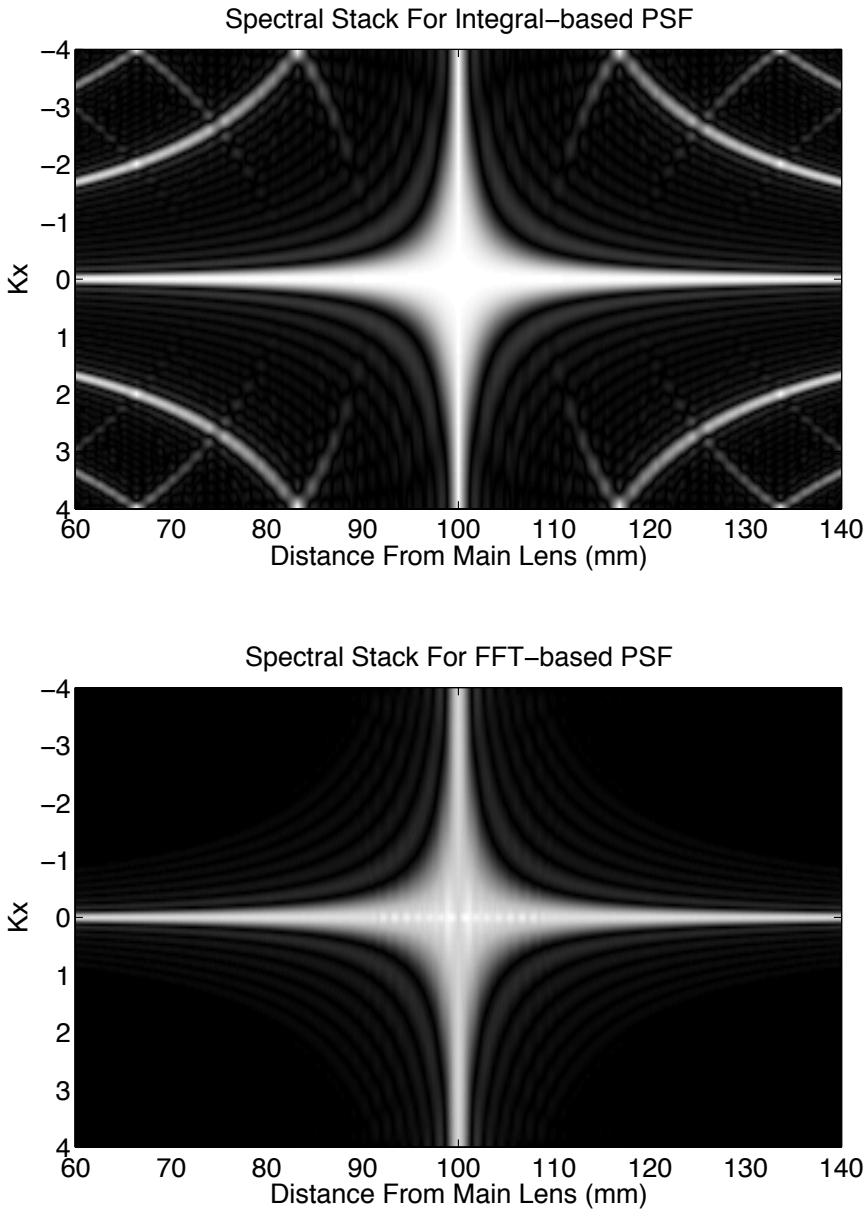

Figure 3.5: Spectral stacks consisting of the 1D FFT of each focal plane from the integral-based PSF (top) and FFT-based PSF (bottom) shown in Fig. 3.4. Note the absence of high-frequency content in the corners of the (bottom) figure.

The combination of shifting the FFT-based PSF away from the optical focal plane and truncation of the spectrum leads to an additional source of shift variance where the spectral stack becomes asymmetric. To demonstrate, the example PSF at 9 mm away from the optical focal plane is again used and is shown in Fig. 3.6 (top) along with the spectral stack (bottom). Note that the spectral stack consists of the 1D FFT associated with each focal

plane. Therefore, the ideal PSF would have a symmetric spectral stack about the in-focus plane. However, once the PSF is shifted away from the optical focal plane, the spectrum is truncated asymmetrically. Because the high-frequency components are not symmetric about the in-focus plane, the resulting banding oscillates between light and dark regions at a different frequency which can be seen in Fig. 3.6 (top).

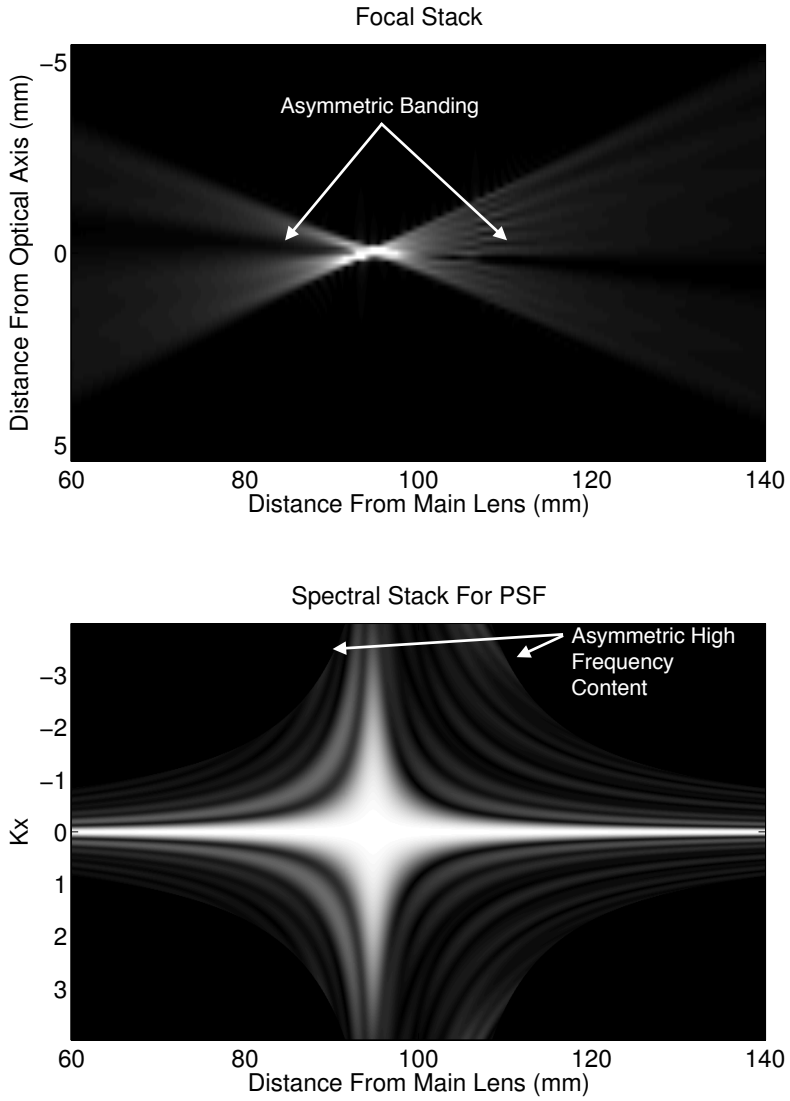

Figure 3.6: Focal stack for a point 9mm in front of the optical focal plane (top—intensity-scaled for clarity) and corresponding spectral stack (bottom).

Finally, this absence of high-frequency content as the image is focused further from the optical focal plane results in a loss of resolution once α exceeds the limits set by (3.11). Once

the Nyquist resolution limit is exceeded, the spatial resolution of the refocused PSF is no longer set by the light-field sensor $W_x/\Delta x$ but is now set by

$$\frac{\alpha W_x}{|1-\alpha|\,\Delta u} \tag{3.12}$$

where W_x is the width of the camera sensor [1]. Again, considering the spectral stack of an example PSF offers insight into the source of this reduced resolution. Figure 3.7 shows a PSF centered at 88 mm, which is outside the Nyquist limit of $94\text{mm} \leq z \leq 106\text{mm}$ for the simulated system. The slice of the spectral stack in Fig. 3.7 corresponding to the optimal focal plane of the PSF is truncated, resulting in a wider pulse width in the spatial domain. As the PSF is moved further from the optical focal plane, and further outside the Nyquist resolution limit, less high-frequency content is available, further reducing the PSF resolution at the in-focus plane.

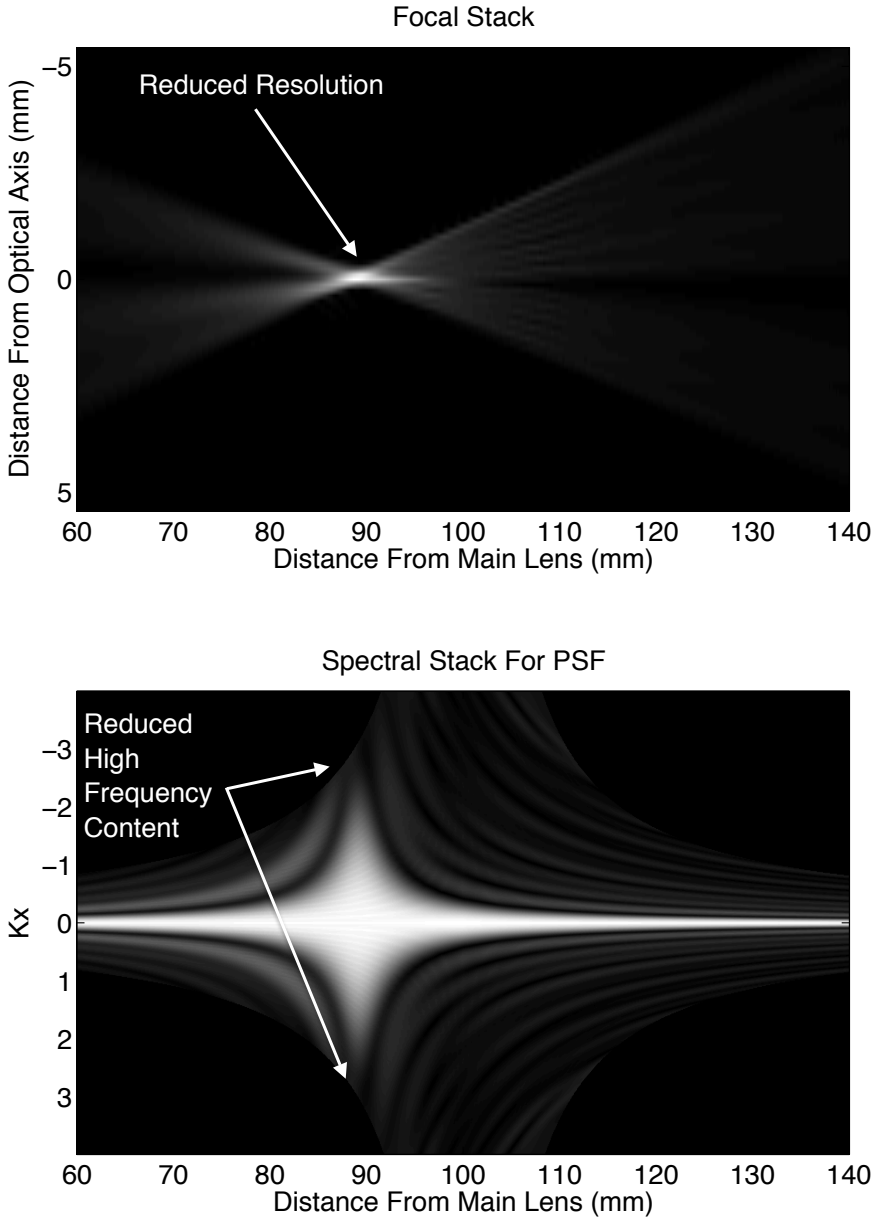

Figure 3.7: Focal stack for a point at 88mm (top) and corresponding spectral stack (bottom). Note the reduced resolution in the PSF (top) resulting from the truncated high-frequency content in the corresponding plane of the spectral stack (bottom).

3.1.1 FFT-based Image Synthesis Characteristics

Many aspects of FFT-based image synthesis lead directly to artifacts in the resulting images that are not seen in integral-based image synthesis. These must be considered when deconvolution is the goal, as these artifacts can lead to spatial variability and PSF mismatch. While [2] and [1] offer guidelines for the technique, exploring the spectrum and resulting

artifacts associated with the PSF offers greater insight into the algorithm, resulting artifacts, and potential sources of shift variance. Ultimately, the results shown here indicate the parameters used in [2] and [1], which concentrate more on refocusing, may not be optimal for deconvolution.

2D Simulations

To demonstrate the various artifacts, the 2D FFT of the radiance array and the corresponding spectral stack for the point at 9mm are again used. However, the previous radiance array spectrum and spectral stack for this point shown in Fig. 3.3 were generated by first zero-padding the radiance array with 400 zeros in each dimension. Simply zero-padding the radiance array before the FFT increases the number of data points in the spectrum through interpolation. While this technique does not *create* data, it does provide a smoother data set to sample from. To clarify, Fig. 3.8 repeats the 2D FFT of the radiance array from Fig. 3.3, which is padded by 400 zeros in each dimension, along with the 2D FFT of the same radiance array with no padding.

While these two figures appear quite different, they are in fact the result of the same underlying data. The top figure simply contains more points, where the additional points are obtained via zero-padding of the radiance array before performing the FFT. However, digital refocusing can be thought of as simply resampling the radiance spectrum, and the results obtained from these two spectra are significantly different. This can be seen by comparing the spectral stacks shown in Fig. 3.9. The top figure shows the spectral stack obtained by resampling the smoothed, interpolated data obtained by first zero-padding the radiance array. The bottom figure shows the spectral stack obtained by resampling the spectrum of the radiance array obtained without zero-padding. The difference between the two spectral stacks is striking though not unexpected when considering the spectrum of the corresponding radiance array. The variation in the bottom spectral stack shown in Fig. 3.9 results in an aliasing artifact shown in Fig. 3.10. These are ringing artifacts resulting from images

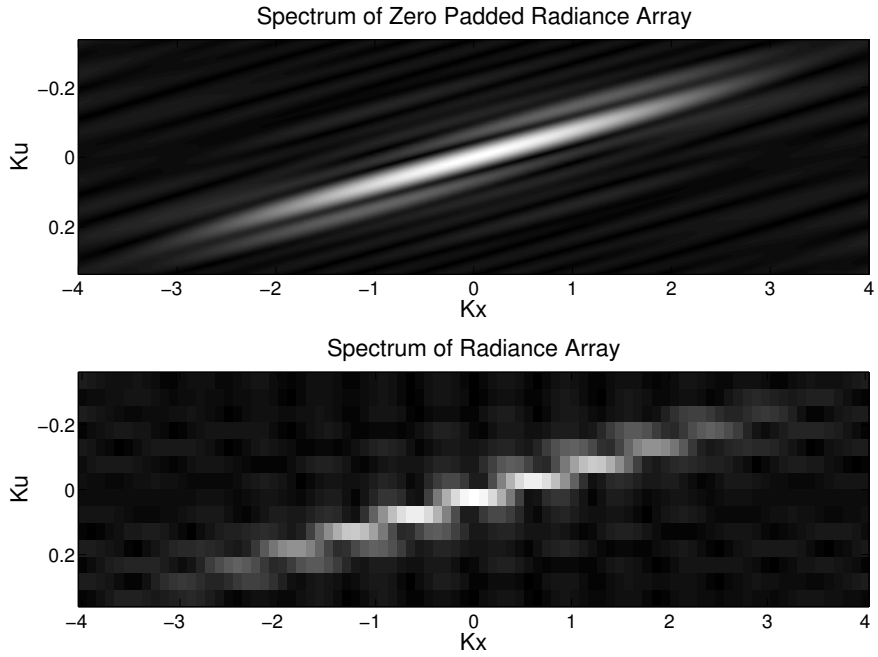

Figure 3.8: Spectrum of radiance array padded by 400 zeros prior to FFT (top). Spectrum of radiance array with no zero-padding prior to FFT (bottom). Both spectra are for a point located at 9mm in front of the focal plane.

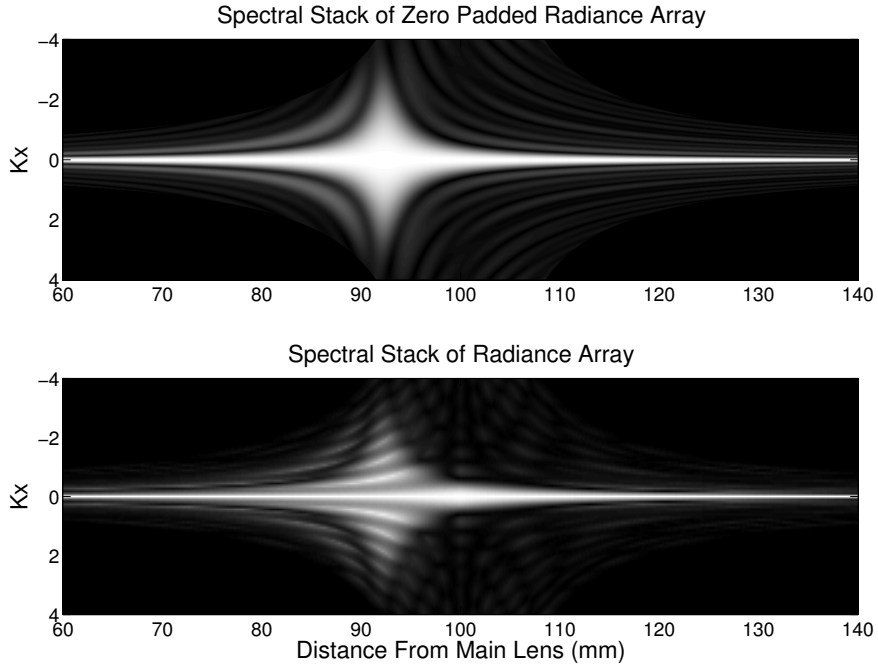

Figure 3.9: Spectral stack obtained from spectrum resulting from zero-padded radiance array (top) compared to the spectral stack obtained from the spectrum resulting from no zero-padding (bottom).

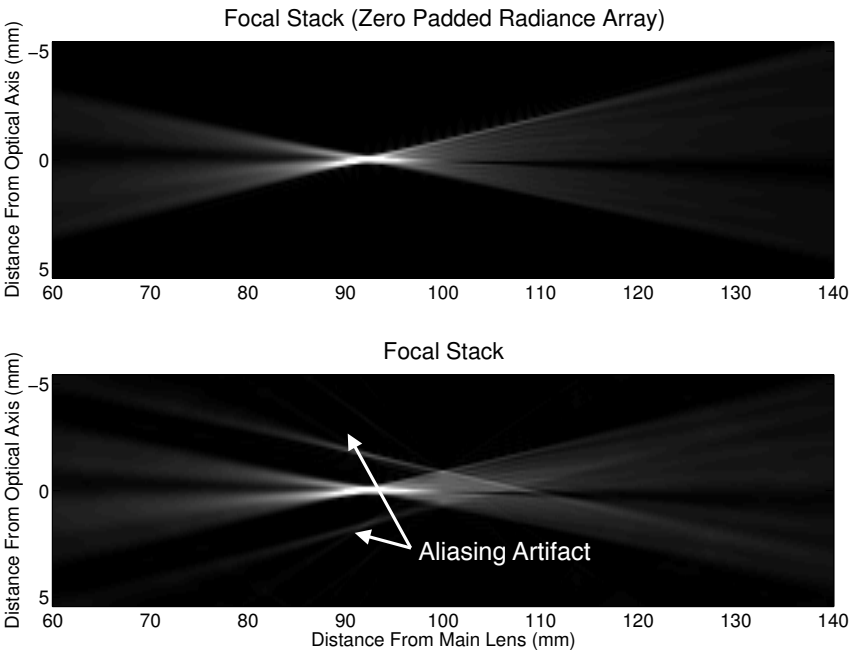

Figure 3.10: Focal stack from zero-padded radiance array (top) and focal stack from radiance array with no zero padding (bottom) exhibiting the resulting aliasing artifact. Both figures intensity-scaled for clarity.

perpendicular to the slicing plane being projected down onto the image plane—referred to as "ghosting" artifacts by [1, 2]. This aliasing artifact is caused by using a resampling filter with finite spatial extent an approximation for the infinite extent ideal filter.

4D Reconstructions

While the 2D simulations provide greater insight into the source of the artifacts, the artifacts themselves become more recognizable when considering a 2D image from actual data. The parameters for the plenoptic camera used in collecting the data are provided in Table 3.1: This configuration places the optical focal plane at approximately 40.25 cm in front of the camera CCD, or 29 cm in front of the camera aperture. To demonstrate the aliasing artifacts, a slice of a PSF at 11.8 cm in front of the camera focal plane is presented in Fig. 3.11. The details of how this PSF is generated are presented in subsequent sections.

Table 3.1: Plenoptic Camera Parameters

Lenslet Focal Length	f_l	0.500 mm
Lenslet Pitch	p_l	0.125 mm
Pixel Pitch	p_p	0.0074 mm
Number of Pixels	n_p	3280×4904
Sensor Size		24 mm $\times$ 36 mm
Number of Lenslets	n_l	193×289
Main Lens Focal Length	f_m	60 mm

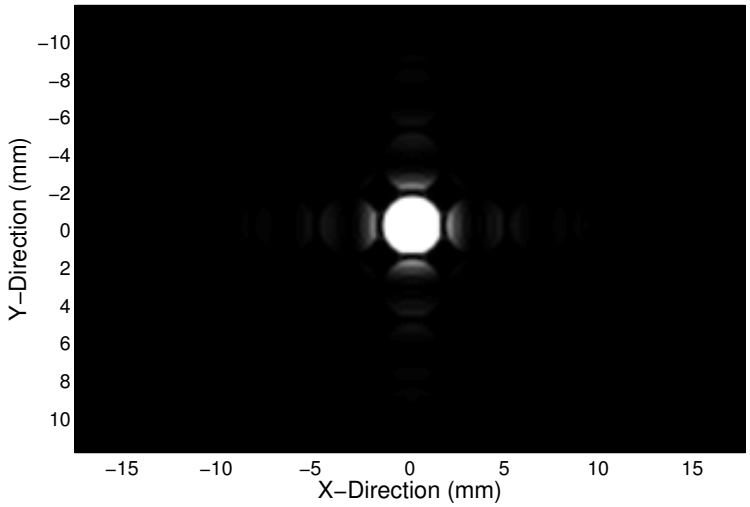

Figure 3.11: Slice of system PSF at 12.6 cm in front of the camera focal plane showing aliasing artifacts resulting from inadequate zero padding. Image intensity-scaled for clarity.

Previous research utilized zero-padding to eliminate aliasing artifacts near the edges of the image and a Kaiser-Bessel resampling window to reduce the ringing artifacts near edges within the image [1, 2]. However, further investigation shows that increasing the oversampling rate above the previously recommended 5% reduces both types of artifacts. Specifically, increasing the zero-padding in the spatial (x, y) direction alleviates aliasing near the edges of the images, while increasing the zero-padding in the angular (u, v) direction reduces the ringing artifacts near the imaged object.

The impact of various zero-padding strategies and different resampling filters is shown in Fig. 3.12. The left column of Fig. 3.12 shows the same slice of the PSF generated via linear interpolation (length 2 triangular resampling filter). The right column of Fig. 3.12 shows the same slice of the PSF generated using a length 2 Kaiser-Bessel resampling filter

with $\beta = 2.3934$ [40]. The top row of Fig. 3.12 is obtained by first zero-padding the radiance array by approximately 5% in each direction (16 zeros in x, 10 zeros in y, 2 zeros in u and v), and the bottom row is obtained by zero-padding the radiance array with 20 zeros in all four dimensions.

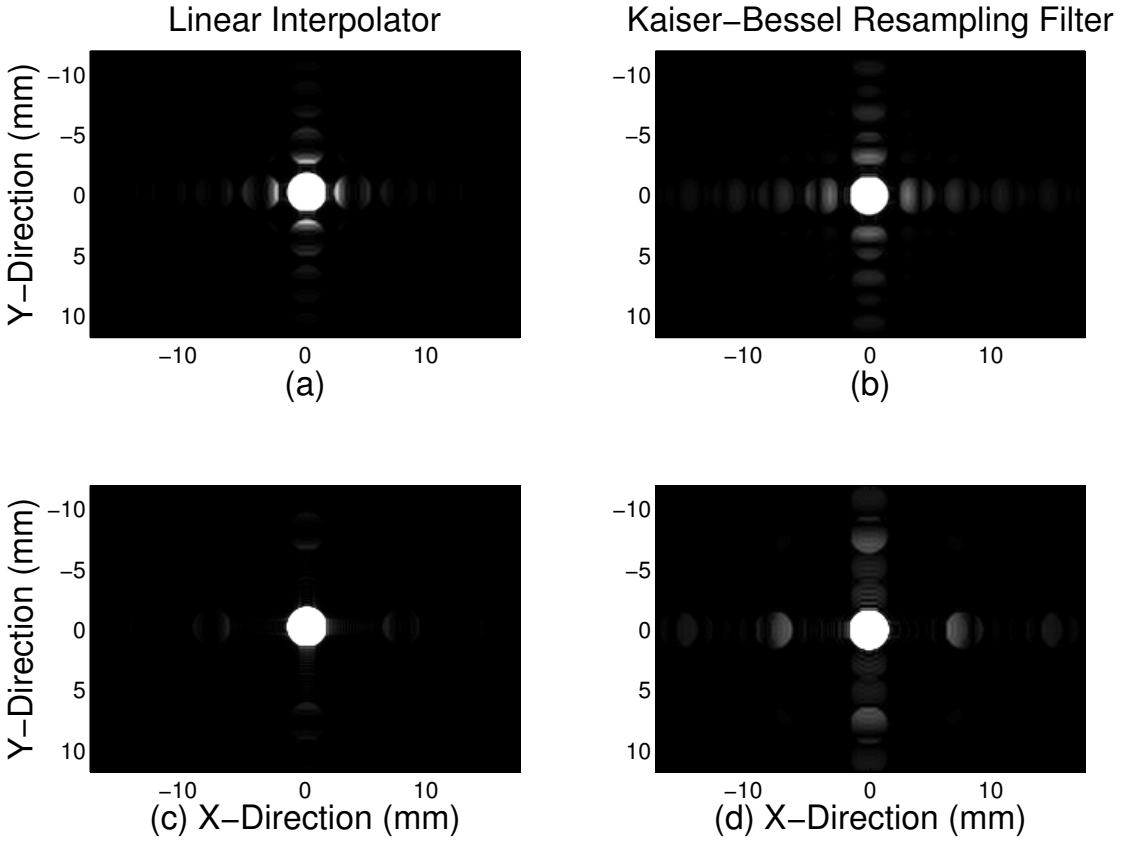

Figure 3.12: Slice of system PSF at 11.8 cm in front of the camera focal plane. Figures (a) and (b) based on approximately 5% zero-padding of radiance array and Figures (c) and (d) based on zero-padding by 20 in all four dimensions. Figures (a) and (c) generated using linear interpolation (length 2 triangular resampling window) and Figures (b) and (d) generated using a length 2 Kaiser-Bessel window with $\beta = 2.3934$. All figures intensity-scaled for clarity.

When zero-padding is limited to 5% in the (u, v) directions, the Kaiser-Bessel resampling filter achieves greater suppression of the ghosting artifacts as shown in Fig. 3.12 (a) and (b). That is, the peak amplitude of the artifacts is smaller than those achieved using the linear resampling filter, but the artifacts decay slower than those of the linear filter. However, padding by 20 zeros in both angular dimensions (125%) significantly improves the artifact

suppression when using a linear resampling window as shown in Fig. 3.12 (c). Zero-padding by 20 zeros in the angular dimensions is a large percentage but is a small absolute number of zeros with minimal impact to the overall processing time. This method of combining zero-padding and linear interpolation reduces the artifacts to near zero.

When speed of image reconstruction is imperative, the Kaiser-Bessel resampling filter may provide a suitable compromise between artifact suppression and computational efficiency. The Kaiser-Bessel window length can be reduced to 1.5 while still providing artifact suppression. The advantage here is that a shorter window length requires fewer terms in the computation of each point in the resampling filter, which improves the speed of the algorithm. However, calculating the weighting terms for the Kaiser-Bessel filter is more computationally intensive than calculating the weighting terms of a linear filter, and testing on a typical laptop has shown very little speed improvement when utilizing the length 1.5 Kaiser-Bessel resampling filter compared to a length 2 linear interpolator.

Increasing the number of zeros used in the zero-padding of the radiance array does increase the number of operations required to compute the 4D FFT of the radiance array. This is a one-time operation that contributes little overall computation time when a large number of focal planes are desired—as with deconvolution. Furthermore, zero-padding of the radiance array also increases the number of points in the slicing operation but only based on the size of the two spatial dimensions. Fortunately, a modest 5% padding in the spatial dimension and 20 zeros in the angular dimension is adequate to suppress the corresponding artifacts. Characterization of the impacts associated with adjusting the various parameters is the subject of future work.

3.1.2 Volumetric Flame Reconstruction

A final example is presented where a plenoptic camera is used to image a scene as shown in Fig. 3.13. The experimental parameters are the same as those given in Table 3.1. A flame generated by a Bunsen burner is located on the optical centerline and 6.25 cm in front of the

camera focal plane. A target plate is located on the optical centerline and 7.25 cm behind the camera focal plane. The plenoptic camera is then used to capture an image of the scene. The raw data captured by the plenoptic camera is shown in Fig. 3.14. Note that both the flame and the target plate appear blurred in the raw image as neither is on the optical focal plane.

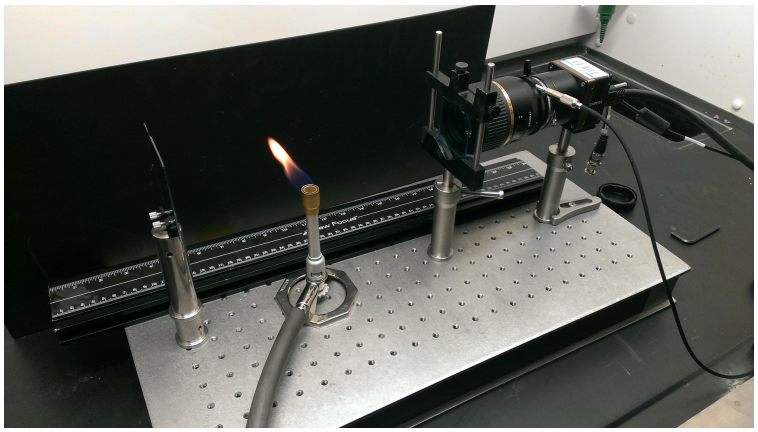

Figure 3.13: Experimental setup showing the plenoptic camera along with the Bunsen burner and target plate being imaged.

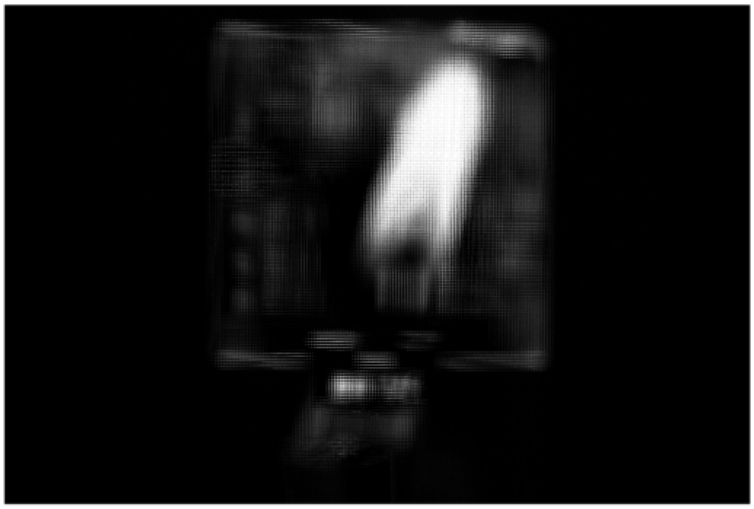

Figure 3.14: Sensor data obtained by imaging the experimental setup. Image intensity-scaled for clarity.

Next, a PSF must be determined. Again, the synthesized PSF presented in Section 2.2.3 is used. The deconvolution begins by creating a focal stack of both the experiment image

and the PSF. Figure 3.15 shows an (x, y) slice of the volume, a single focal plane, at 22.75 cm where the Bunsen burner is in focus. This focal plane shows the image blur resulting from the target plate 13.5 cm further from the camera. In a blur-free image, we would expect to see only the in-focus Bunsen burner. An (x, y) slice of the volume at 36.25 cm is shown in Fig. 3.16 providing an in-focus view of the target plate. Blur from the Bunsen burner flame is significant in the image and obscures a portion of the target plate. In the absence of image blur in the depth direction, the details of the target plate behind the Bunsen burner would be clear.

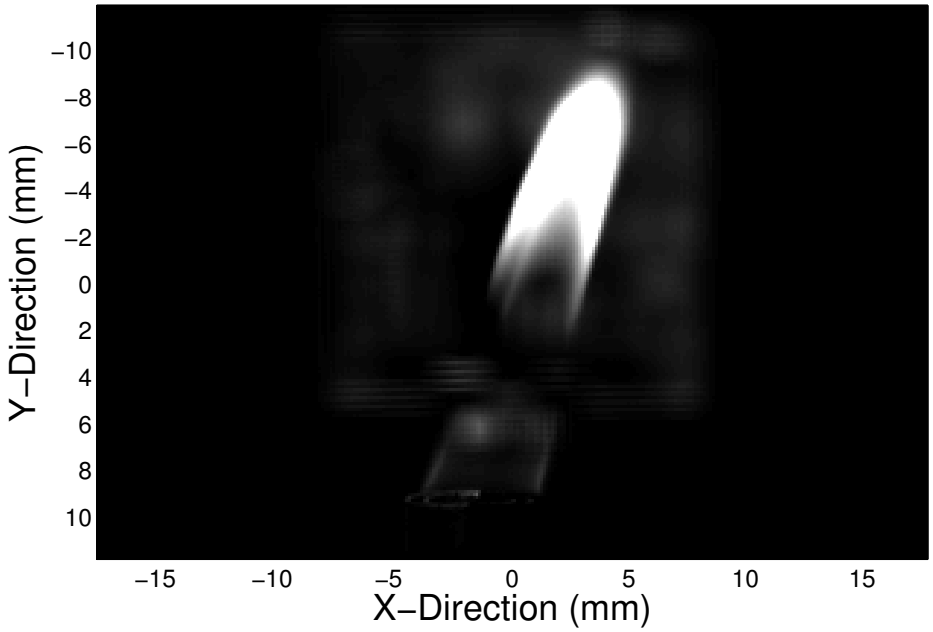

Figure 3.15: Slice of the focal stack along the (x, y) plane at $z = 23$ cm showing the Bunsen burner flame.

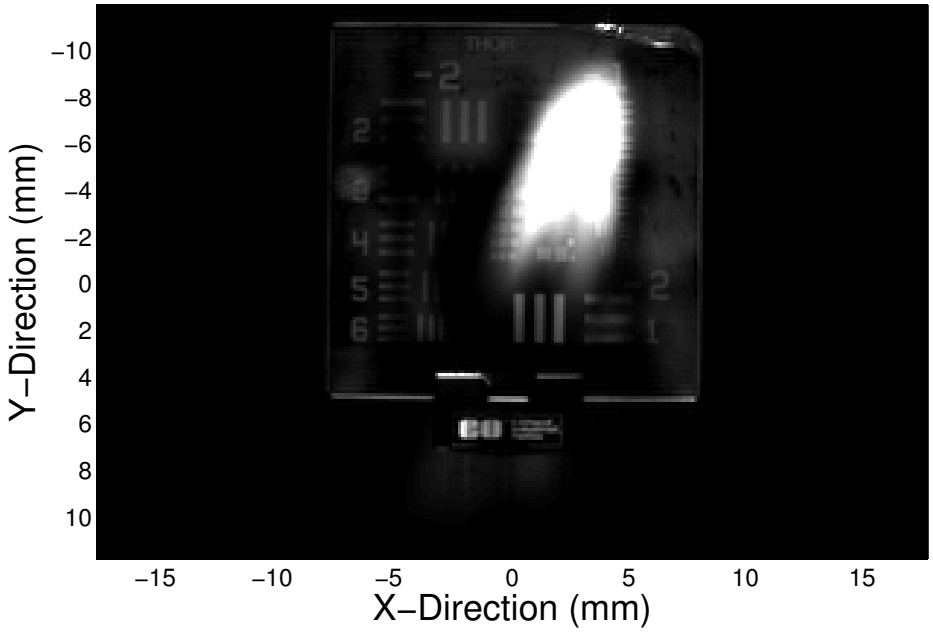

Figure 3.16: Slice of the focal stack along the (x, y) plane at $z = 36$ cm showing the target plate.

Performing the deconvolution and considering the same (x, y) slices as before shows a significant reduction in out-of-plane energy. Of particular note, the blur from the Bunsen burner flame is almost completely eliminated in the (x, y) slice at 36.25 cm shown in Fig. 3.18. Details of the target plate previously obscured can now be seen. This is a significant improvement, as some details of the plate appeared to be lost in the previous image.

The out-of-plane blur is not completely removed in the reconstruction, which arises from the non-invertibility of the PSF as well as the mismatch between the PSF and the object response. This raises the question as to whether integral-based refocusing produces similar results, as the refocusing artifacts are different from those of FFT-based refocusing. Figure 3.19 again shows the deconvolved (x, y) slice of the target plate at 36.25 cm. However, both the focal stack and PSF were generated using integral-based refocusing of the same sensor data. The resulting deconvolved image shows marginally better detail than that shown in Fig. 3.18.

The 3D deconvolution performed here requires less than 10 seconds on a typical laptop without the benefit of parallel processing. Generating the focal stacks using FFT-based

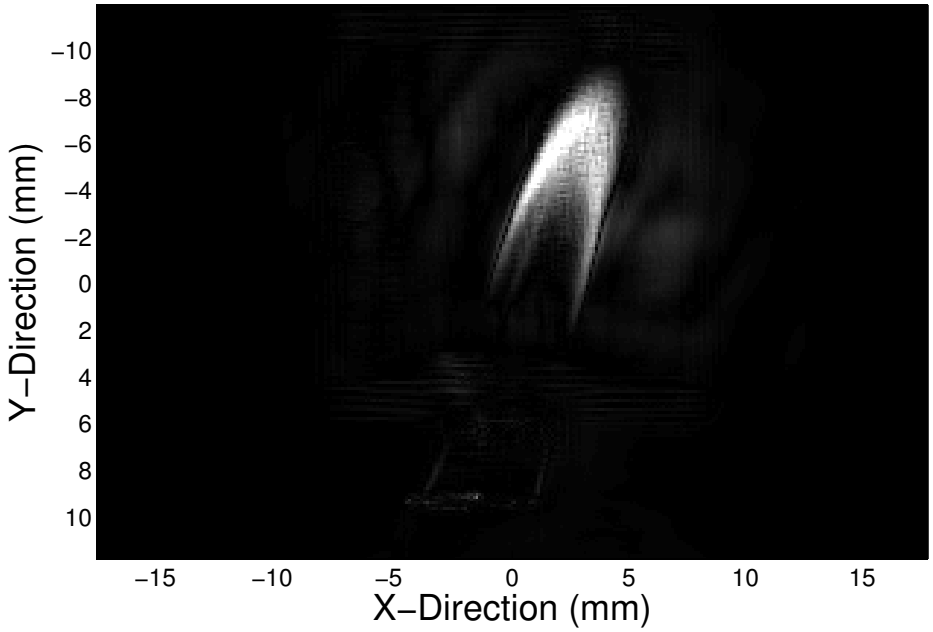

Figure 3.17: Slice of the deconvolved volume along the (x, y) plane at $z = 23$ cm. Image intensity-scaled for better visibility.

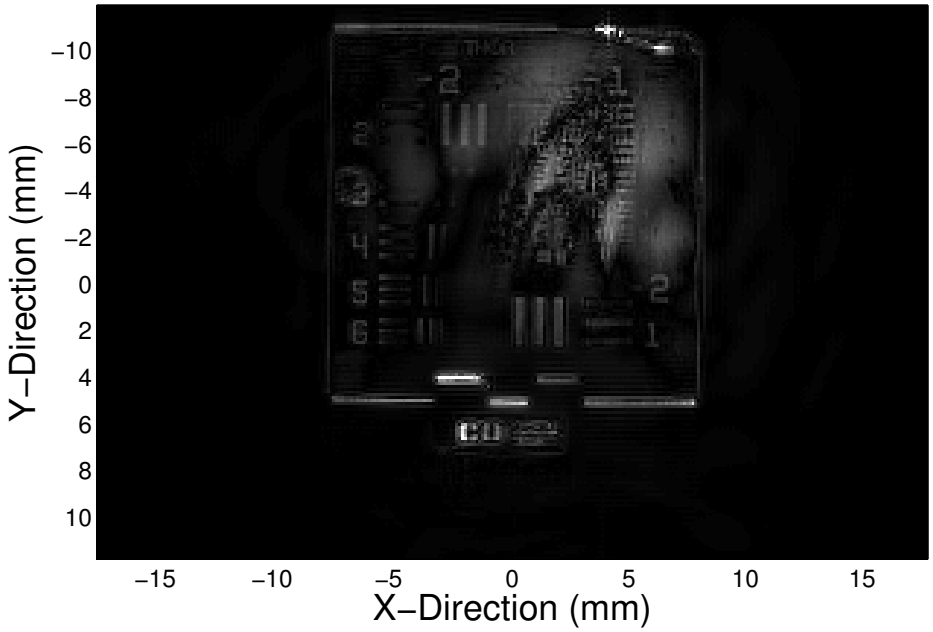

Figure 3.18: Slice of the deconvolved volume along the (x, y) plane at $z = 36.25$ cm. Image intensity-scaled for better visibility.

processing requires less than 30 seconds, while integral-based processing can require orders of magnitude longer. Again, both algorithms would benefit from parallel processing. A comparison of Fig. 3.18 and Fig. 3.19 shows that integral-based processing can yield slightly

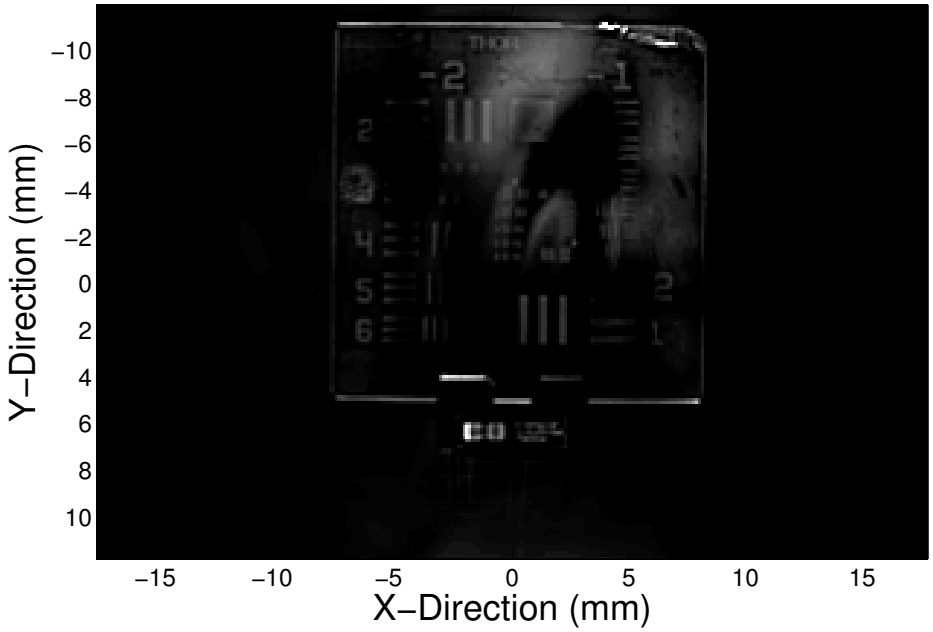

Figure 3.19: Slice of the deconvolved volume along the (x, y) plane at $z = 36.25$mm resulting from integral-based focal stacks. Image intensity-scaled for better visibility.

better results when combined with deconvolution; however, achieving this slight increase in performance requires a significant time penalty when compared to the FFT-based alternative.

Chapter 4

Fourier Projection-Slice Theorem

While deconvolution has been shown to produce excellent results and is computationally efficient, an alternative tomographic reconstruction algorithm is also presented. To achieve this, a specialized form of the Radon transform is derived for the geometry specific to a typical plenoptic camera. This relates the 2-D projections acquired by the plenoptic camera to the 3-D frequency spectrum of the imaged volume. Frequency-domain processing techniques can then be applied to the problem which can capitalize on the efficiency of the FFT in order to significantly reduce the time required to produce an estimate of the imaged volume and eliminate the need for deconvolution—refer to Fig. 4.1.

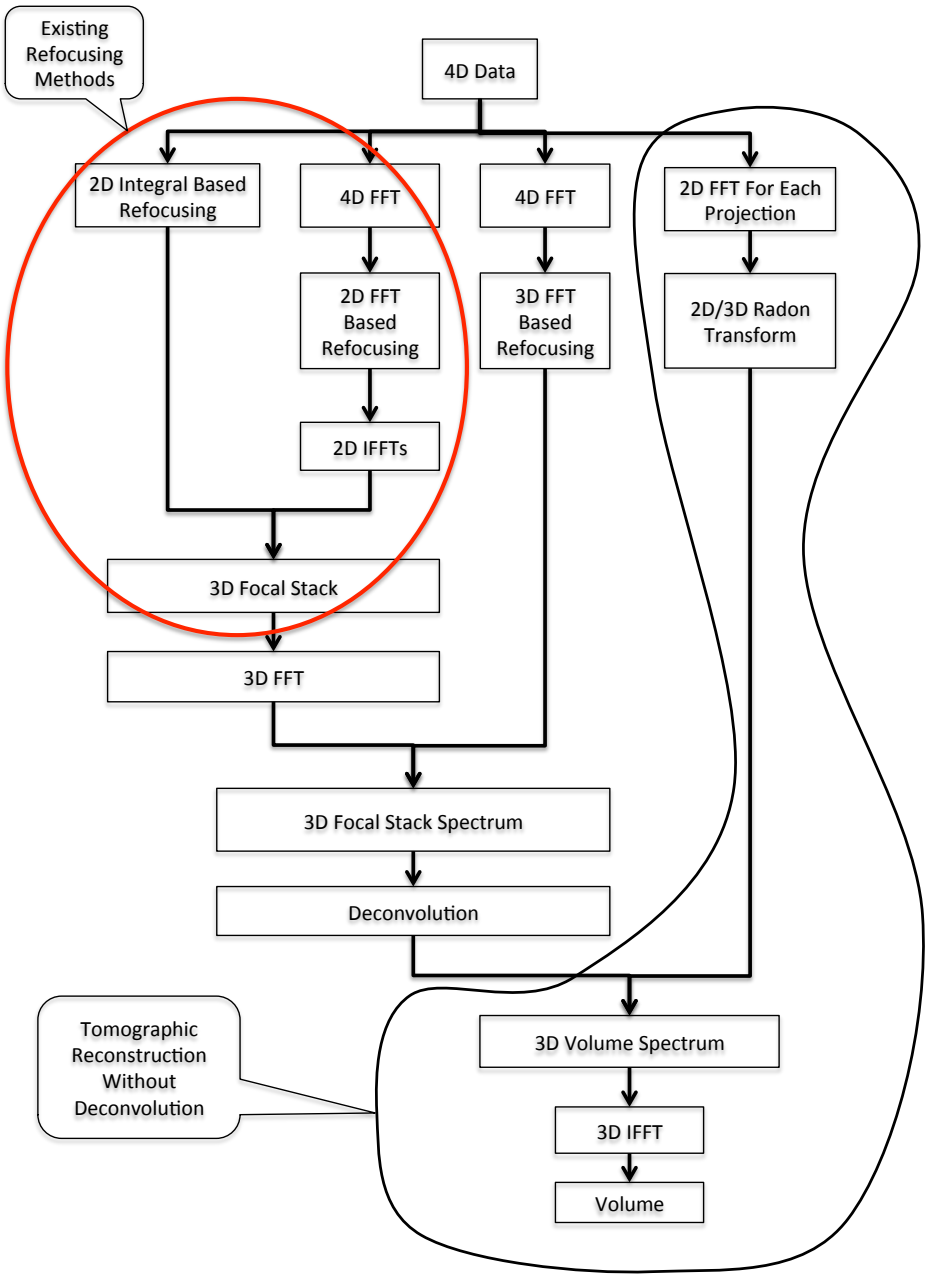

Figure 4.1: Flow chart indicating the use of a specialized form of the Radon transform to obtain the 3D Volume spectrum directly from the 2D projections.

4.1 Fourier Projection-Slice Theorem

Plenoptic imaging can be thought of as taking 2-D projections from a 3-D object over a range of angles. This transformation is an extension of the 2-D Radon transform to 3-D space, i.e., the 3-D Radon transform. In the case of a complete set of angles, it is well known that the 3-D Radon transform has an inverse as does the 2-D transform through the use of the projection-slice theorem.

While the projection-slice theorem has been extended to higher dimensions, plenoptic imaging poses a unique situation in that the imaging sensor is on a fixed plane, and only a limited number of angular samples can be collected. The typical geometry is one where the sensor is rotated around the object to be imaged, allowing each projection to be taken normal to the imaging surface over a full range of angles.

4.1.1 2-D/3-D Extension of the Fourier Projection-Slice Theorem

The projection-slice theorem is the basis for Fourier-based tomographic reconstruction. Traditionally, this is used to reconstruct a 2-D image $f(x, y)$ from its 1-D projections $g(\ell, \theta)$ [41] and is formally given by:

$$G(\varrho, \theta) = F(\varrho \cos\theta, \varrho \sin\theta) \tag{4.1}$$

This relationship states that the Fourier transform of the 1-D projection $g(\ell, \theta)$ is equivalent to a slice from the 2-D Fourier transform of the object $f(x, y)$. The projection-slice theorem has been extended to higher dimensions [42–44], but typically the geometry is such that the line integrals necessary to calculate the projection are taken normal to the surface. However, the sensor in a plenoptic camera is fixed, and the image of the 3-D object is projected onto this sensor. That is, the line integrals used to calculate the projection will

intersect the sensor plane at some arbitrary angles θ and ϕ. The projection-slice theorem must be established for this new geometry.

Defining an arbitrary object in a 3-dimensional space by $f(x, y, z)$, the projection $g(x', y', \bar{v})$ resulting from rays parallel to $\hat{v}$ onto a 2-dimensional plane at $z = 0$ is given by:

$$g(x', y', \bar{v}) = \int_{-\infty}^{\infty} \int_{-\infty}^{\infty} \int_{-\infty}^{\infty} f(x, y, z) \delta(\bar{r} - \bar{r_0} - t\bar{v})\, dx\, dy\, dz.$$

Here, $\bar{r} = \bar{r_0} + t\bar{v}$ is the equation of a vector in three-space as shown in Figure 4.2. This is obtained by recognizing that the vector $\bar{v}$ is a unit vector in the direction of $\bar{a}$, and it can be shown that a number t exists such that $t\bar{v} = \bar{a}$. As a result,

$$\bar{a} = \bar{r} - \bar{r_0}$$

$$t\bar{v} = \bar{r} - \bar{r_0}$$

$$\bar{r} = \bar{r_0} + t\bar{v}$$

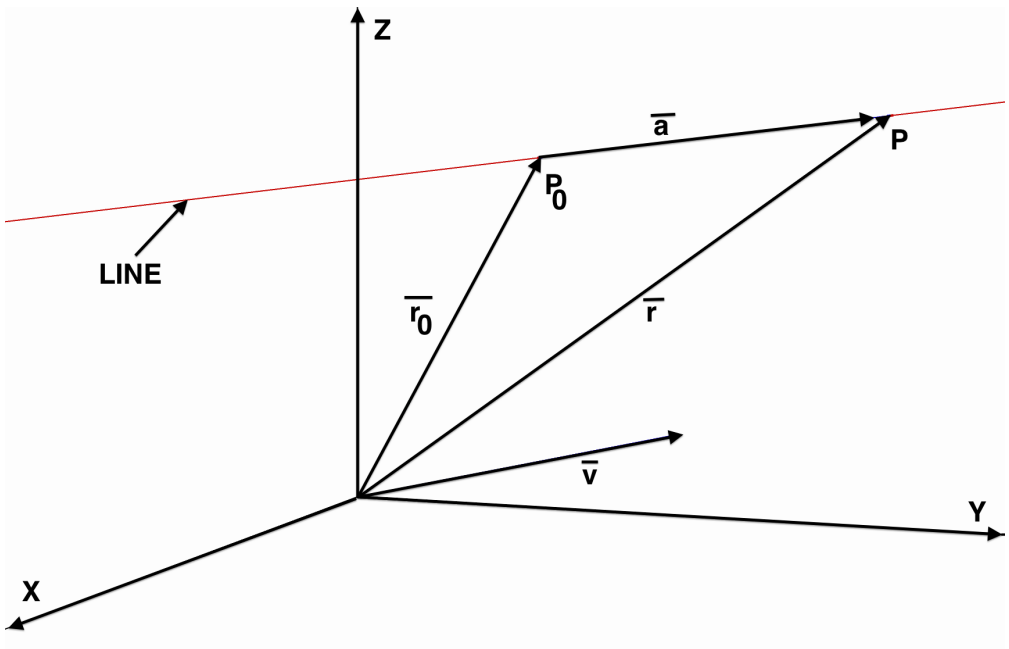

Figure 4.2: Geometry for the equation of a line in three-space

The unit vector $\bar{v}$ can be written in polar coordinates as

$$\bar{v} = \begin{pmatrix} \sin\theta\cos\phi \\ \sin\theta\sin\phi \\ \cos\theta \end{pmatrix}$$

and the equation of a line parallel to the unit vector in three-space is given by

$$\bar{r} = \bar{r_0} + t\bar{v}$$

$$\begin{pmatrix} x \\ y \\ z \end{pmatrix} = \begin{pmatrix} x' \\ y' \\ z' \end{pmatrix} + t \begin{pmatrix} \sin\theta\cos\phi \\ \sin\theta\sin\phi \\ \cos\theta \end{pmatrix}$$

where the coordinates for vectors $\bar{r}$ and $\bar{r_o}$ are explicitly shown.

However, by centering the coordinate system on the $z' = 0$ plane, t can now be solved for in terms of z.

$$\begin{pmatrix} x \\ y \\ z \end{pmatrix} = \begin{pmatrix} x' \\ y' \\ 0 \end{pmatrix} + t \begin{pmatrix} \sin\theta\cos\phi \\ \sin\theta\sin\phi \\ \cos\theta \end{pmatrix}$$

$$t = \frac{z}{\cos\theta}$$

$$\begin{pmatrix} x \\ y \end{pmatrix} = \begin{pmatrix} x' \\ y' \end{pmatrix} + z \begin{pmatrix} \tan\theta\cos\phi \\ \tan\theta\sin\phi \end{pmatrix}$$

The geometry of the system is shown in Figure 4.3. Taking the 2-D Fourier transform of $g\left(x', y', \bar{v}\right)$

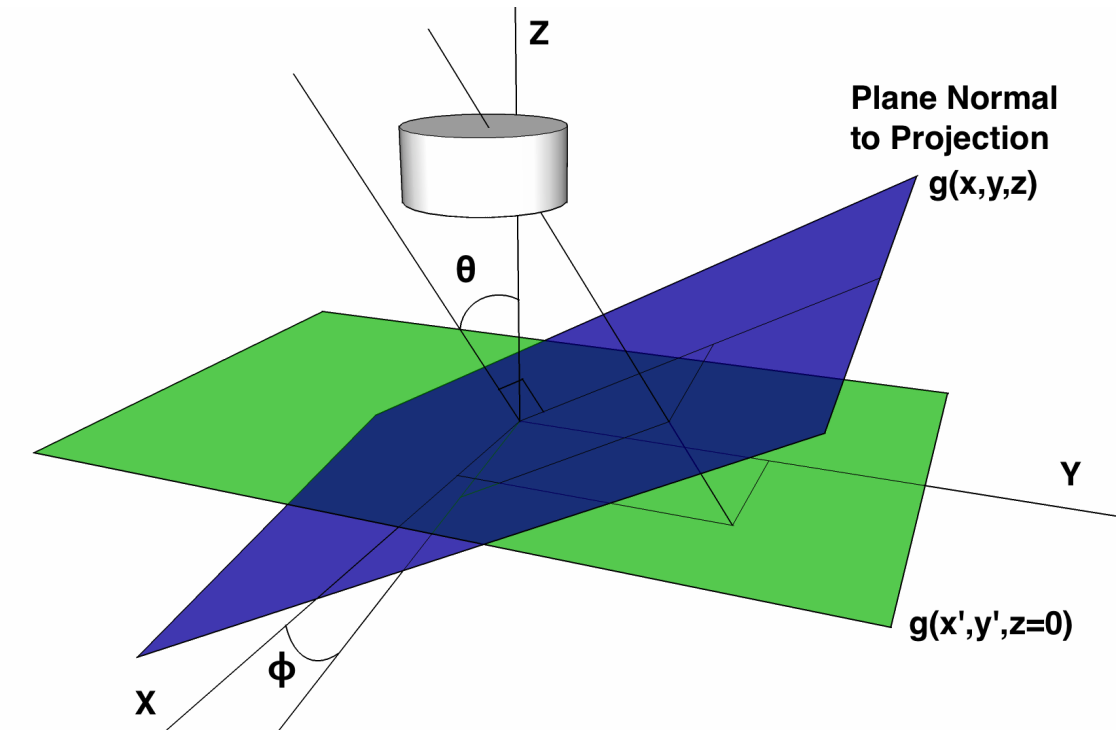

Figure 4.3: Geometry of projections through the volume (x, y, z) onto the sensor plane

$$
\begin{aligned}
G(k_x, k_y, \hat{v}) &= \int_{-\infty}^{\infty}\int_{-\infty}^{\infty} g(x', y', \hat{v}) e^{-\jmath 2\pi(k_x x' + k_y y')}\, dx'\, dy' \\
&= \int_{-\infty}^{\infty}\int_{-\infty}^{\infty}\int_{-\infty}^{\infty}\int_{-\infty}^{\infty}\int_{-\infty}^{\infty} f(x, y, z) \\
&\delta(r - r_0 - t\hat{v}) e^{-\jmath 2\pi(k_x x' + k_y y')}\, dx\, dy\, dz\, dx'\, dy' \\
&= \int_{-\infty}^{\infty}\int_{-\infty}^{\infty}\int_{-\infty}^{\infty}\int_{-\infty}^{\infty}\int_{-\infty}^{\infty} f(x, y, z) \\
&\delta(x - x' - z\tan(\theta)\cos(\phi), \\
&y - y' - z\tan(\theta)\sin(\phi)) \\
&e^{-\jmath 2\pi(k_x x' + k_y y')}\, dx\, dy\, dz\, dx'\, dy' \\
&= \int_{-\infty}^{\infty}\int_{-\infty}^{\infty}\int_{-\infty}^{\infty} f(x, y, z) \\
&e^{-\jmath 2\pi(k_x x + k_y y - z\tan(\theta)(k_x\cos(\phi) + k_y\sin(\theta)))} \\
&dx\, dy\, dz
\end{aligned}
$$

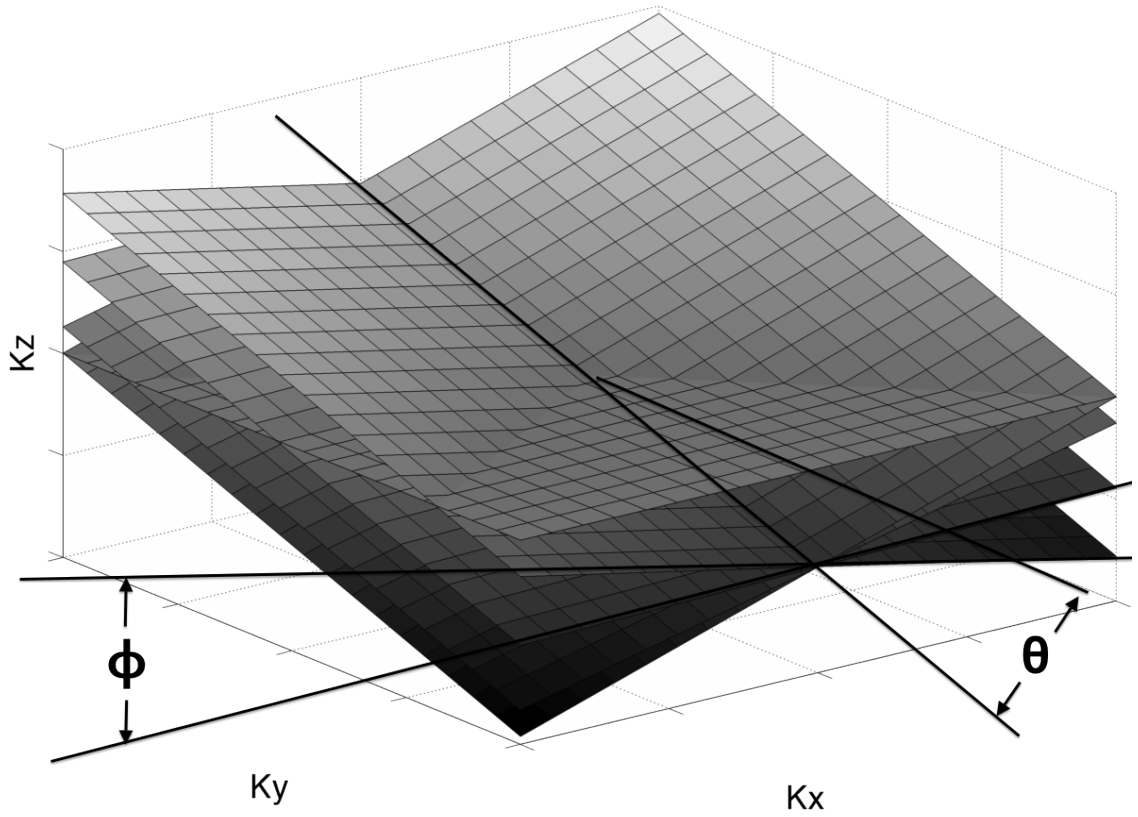

Figure 4.4: Geometry of projections through the volume (x, y, z) onto the sensor plane

where the last line follows by applying the sifting property of the Dirac delta function and by regrouping terms.

This is the Fourier projection-slice theorem relating the 2-D projections from an object to its 3-D Fourier transform for the geometry shown in Figure 4.3. This relationship indicates that the Fourier transform of a 2-D projection at a given (θ, ϕ) will populate a slice of the 3-D image frequency spectrum as shown in Figure 4.4. This allows the imaged volume to be reconstructed directly from the plenoptic data. Furthermore, because this relationship is based on the frequency-domain representations of the signals, efficient FFT processing can be used to move between the spatial domain and the frequency domain.

Figure 4.4 also serves to demonstrate a primary limitation in limited angle tomographic reconstruction algorithms. The slices used to populate the object spectrum pivot about the origin. The resulting sample spacing is denser near the origin. Also, the points in each slice

do not fall on a uniform grid within the object spectrum, and values must be assigned either through nearest neighbor or by interpolation as the FFT requires uniform sample spacing.

This represents a fundamentally different approach to reconstruction of the volume when compared to deconvolution. Deconvolution uses slices from the 4D FFT of the radiance array to populate the 3D spectrum of the focal stack. This spectrum is then deconvolved with the spectrum of the PSF in order to reconstruct the volume. The tomographic approach presented here utilized 2D FFTs associated with each perspective view to directly populate the 3D spectrum of the volume.

4.2 Simulated FFT-based Tomographic Reconstruction

To demonstrate the efficacy of this approach, a 2-D plenoptic imaging system is simulated with the parameters identified in Table 4.1 and a native focal plane at $(x, 100\text{mm})$. A particle field containing a particle at $(1.9\text{mm}, 115\text{mm})$ and another at $(-1.9\text{mm}, 85\text{mm})$ is simulated and the resulting camera sensor data and focal stack are each generated via ray tracing algorithms. The focal stack is generated for comparison using an integral based refocusing algorithm. The scene is then estimated using the FFT-based tomographic approach presented here, and the results of the two reconstruction techniques are shown in Figure 4.5.

Table 4.1: 2-D Simulation Parameters

Lenslet Focal Length	f_l	0.500mm
Lenslet Pitch	p_l	0.125mm
Pixel Pitch	p_p	0.0074mm
Number of Pixels	n_p	1503
Sensor Size		10.5mm
Number of Lenslets	n_l	89
Main Lens Focal Length	f_m	50mm

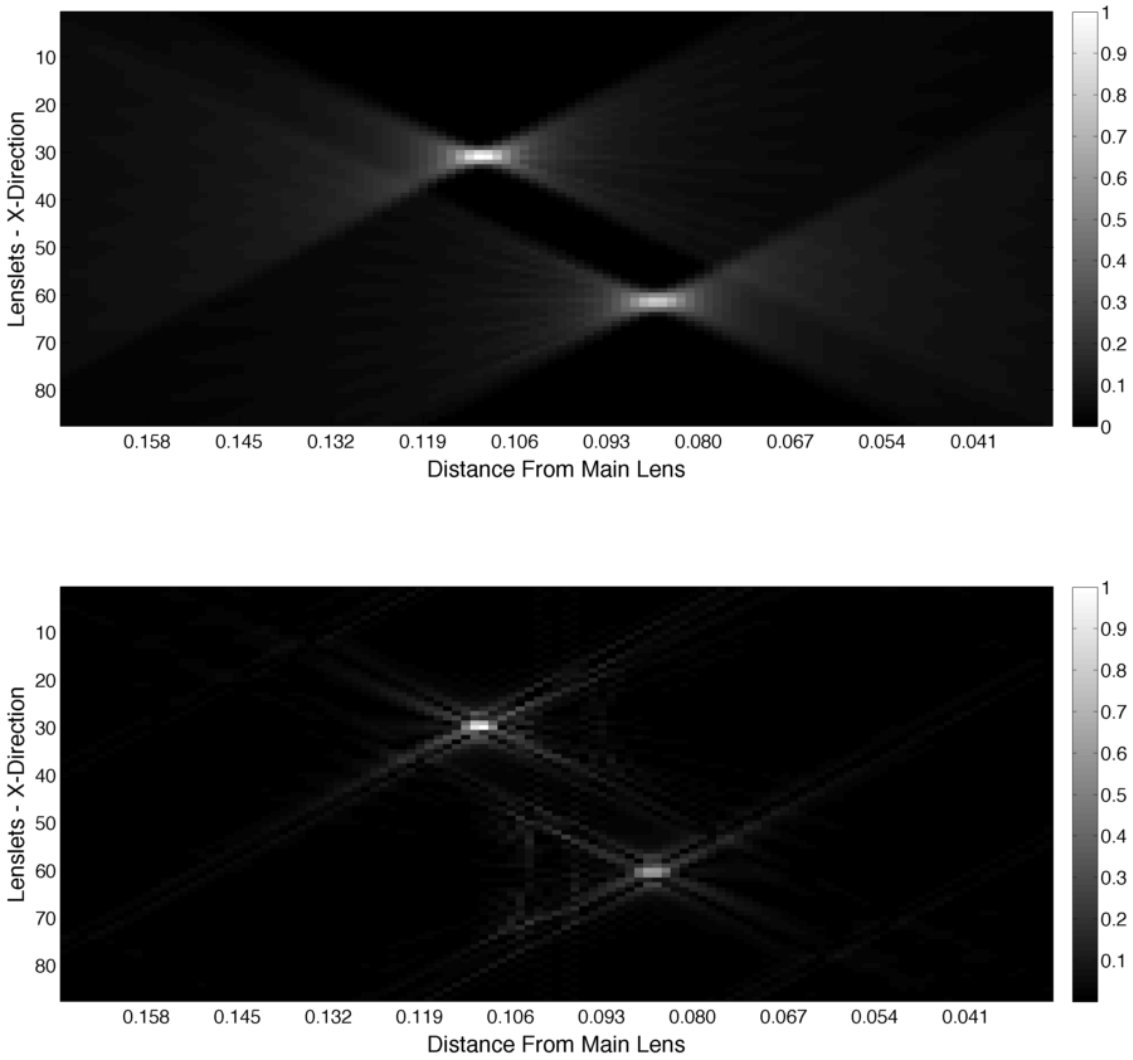

Figure 4.5: Comparison of 2D simulations showing the focal stack (top) and the reconstructed volume (bottom)

It is obvious that the tomographic reconstruction yields significantly reduced out-of-plane energy when compared to the object focal stack. Because the algorithm relies on FFT-based processing, the reconstruction can be completed in seconds on even a modestly equipped personal laptop. By comparison, FFT-based deconvolution on the same machine requires approximately twice as long. This is in part due to the fact that a focal stack for both the imaged volume and a PSF must be generated and processed. The practical limit for the reconstruction size is set by the system memory.

Unfortunately, artifacts do remain. Ideally, the reconstruction would return a single impulse for each of the particles simulated. However, because the plenoptic camera captures a limited range of angles, the frequency spectrum for the imaged space is not fully populated. Furthermore, the frequency spectrum near the origin is more densely populated than regions near the perimeter of the spectrum. These factors yield artifacts in the estimates and serve to limit the resolution in the final reconstruction.

4.3 3D Reconstruction From Experimental Data

While 2D simulations provide insight into the characteristics of the algorithm, reconstruction of 3D volumes is the ultimate goal. To demonstrate the algorithm in 3D, the experimental data from Fig. 2.13 is again used. Once again, this configuration places the optical focal plane at approximately 40.25 cm in front of the camera CCD, or 29 cm in front of the camera aperture. The flame generated by the Bunsen burner is located on the optical centerline and 6.25 cm in front of the camera focal plane. The target plate is located on the optical centerline and 7.25 cm behind the camera focal plane.

The plenoptic data is first used to synthesize an image focused on the Bunsen burner flame and the target plate, Fig. 4.6 and Fig. 4.7 respectively. An estimate of the volume is generated via FFT-based projection-slice reconstruction. The slice of the volume corresponding to the Bunsen burner position is shown in Fig. 4.8 followed by the slice of the volume corresponding to the plate position in Fig. 4.9. Both figures show a reduced blur when compared to the corresponding slices of focal stack.

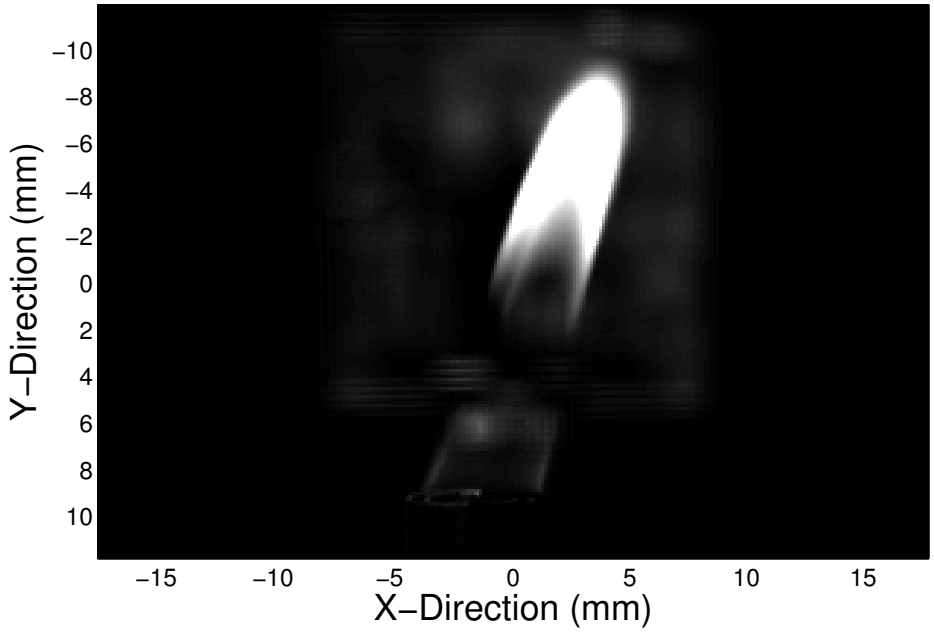

Figure 4.6: Slice of the focal stack along the (x, y) plane at $z = 23$ cm showing the Bunsen burner flame.

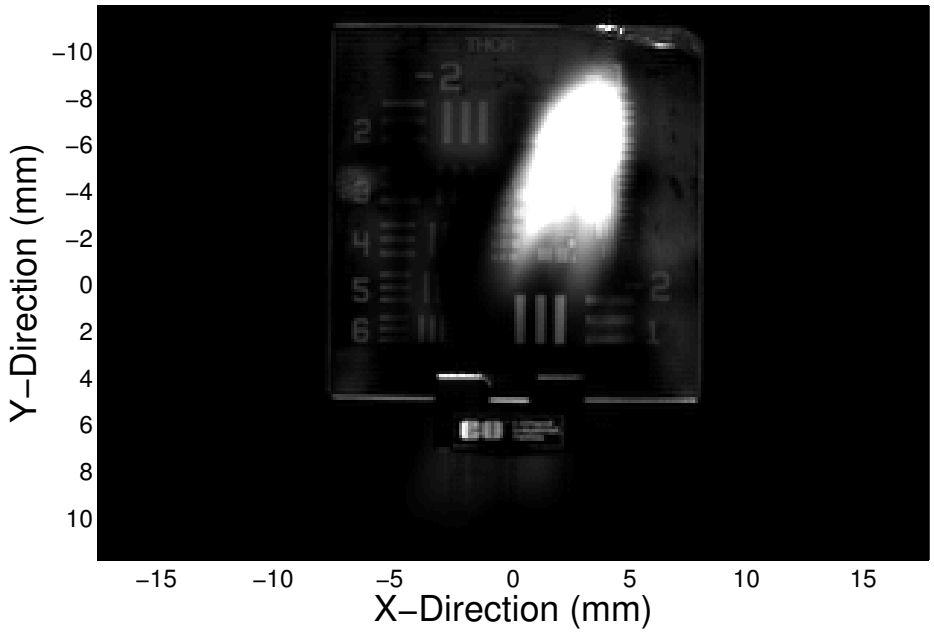

Figure 4.7: Slice of the focal stack along the (x, y) plane at $z = 36$ cm showing the target plate.

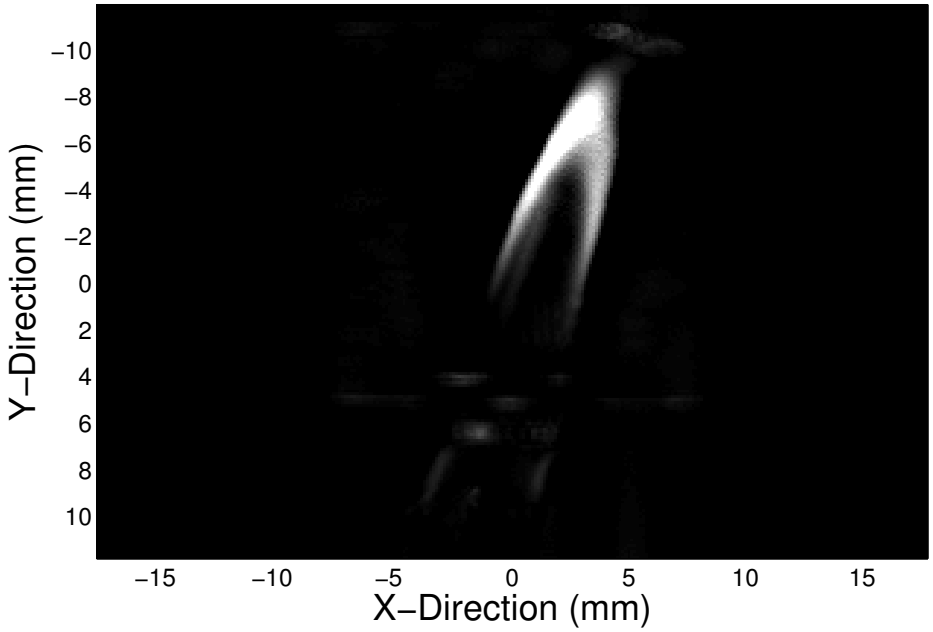

Figure 4.8: Slice of the reconstructed volume along the (x, y) plane at $z = 23$ cm. Image intensity-scaled for better visibility.

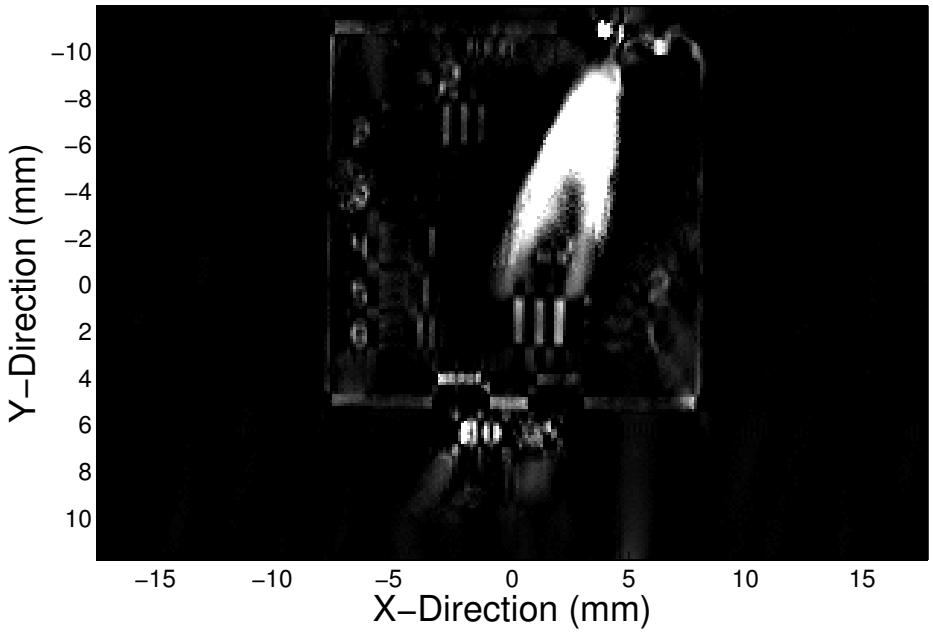

Figure 4.9: Slice of the reconstructed volume along the (x, y) plane at $z = 36.25$ cm. Image intensity-scaled for better visibility.

Unfortunately, this algorithm does not completely remove the image blur. Both FFT-based deconvolution and MART have been shown to produce reconstructions with blur significantly reduced compared to these results. However, both MART and FFT-based deconvolution are significantly slower than this method. MART can require several orders of magnitude longer to produce a similarly sized reconstruction. Deconvolution is much faster than MART, but must compute a radiance array—and the corresponding 4D FFT—of both the focal stack and a PSF. As a result of this additional computational overhead, deconvolution is roughly half as fast as FFT-based projection-slice processing. Furthermore, when utilizing deconvolution, the user is faced with estimating the PSF of the system, which can have a significant impact on the quality of the results.

Chapter 5

Conclusions

This research demonstrates two novel approaches to reconstructing a volume imaged utilizing a plenoptic camera. Firstly, deconvolution is presented which utilizes knowledge of the system impulse response to reduce the blur inherent in the object focal stack, thereby improving the estimate of the volume. Secondly, a 2-D/3-D extension of the projection-slice theorem has been developed for computing volumetric estimates directly from the recorded projections.

Deconvolution has been shown to be a highly efficient means of volume reconstruction from plenoptic data. Given the PSF and focal stack, the volume can be reconstructed in seconds. When compared to existing tomographic methods such as MART that may require several hours to reconstruct modestly sized volumes [45–47], this is a significant improvement.

However, limitations remain. In order to use deconvolution, the focal stacks for both the PSF and the object space must be available. Synthesizing these using integral-based algorithms is computationally intensive and can require hours to calculate. Fortunately, FFT-based refocusing algorithms can also be used for focal stack synthesis and can reduce the computation time to seconds. Both integral-based and FFT-based image synthesis exhibit technique-specific artifacts not previously identified in the current literature.

Integral-based image synthesis demonstrates a banding phenomenon in the focal stacks. This is the direct result of inadequate sampling of the plenoptic data when calculating the refocused image. While this can be reduced significantly by increasing the number of angular samples used in the calculation, this directly affects the computational overhead of an already computationally intensive process. Furthermore, the refocusing process results in asymmetry of the PSF due to the structure of the data.

While FFT-based image synthesis yields a significantly reduced computational burden, it too displays technique-specific artifacts. The banding present in integral-based image synthesis is not present when utilizing FFT-based processing due to the low-pass filtering inherent with the technique. While this yields a smoother response, this filtering effect also results in an asymmetric response and reduced resolution. Previous publications have presented resampling algorithms designed to reduce the ringing artifacts associated with the spectral banding inherent with FFT-based processing. However, with proper preprocessing of the data, superior results can be achieved with a more efficient linear resampling filter. While both algorithms have been demonstrated to recover information otherwise obscured by out-of-plane energy, the application of FFT-based processing results in an algorithm many times faster than an equivalent integral-based algorithm.

These artifacts directly affect the quality of the reconstructions obtained via deconvolution due to mismatch between the PSF and the object response. While the plenoptic imaging system impulse response can be modeled as shift-invariant, sampling and quantization effects result in a highly variable object response. As a result, a single PSF cannot provide a perfect reconstruction of the volume. Future work will explore the possibility of filtering the acquired data and/or the reconstructed response, as well as the development of iterative algorithms that can be used either exclusively or in conjunction with deconvolution to provide improved reconstructions. However, despite the residual blur, such a reconstruction is a significant improvement over the initial focal stack. We have demonstrated the value of the technique for a single application—reconstructing combustion events that could be used to improve burner design. This application illustrates the potential of plenoptic imaging for volume reconstruction in many other applications as well.

Finally, FFT-based tomographic reconstruction algorithms can provide a computationally efficient method of estimating volumes imaged by a plenoptic camera. The accuracy of the resulting estimates is limited by the angular range of projections acquired by the camera. Nevertheless, the speed with which an estimate can be generated makes this approach

appealing for applications where multiple volumetric estimates are required, such as combustion and/or flame imaging. Future work will attempt to quantify the resolution limits and tradeoffs inherent in tomographic reconstruction specifically applied to plenoptic imaging.

Bibliography

[1] R. Ng, "Fourier Slice Photography," in *ACM SIGGRAPH 2005 Papers*, ser. SIGGRAPH '05. New York, NY, USA: ACM, 2005, pp. 735–744. [Online]. Available: http://doi.acm.org/10.1145/1186822.1073256

[2] ——, "Digital Light Field Photography," Ph.D. dissertation, Stanford University, July 2006.

[3] B. Wilburn, N. Joshi, V. Vaish, E.-V. Talvala, E. Antunez, A. Barth, A. Adams, M. Horowitz, and M. Levoy, "High Performance Imaging Using Large Camera Arrays," *ACM Trans. Graph.*, vol. 24, no. 3, pp. 765–776, Jul. 2005. [Online]. Available: http://doi.acm.org/10.1145/1073204.1073259

[4] T. G. Georgiev and A. Lumsdaine, "Resolution in Plenoptic Cameras," in *Frontiers in Optics 2009/Laser Science XXV/Fall 2009 OSA Optics & Photonics Technical Digest*. Optical Society of America, 2009, p. CTuB3. [Online]. Available: http://www.opticsinfobase.org/abstract.cfm?URI=COSI-2009-CTuB3

[5] F. Scarano, "Iterative Image Deformation Methods in PIV," *Measurement Science and Technology*, vol. 13, no. 1, p. R1, 2002. [Online]. Available: http://stacks.iop.org/0957-0233/13/i=1/a=201

[6] F. Scarano and M. L. Riethmuller, "Advances in Iterative Multigrid PIV Image Processing," *Experiments in Fluids*, vol. 29, no. 1, pp. S051–S060, 2000. [Online]. Available: http://dx.doi.org/10.1007/s003480070007

[7] J. Westerweel, G. E. Elsinga, and R. J. Adrian, "Particle Image Velocimetry for Complex and Turbulent Flows," *Annual Review of Fluid Mechanics*, vol. 45, no. 1, pp. 409–436, 2013. [Online]. Available: http://dx.doi.org/10.1146/annurev-fluid-120710-101204

[8] M. Raffel, C. E. Willert, S. T. Wereley, and J. Kompenhans, *Particle Image Velocimetry: A Practical Guide (Experimental Fluid Mechanics)*, 2nd ed. Springer, 8 2007. [Online]. Available: http://www.springer.com/us/book/9783540723073

[9] R. J. Adrian and J. Westerweel, *Particle Image Velocimetry (Cambridge Aerospace Series)*. Cambridge University Press, 12 2010. [Online]. Available: http://www.cambridge.org/us/academic/subjects/engineering/thermal-fluids-engineering/particle-image-velocimetry?format=HB

[10] C. Brucker, D. Hess, and J. Kitzhofer, "Single-View Volumetric PIV via High-Resolution Scanning, Isotropic Voxel Restructuring and 3D Least-Squares Matching (3D-LSM)," *Measurement Science and Technology*, vol. 24, no. 2, p. 024001, 2013. [Online]. Available: http://stacks.iop.org/0957-0233/24/i=2/a=024001

[11] T. Hori and J. Sakakibara, "High-speed Scanning Stereoscopic PIV for 3D Vorticity Measurement in Liquids," *Measurement Science and Technology*, vol. 15, no. 6, p. 1067, 2004. [Online]. Available: http://stacks.iop.org/0957-0233/15/i=6/a=005

[12] F. Pereira, M. Gharib, D. Dabiri, and D. Modarress, "Defocusing Digital Particle Image Velocimetry: A 3-Component 3-Dimensional DPIV Measurement Technique. Application to Bubbly Flows," *Experiments in Fluids*, vol. 29, no. 1, pp. S078–S084, 2000. [Online]. Available: http://dx.doi.org/10.1007/s003480070010

[13] A. Schrder and C. E. Willert, Eds., *Particle Image Velocimetry: New Developments and Recent Applications (Topics in Applied Physics)*, 2008th ed. Springer, 3 2008. [Online]. Available: http://www.springer.com/us/book/9783540735274

[14] K. D. Hinsch, "Holographic Particle Image Velocimetry," *Measurement Science and Technology*, vol. 13, no. 7, p. R61, 2002. [Online]. Available: http://stacks.iop.org/0957-0233/13/i=7/a=201

[15] T. Fahringer and B. Thurow, "Tomographic Reconstruction of a 3-D Flow Field Using a Plenoptic Camera," in *Fluid Dynamics and Co-located Conferences*. American Institute of Aeronautics and Astronautics, Jun. 2012, pp. –. [Online]. Available: http://dx.doi.org/10.2514/6.2012-2826

[16] T. W. Fahringer and B. S. Thurow, "3D Particle Position Reconstruction Accuracy in Plenoptic PIV," in *AIAA SciTech*. American Institute of Aeronautics and Astronautics, Jan. 2014, pp. –. [Online]. Available: http://dx.doi.org/10.2514/6.2014-0398

[17] K. Lynch and B. Thurow, "3-D Flow Visualization of Axisymmetric Jets at Reynolds Number 6,700 and 10,200," *Journal of Visualization*, vol. 15, no. 4, pp. 309–319, 2012. [Online]. Available: http://dx.doi.org/10.1007/s12650-012-0141-2

[18] G. E. Elsinga, B. Wieneke, F. Scarano, and A. Schroder, "Tomographic 3D-PIV and Applications," in *Particle Image Velocimetry*. Springer Berlin Heidelberg, 2008, vol. 112, pp. 103–125.

[19] B. Bohm, C. Heeger, R. Gordon, and A. Dreizler, "New Perspectives on Turbulent Combustion: Multi-Parameter High-Speed Planar Laser Diagnostics," *Flow, Turbulence and Combustion*, vol. 86, no. 3-4, pp. 313–341, 2011.

[20] G. Kychakoff, K. Knapp, R. D. Howe, and R. K. Hanson, "Flow Visualization in Combustion Gases Using Nitric Oxide Fluorescence," *AIAA Journal*, vol. 22, no. 1, pp. 153–154, Jan. 1984. [Online]. Available: http://dx.doi.org/10.2514/3.8359

[21] K. Watson, K. Lyons, J. Donbar, and C. Carter, "Scalar and Velocity Field Measurements in a Lifted CH4-Air Diffusion Flame," *Combustion and Flame*, vol. 117, no. 1-2, pp. 257 – 271, 1999.

[22] P. Kothnur, M. Tsurikov, N. Clemens, J. Donbar, and C. Carter, "Planar Imaging of CH, OH, and Velocity in Turbulent Non-premixed Jet Flames," *Proceedings of the Combustion Institute*, vol. 29, no. 2, pp. 1921 – 1927, 2002. [Online]. Available: http://www.sciencedirect.com/science/article/pii/S1540748902802334

[23] R. K. Hanson, "Applications of Quantitative Laser Sensors to Kinetics, Propulsion and Practical Energy Systems," *Proceedings of the Combustion Institute*, vol. 33, no. 1, pp. 1 – 40, 2011. [Online]. Available: http://www.sciencedirect.com/science/article/pii/S1540748910003913

[24] L. Ma, W. Cai, A. W. Caswell, T. Kraetschmer, S. T. Sanders, S. Roy, and J. R. Gord, "Tomographic Imaging of Temperature and Chemical Species Based on Hyperspectral Absorption Spectroscopy," *Opt. Express*, vol. 17, no. 10, pp. 8602–8613, May 2009. [Online]. Available: http://www.opticsexpress.org/abstract.cfm?URI=oe-17-10-8602

[25] K. Y. Cho, A. Satija, T. L. Pourpoint, S. F. Son, and R. P. Lucht, "High-repetition-rate Three-dimensional OH Imaging Using Scanned Planar Laser-induced Fluorescence System for Multiphase Combustion," *Appl. Opt.*, vol. 53, no. 3, pp. 316–326, Jan 2014. [Online]. Available: http://ao.osa.org/abstract.cfm?URI=ao-53-3-316

[26] J. Hult, A. Omrane, J. Nygren, C. Kaminski, B. Axelsson, R. Collin, P.-E. Bengtsson, and M. Alden, "Quantitative Three-dimensional Imaging of Soot Volume Fraction in Turbulent Non-premixed Flames," *Experiments in Fluids*, vol. 33, no. 2, pp. 265–269, 2002. [Online]. Available: http://dx.doi.org/10.1007/s00348-002-0410-2

[27] W. Fischer and H. Burkhardt, "Three-dimensional Temperature Measurement in Flames by Multispectral Tomographic Image Analysis," *Proc. SPIE*, vol. 1349, pp. 96–105, 1990. [Online]. Available: http://dx.doi.org/10.1117/12.23521

[28] M. Hossain, G. Lu, and Y. Yan, "Three-dimensional Reconstruction of Combustion Flames Through Optical Fiber Sensing and CCD Imaging," in *Instrumentation and Measurement Technology Conference (I2MTC), 2011 IEEE*, May 2011, pp. 1–5.

[29] T. Qiu, Y. Yan, and G. Lu, "A New edge Detection Algorithm for Flame Image Processing," in *Instrumentation and Measurement Technology Conference (I2MTC), 2011 IEEE*, May 2011, pp. 1–4.

[30] H. C. Bheemul, G. Lu, and Y. Yan, "Three-Dimensional Visualization and Quantitative Characterization of Gaseous Flames," *Measurement Science and Technology*, vol. 13, no. 10, p. 1643, 2002. [Online]. Available: http://stacks.iop.org/0957-0233/13/i=10/a=318

[31] K. Lynch, "Development of a 3-D Fluid Velocimetry Technique Based on Light Field Imaging," Master's thesis, Auburn University, May 2011.

[32] B. S. Thurow and K. P. Lynch, "Development of a High-Speed Three-Dimensional Flow Visualization Technique," *AIAA Journal*, vol. 47, no. 12, pp. 2857–2865, 2013/04/25 2009. [Online]. Available: http://arc.aiaa.org/doi/abs/10.2514/1.41788

[33] J. Belden, T. T. Truscott, M. C. Axiak, and A. H. Techet, "Three-Dimensional Synthetic Aperture Particle Image Velocimetry," *Measurement Science and Technology*, vol. 21, no. 12, p. 125403, 2010. [Online]. Available: http://stacks.iop.org/0957-0233/21/i=12/a=125403

[34] F. Ives, US Patent 725,567, 1903.

[35] V. Vaish, G. Garg, E.-V. Talvala, E. Antunez, B. Wilburn, M. Horowitz, and M. Levoy, "Synthetic Aperture Focusing using a Shear-Warp Factorization of the Viewing Transform," in *Proceedings of the 2005 IEEE Computer Society Conference on Computer Vision and Pattern Recognition (CVPR'05) - Workshops - Volume 03*, ser. CVPR '05. Washington, DC, USA: IEEE Computer Society, 2005, pp. 129–. [Online]. Available: http://dx.doi.org/10.1109/CVPR.2005.537

[36] M. Levoy, R. Ng, A. Adams, M. Footer, and M. Horowitz, "Light Field Microscopy," *ACM Trans. Graph.*, vol. 25, no. 3, pp. 924–934, Jul. 2006. [Online]. Available: http://doi.acm.org/10.1145/1141911.1141976

[37] M. Temerinac-Ott, O. Ronneberger, R. Nitschke, W. Driever, and H. Burkhardt, "Spatially-Variant Lucy-Richardson Deconvolution for Multiview Fusion of Microscopical 3D Images," in *Biomedical Imaging: From Nano to Macro, 2011 IEEE International Symposium on*, 2011, pp. 899 –904.

[38] P. Anglin, S. J. Reeves, and B. S. Thurow, "Characterization of Plenoptic Imaging Systems and Efficient Volumetric Estimation from Plenoptic Data," Auburn University, Tech. Rep., 2015. [Online]. Available: http://hdl.handle.net/11200/48467

[39] R. Bracewell, "Strip Integration in Radio Astronomy," *Aust. J. Phys.*, vol. 9, no. 2, pp. 198–217, Jan. 1956. [Online]. Available: http://www.publish.csiro.au/paper/PH560198

[40] J. I. Jackson, C. H. Meyer, and D. G. Nishimura, "Selection of a Convolution Function for Fourier Inversion Using Gridding," *IEEE Transactions on Medical Imaging*, vol. 10, No. 3, pp. 473–478, 1991.

[41] S. R. Deans, *The Radon Transform and Some of Its Applications.* Krieger Publishing Company, 1983. [Online]. Available: http://findarticles.com/p/articles/mi_m0QLT/is_/ai_n24382324

[42] Y. S. Amir Averbuch, "3D Fourier Based Discrete Radon Transform," *Applied and Computational Harmonic Analysis*, vol. 15, pp. 33–69, 2003.

[43] G.-H. Chen, S. Leng, and C. A. Mistretta, "A Novel Extension of the Parallel-Beam Projection-Slice Theorem to Divergent Fan-Beam and Cone-Beam Projections," *Medical Physics*, vol. 32, no. 3, pp. 654+, 2005. [Online]. Available: http://dx.doi.org/10.1118/1.1861792

[44] Z.-P. Liang and J. Munson, D.C., "Partial Radon Transforms," *Image Processing, IEEE Transactions on*, vol. 6, no. 10, pp. 1467–1469, 1997.

[45] B. S. Thurow and T. Fahringer, "Recent Development of Volumetric PIV with a Plenoptic Camera," in *Proceeding of the* 10^{th} *International Symposium on Particle Image Velocimetry, Delft, The Netherlands, July 1-3*, 2013.

[46] T. Fahringer and B. Thurow, "The Effect of Grid Resolution on the Accuracy of Tomographic Reconstruction Using a Plenoptic Camera," in *51st AIAA Aerospace Sciences Meeting including the New Horizons Forum and Aerospace Exposition*. American Institute of Aeronautics and Astronautics, 2014/01/02 2013. [Online]. Available: http://dx.doi.org/10.2514/6.2013-39

[47] ——, "Tomographic Reconstruction of a 3-D Flow Field Using a Plenoptic Camera," in *American Institute of Aeronautics and Astronautics*. American Institute of Aeronautics and Astronautics, 2014/01/02 2012.